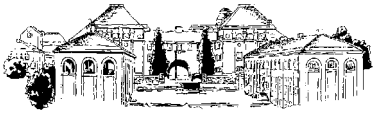

KUNGL TEKNISKA HÖGSKOLAN

ISSN 1403-1701 Kärnkraftsäkerhet 10
TRITA EKS.Avhandling
ISRN KTH/NPS/APRI/Ignalina-0402-SE

ANALYSIS METHODOLOGY FOR RBMK-1500 CORE SAFETY AND INVESTIGATIONS ON CORIUM COOLABILITY DURING A LWR SEVERE ACCIDENT

Doctoral Thesis

by

Audrius Jasiulevicius

Stockholm
2003

Department of Energy Technology
Division of Nuclear Power Safety
The Royal Institute of Technology
Stockholm, Sweden

Institutionen för Energiteknik
Avd. för Kärnkraftsäkerhet
Kungliga Tekniska Högskolan
Stockholm

Abstract

This thesis presents the work involving two broad aspects within the field of nuclear reactor analysis and safety. These are:

- development of a fully independent reactor dynamics and safety analysis methodology of the RBMK-1500 core transient accidents and
- experiments on the enhancement of coolability of a particulate bed or a melt pool due to heat removal through the control rod guide tubes.

The first part of the thesis focuses on the development of the RBMK-1500 analysis methodology based on the CORETRAN code package. The second part investigates the issue of coolability during severe accidents in LWR type reactors: the coolability of debris bed and melt pool for in-vessel and ex-vessel conditions.

The safety of the RBMK type reactors became an important area of research after the Chernobyl accident. Since 1989, efforts to adopt Western codes for the RBMK analysis and safety assessment are being made. The first chapters of this Thesis describe the development of an independent neutron dynamics and safety analysis methodology for the RBMK-1500 core transients and accidents. This methodology is based on the codes HELIOS and CORETRAN. The RBMK-1500 neutron cross section library was generated with the HELIOS code. The ARROTTA part of the CORETRAN code performs three dimensional neutron dynamics analysis and the VIPRE-02 part of the CORETRAN package performs the rod bundle thermal hydraulics analysis. The VIPRE-02 code was supplemented with additional CHF correlations, used in RBMK-type reactor calculations. The validation, verification and assessment of the CORETRAN code model for RBMK-1500 were performed and are described in the thesis.

The second part of the thesis describes the in-vessel particulate debris bed and melt pool coolability investigations. The role of the control rod guide tubes (CRGTs) in enhancing the coolability during a postulated severe accident in a BWR was investigated experimentally. This investigation is directed towards the accident management scheme of retaining the core melt within the BWR lower head.

The particulate debris bed coolability was also investigated during the ex-vessel severe accident situation, having a flow of non-condensable gases through the porous debris bed. Experimental investigations on the dependence of the quenching time on the non-condensable gas flow rate were carried out.

The first chapter briefly presents the status of developments in both the RBMK-1500 core analysis and the corium coolability areas.

The second chapter describes the generation of the RBMK-1500 neutron cross section data library with the HELIOS code. The cross section library was developed for the whole range of the reactor conditions (i.e. for both cold and hot reactor states). The results of the benchmarking with the WIMS-D4 code and validation against the

RBMK Critical Facility experiments is also presented here. The HELIOS generated neutron cross section data library provides a close agreement with the WIMS-D4 code results. The validation against the data from the Critical Experiments shows that the HELIOS generated neutron cross section library provides excellent predictions for the criticality, axial and radial power distribution, control rod reactivity worths and coolant reactivity effects, etc. The reactivity effects of voiding for the system, fuel assembly and additional absorber channel are underpredicted in the calculations using the HELIOS code generated neutron cross sections. The underprediction, however, is much less than that obtained when the WIMS-D4 code generated cross sections are employed.

The third chapter describes the work, performed towards the accurate prediction, assessment and validation of the CHF and post-CHF heat transfer for the RBMK-1500 reactor fuel assemblies employing the VIPRE-02 code. This chapter describes the experiments, which were used for validating the CHF correlations, appropriate for the RBMK-1500 type reactors. These correlations after validation were added to the standard version of the VIPRE-02 code. The VIPRE-02 calculations were benchmarked against the RELAP5/MOD3.3 code. It was found that these user-coded additional CHF correlations developed for the RBMK type reactors (Osmachkin, RRC KI and Khabenski correlations) and implemented into the code by the author, provide a good prediction of the CHF occurrence at the RBMK reactor nominal pressure range (at about 7 MPa). Transition and film boiling are also predicted well with the VIPRE-02 code for this pressure range. It was found, that for the RBMK-1500 reactor applications, EPRI CHF correlation should be used for the CHF predictions for the lower fuel assemblies of the reactor in the subchannel model of the RBMK-1500 fuel assembly. RRC KI and Bowring CHF correlations may be used for the upper fuel assemblies. For a single-channel model of the RBMK-1500 fuel channel, Osmachkin, RRC KI and Bowring correlations provide the closest predictions and may be used for the CHF estimation. For the low coolant mass fluxes in the fuel channel, Khabenski correlation can be applied.

The fourth chapter presents the verification of the CORETRAN code for the RBMK-1500 core analysis (HELIOS generated neutron cross section data, coupled CORETRAN 3-D neutron kinetics calculations and VIPRE-02 thermal hydraulic module). The model was verified against a number of RBMK-1500 plant data and transient calculations. The new RBMK-1500 core model was successfully applied in several safety assessment applications. A series of transient calculations, considered within the scope of the RBMK-type reactor Safety Analysis Report (SAR), were performed. Several cases of the transient calculations are presented in this chapter. The HELIOS/CORETRAN/VIPRE-02 core model for the RBMK-1500 is fully functional. The RBMK-1500 CPS logic, added into the CORETRAN provides an adequate response to the changes in the reactor parameters.

Chapters 5 and 6 describe the experiments and the analysis performed on the coolability of particulate debris bed and melt pool during a postulated severe accident in the LWR. In the Chapter 5, the coolability potential, offered by the presence of a large number of the Control Rod Guide Tubes (CRGTs) in the BWR lower head is presented. The experimental investigations for the enhancement of coolability

possible with CRGTs were performed on two experimental facilities: POMECO (POrous MEdium COolability) and COMECO (COrium MElt COolability). The influence of the coolant supply through the CRGT on the debris bed dryout heat flux, debris bed and melt pool quenching time, crust growth rate, etc. were examined. The heat removal capacity offered by the presence of the CRGT was quantified with the experimental data, obtained from the POMECO and COMECO facilities. It was found that the presence of the CRGTs in the lower head of a BWR offers a substantial potential for heat removal during a postulated severe accident. Additional 10-20 kW of heat were removed from the POMECO and COMECO test sections through the CRGT. This corresponds to the average heat flux on the CRGT wall equal to 100-300 kW/m^2.

In the Chapter 6 the ex-vessel particulate debris bed coolability is investigated, considering the non-condensable gases released from the concrete ablation process. The influence of the flow of the non-condensable gases on the process of quenching a hot porous debris bed was considered. The POMECO test facility was modified, adding the air supply at the bottom of the test section, to simulate the non-condensable gas release. The process was investigated for both high and low porosity debris beds. It was found that for the low porosity bed composition the counter-current flooding limit could be exceeded, which would degrade the quenching process for such bed compositions. The experimental results were analyzed with several CCFL models, available in the literature.

Keywords: RBMK, light water reactor, core analysis, transient analysis, reactor dynamics, RIA, ATWS, critical heat flux, post-CHF, severe accidents, particulate debris beds, melt pool coolability, BWR, CRGT, dryout, quenching, CCFL, crust growth, solidification, water ingression, heat transfer.

Preface

This thesis is based on the results of research activities, carried out by the author during the period from 2000 to 2003 at the Nuclear Power Safety Division, Royal Institute of Technology (KTH). The results of these activities have been summarized and described in the following publications:

1. Jasiulevicius, A., Sehgal, B.R., "**Development and Validation of HELIOS neutron cross section library for RBMK reactors**", Proceedings of 10th meeting on Reactor Physics Calculations in the Nordic Countries, Roskilde, May 14-15, 2001.
2. Jasiulevicius, A., Kubarev, A., Sehgal, B. R., "**Development and Validation of a Methodology for Neutron Dynamics Analysis of RBMK Reactors**", Proceedings of ANS International Meeting on Mathematical Methods for Nuclear Applications, *Salt Lake City, USA*, September 9-12, 2001.
3. Jasiulevicius, A., Sehgal, B.R., "**VIPRE02 code assessment for CHF and post-CHF heat transfer modes in long tubes**", Proceedings of ANS 2002 student conference, *Pennsylvania State University, PA, USA*, April 10-12, 2002.
4. Jasiulevicius, A., Sehgal, B.R., "**Validation of HELIOS neutron cross-section library for RBMK reactors against the data from the Critical Facility experiments**", Proceedings of ICONE-10 conference, *Arlington, Virginia, USA*, April 14-18, 2002.
5. Jasiulevicius, A., Sehgal, B.R., "**VIPRE02 code assessment for CHF and post-CHF heat transfer modes in long tubes**", Proceedings of ICONE-10 conference, *Arlington, Virginia, USA*, April 14-18, 2002.
6. Konovalikhin, M.J., Jasiulevicius, A., Sehgal, B.R., "**Heat removal through control rod guide tube in BWR lower head during a severe accident**", Proceedings of the 40th European two-phase flow meeting, *Stockholm, Sweden*, June10-13, 2002.
7. Jasiulevicius, A., Kubarev, A., Sehgal, B.R., "**CORETRAN code application for RBMK reactor safety analysis**", Proceedings of PHYSOR 2002 conference, *Seoul, Korea*, October 7-10, 2002.
8. Sehgal, B.R. and Jasiulevicius, A. "**POMECO and COMECO experiments on investigation of the potential for coolability by BWR control rod guide tubes"**, APRI-4 program report for SKi. December 2002.
9. E. Bubelis (LEI), M. Clemente (GRS), A. Jasiulevicius (KTH), A. Kaliatka (LEI), A. Kubarev (KTH), R. Pabarcius (LEI), J.P. Weber (GRS) **Review of the Revised RRC KI Report "Calculation Substantiation of Tender Specification for Second Shut Down System of the INPP Unit-2 without Dividing of the CPS Loop and without Using CRO"**, SIP Report Nº 95593-R29, February 2003.

10. Sehgal, B. R., Park, H., S., Giri, A., Karbojian, A., Jasiulevicius, A., Ma, W.M., Hansson, R. C., "**Melt-Structure-Water Interactions During Postulated Severe Accidents in LWR's**" Annual report on MSWI project for Swiss Federal Office of Energy, February, 2003.

11. Konovalikhin, M.J., Jasiulevicius, A., Sehgal, B.R., "**Debris bed coolability in the BWR pressure vessel**", Proceedings of 6th ASME-JSME Thermal Engineering Joint Conference, *Kohala Coast, Havaii, USA*, March 16-20, 2003.

12. Jasiulevicius, A**., "Reactor physics calculations and core analysis at the Nuclear Power Safety Division, KTH"**, VTT Symposium 230, ISBN 951-38-6286-0, ISSN 1455-0873.

13. Jasiulevicius, A., Sehgal, B.R., Asmolov, V., Kobzar, L., "**VIPRE02 code development and validation for CHF prediction in RBMK reactor fuel assemblies** ", Proceedings of ICONE-11 conference, *Tokyo, Japan*, April 20-23, 2003.

14. Jasiulevicius, A., Sehgal, B.R., "**Debris bed quenching with non-condensable gas addition from bottom",** Proceedings of ICONE-11 conference, *Tokyo, Japan*, April 20-23, 2003.

15. Sehgal, B.R., Konovalikhin, M.J., Jasiulevicius, A., "**Debris bed coolability in the BWR pressure vessel**", Proceedings of HEFAT2003, 2nd Conference on Heat Transfer, Fluid Mechanics and Thermodynamics, *Victoria Falls, Zambia*, June 23-26, 2003.

16. Jasiulevicius, A., Sehgal, B.R., "**Modelling of critical heat flux in long tubes and tube bundles with VPRE02 and RELAP5 codes"**, Proceedings of 4th Baltic Heat Transfer Conference, *Kaunas, Lithuania*, 25-27 August, 2003.

17. Jasiulevicius, A., Kubarev, A., Sehgal, B.R., "**RBMK-1500 transient analysis with CORETRAN code**". Proceedings of NURETH-10 conference, *Seoul, Korea*, October 5-9, 2003.

18. Jasiulevicius, A., Sehgal, B.R., "**COMECO experiments on molten pool coolability in BWR lower head**". Proceedings of NURETH-10 conference, *Seoul, Korea*, October 5-9, 2003.

19. Gylys, J., Adomavicius, A., Belousov, A., Ognerubov, V., Jasiulevicius, A., "**The analysis of single control rod withdrawal accident case at Ignalina NPP for RBMK-1500 reactor referent full power state, employing coupled neutronics-thermohydraulics code CORETRAN**", Proceedings of III International Conference on Industrial Heat Engineering, *Kiev, Ukraine*, September 29 – October 4, 2003.

20. Jasiulevicius, A., Sehgal, B. R**., "Investigations on the enhancement of corium coolability with CRGTs in the lower head of a BWR"**, Accepted to be published in *Nuclear Engineering and Design*.

Contents

TABLE OF FIGURES

Table of tables

Nomenclature

Arabic

a	Temperature coefficient of conductivity, m^2s
c	Specific heat, J/kg·K
d	Diameter, m
g	Gravity acceleration, m/s^2
h	Enthalpy, J/kg; heat transfer coefficient, W/m^2K
j	Current, n/cm^2
k	Multiplication factor; peaking factor; thermal conductivity coefficient, W/m·K
u	Lethargy
p	Pressure, Pa
q	Heat flux, W/m^2
r	Latent heat of vaporization, J/kg
t	Time, s
x	Mass quality
z	Height, m
A	Area, m^2
G	Flow rate, kg/s
H	Height, m
N	Number density, n/cm^3
Pr	Prandl number
R	Radius, m
Re	Reynolds number
S	Surface area, m^2
T	Temperature, K
V	Volume, m^3
W	Power, W
We	Weber number

Greek

α	Reactivity coefficient
δ	Effective addition, m
ε	Porosity
χ	Fission spectrum; quality
ϕ	Neutron flux
λ	Intermediate resonance factor
ρ	Reactivity, β; density, kg/m^3
ρw	Mass flux, kg/m^2s
σ	Microscopic neutron cross section, barn; surface tension coefficient, N/m
$\kappa\Sigma_f$	Fission-energy production
μ	Dynamic viscosity coefficient, Pa·s
ν	Kinematic viscosity coefficient, m^2s

$\nu\Sigma_f$	Fission-neutron production
Φ	Linear heat rate, W/m
Σ	Macroscopic cross section, barn

Subscripts/Superscripts

0g	P0 scattering
1g	P1 scattering
ag	Absorption
b	Background
c	Crust
cr	Critical
e	Equilibrium
el	Electrical
f	Fuel
fg	Fission, heat of vaporization
fus	Fusion
g	Total, Graphite
i	Component i
inf	Infinite
l	Liquid
m	Melt
j	Component j
r	Radial
r1	Removal from 1st group
p	Particle
rad	Radiation
rg	Removal
p	Potential
out	Outside
sat	Saturation
sol	Solid
sub	Subcooled
th	Thermal
v	Volumetric; vapour
w	Water
x	Type of the macroscopic neutron cross section x
z	Axial
Ber	Berenson
F	Fuel
C	Coolant
M	Moderator
SB	Stefan-Boltzman

Abbreviations

AZ	Russian acronym for Emergency Protection
ALS	Accident Localization System

ATWS	Anticipated Transient Without Scram
BDBA	Beyond Design Basis Accident
BWR	Boiling Water Reactor
CCCP	Current Coupling Collision Probability
CCFL	Counter Current Flooding Limitation
CE	Combustion Engineering
CHF	Critical Heat Flux
CPR	Critical Power Ratio
CPS	Control and Protection System
CRGT	Control Rod Guide Tube
DAS	Data Acquisition System
DBA	Design Basis Accident
DNB	Departure from Nucleate Boiling
DNBR	Departure from Nucleate Boiling Ratio
ECCS	Emergency Core Cooling System
ECF	Experimental Critical Facility
EdF	Electricité de France
EPRI	Electric Power Research Institute
EREC	Electrogorsk Research and Engineering Centre
FASR	Fast Acting Scram Rod
FASS	Fast Acting Scram System
FC	Fuel Channel
HEM	Homogeneous Equilibrium Model
IAEA	International Atomic Energy Agency
INEL	Idaho National Engineering Laboratory
IPPE	Institute of Physics and Power Engineering
LAC	Local Automatic Control
LEI	Lithuanian Energy Institute
LEP	Local Emergency Protection
LOCA	Loss Of Coolant Accident
LPLF	Low Pressure Low Flow
LWR	Light Water Reactor
MCC	Main Circulation Circuit
CCI	Molten Corium – Concrete Interaction
MCR	Manual Control Rod
MOC	Method Of Characteristics
NPP	Nuclear Power Plant
NUPEC	Nuclear Power Engineering Corporation
PDDMS	Power Density Distribution Monitoring System
PHWR	Pressurized Heavy Water Reactor
PTR	Pressure Tube Reactor
PWR	Pressurized Water Reactor
RIA	Reactivity Initiated Accident
RCS	Reactor Cooling Circuit
RBMK	Russian acronym for High Power Boiling Reactor
RIT	Royal Institute of Technology
RPV	Reactor Pressure Vessel
RRC KI	Russian Research Centre Kurchatov Institute

SAR	Safety Analysis Report
SCR	Shortened Control Rod
UCLA	University of California in Loa Angeles
VVER	Russian acronym for Water-Water Energy Reactor

Acknowledgements

There are so many people I should thank for making my work at KTH possible. Their help guided me through my years of stay and studies in Sweden and they made my work a memorable and most rewarding experience. First of all I wish to express my gratitude to my supervisor, Prof. Bal Raj Sehgal, for giving me the opportunity to join and work in his World Class laboratory. I wouldn't thank Bal Raj enough for his trust, support and advice. The chance to work and learn from the best has made my research and progress possible.

I could not possibly name everyone who has contributed significantly to my understanding of the subject, but I will at least try to mention people who were closest to me during the last three years. Of course, this was our ever-changing group at KTH. Among the colleagues who have assisted me in one way or another, I feel very much indebted to Andrei Kubarev, my office-mate and advisor, who was sharing his knowledge with me and leading me through the exciting and sometimes confusing world of RBMK's. As well, among the other people I met over the years my special thanks go to Mr. Antanas Romas (now at ES-Konsult AB) and Dr. Maxim Konovalikhin (now at FzK Karlsruhe), my mentors and advisors in the times I needed support.

I cannot fail to mention Ms. Kajsa Bergman – the wonderful lady who happens to be our administrator. There are countless little favors she did to me, as to everybody else at our Division, to make our life in Sweden easy and comfortable. Not to mention the big favors – such as giving me a place to stay during my first month in Stockholm, when I was lost in the traps of complicated housing situation of a big city.

Special thanks have to go to our staff in the lab: Aram, José, Conny and Gunnar who made all our experimental plans and designs become real. And of course the rest of the guys (and a girl) who were working side by side with me over this time: Armen, Anand, Askar, Asis, Dereje, Lin, Ma, Sean, Sun, Utkarsh and Tita. And of course people who I never met, but who did the research at the Division during the years before I joined the group, and on whose shoulders I could stand and continue their research: Dr. T. N. Dinh and Dr. R. Nourgaliev (both now at the University of California in Santa Barbara, USA).

There is also a number of people outside our division whose indispensable advice helped in my research over these years. I would like to thank Dr. Rudi Stamm'ler, the chief physicist from Studsvik Scandpower for the uncountable number of e-mails and phone calls we exchanged. I feel extremely lucky to get to know a person like Rudi, whose admirable knowledge and wonderful personality I will remember for many years to come. As well specials thanks are devoted to the researchers at PSI: Dr. Yacine Aounallah and Hakim Ferroukhi and their leader Dr. Martin Zimmermann for all the help they had generously provided us during our early days of struggle with CORETRAN and VIPRE-02 codes. Last but certainly not the least I would like to

mention Mr. Per Bystedt from SiP, who was not just a manager of our research projects during the last many years but also became a friend, supporter and advisor.

At the end of the long list of people who help and supported me over the years, I would like to thank the ones, without whom all this would never happened. I am thankful to my family beyond all words. I thank my parents back in Lithuania. And most of all I wish to thank my wife Ausra, daughter Aura and son Aidas, who was born during our stay in Stockholm. For trusting in me and following me to another country, while sometimes compromising their own interest and for all love and support. I would never have done this without you!

Sponsors and industry

The thesis work was financed by the following organizations and projects:

1. The Swedish International Projects (SiP).
2. The SKI and Swedish and Finnish power companies in the frame of APRI project.

I am grateful to all the sponsors and I would like to thank all their representatives – in particular Per Bystedt, Per Ringström, Viviana Sandberg, Ninos Garis, Oddbjörn Sandervåg, Wiktor Frid, Veine Gustavsson and other for their help and feedback.

Summary of Technical Accomplishments and Contributions

	Technical Accomplishments and Contributions	*Chapters Appendices*
I. Generation of RBMK-1500 cross section data and result validation		
1	A neutron cross section library for the RBMK-1500 core neutronic analysis with CORETRAN code was generated with the HELIOS code for fuel and non-fuel assemblies of the RBMK-1500 reactor.	Chapter 2 App. A
2	The neutron cross section data library for the RBMK-1500, generated using the HELIOS code, was benchmarked against that obtained with the WIMS-D4 code. The HELIOS library was generated based on a different methodology (independent fuel and graphite temperature variations in all reactor regions). It was found that the values of the cross sections were close to each other in the two libraries.	Chapter 2 App. A App. B
3	The new HELIOS cross section library was implemented into the CORETRAN code. The result of the work was a new fully independent RBMK-1500 reactor core analysis tool, based on the Western methodologies and codes.	Chapter 4 App. A
4	The validation of the HELIOS code calculated cross section data was performed against the data from the KI Critical Facility experiments, using the 3-D neutron kinetics code CORETRAN. Good agreement with the experimental data was obtained.	Chapter 2 App. A App. B
II. VIPRE-02 code assessment and validation against CHF data for long tubes and tube bundles		
5	RBMK-specific CHF correlations were implemented into the VIPRE-02 code. These were the RRC KI, Osmachkin and Khabenski correlations. This allowed performing the detailed thermal hydraulic analysis of the RBMK-1500 core and prediction of the margins to CHF for this reactor type with VIPRE-02 code.	Chapter 3 App. C
6	CHF and post-CHF correlations implemented in VIPRE-02 were validated against the data from single heated long channel experiments, performed at KTH, Stockholm and at the E-108 test facility in Electrogorsk, Russia. For the pressures of 2-3 MPa, the best agreement with the experimental data for the CHF was obtained with the Bowring CHF correlation. Good agreement with the CHF experimental results was obtained with the Osmachkin and Bowring correlations for p=7 MPa. Maximum wall temperatures during transition and film boiling were also predicted correctly	Chapter 3 App. C

	for the pressures of 7-12 MPa. For pressures of >16 MPa, CHF is predicted well with the EPRI CHF correlation. Transition boiling correlations, used in VIPRE-02, underpredict the maximum wall temperatures for this pressure region. For the film boiling, all VIPRE-02 correlations provide good agreement with the experimental data.	
7	Subchannel model of the RBMK-1500 fuel bundle was validated against the CHF experiments performed at the RRC KI, Russia. These calculations show that for the subchannel model at p=7 MPa the CHF for the upper RBMK-1500 fuel assemblies can be predicted well using RRC KI and Bowring CHF correlations. For the lower RBMK-1500 fuel assemblies, a good agreement with the experimental data is obtained using EPRI correlation. For the low coolant mass flux region, the Khabenski correlation provides accurate CHF predictions for the RBMK-1500 fuel bundles.	Chapter 3 App. D
III. Ignalina NPP RBMK-1500 reactor core analysis		
8	Assessment of the RBMK-1500 core analysis methodology was performed. The work evaluated the performance of the RBMK-1500 CPS logic added to the CORETRAN and the interface between the HELIOS neutron cross section library and CORETRAN code. The analysis performed proved that this new RBMK-1500 core analysis methodology based on the HELIOS and the modified CORETRAN code provides reliable results and can be applied for RBMK-1500 core performance and safety evaluations.	Chapter 4 App. A
9	The methodology developed above was benchmarked against the STEPAN code for steady state operation of the RBMK-1500 reactor. A number of actual reactor states for both Unit 1 and 2 of the Ignalina NPP were calculated. Both HELIOS and WIMS-D4 generated cross section libraries were used. Good predictions for the criticality, radial and axial power distribution, fast power coefficient and voiding effect in the RBMK-1500 reactor were obtained.	Chapter 4 App. A, App. E
10	The CORETRAN simulation of experiments on shut down RBMK-1500 reactor were performed. Good agreement with the experimental data was obtained for the FASS rod worth and reactor subcriticality.	Chapter 4
11	Calculations were performed for all RBMK-1500 core transients, considered within the scope of neutronic calculations of the Ignalina NPP safety analysis report (SAR), including the RIA and ATWS cases. Benchmarking was done against the STEPAN code. CORETRAN calculations were performed with both	Chapter 4 App. A App. E

	HELIOS and WIMS-D4 cross section libraries. The results obtained proved the capabilities of the developed HELIOS/CORETRAN/VIPRE-02 package to perform the RBMK-1500 core analysis.	
12	Coupled neutronic and thermal hydraulic analysis of RBMK-1500 transients were performed. The results obtained from the neutronic calculations (e.g. power behavior during the transient) were supplied to the subchannel model of VIPRE-02 to estimate the safety margins during the transients. The model allowed detailed estimation of critical safety parameters, such as maximum fuel or cladding temperature during a transient. It proved to be fully functional and provided reasonable results.	Chapter 4 App. E
IV. Investigations of additional coolability potential offered by the presence of the CRGTs during the LWR severe accidents		
13	Experiments on the POMECO facility on the particulate debris beds containing a model of a CRGT were performed. The coolant was supplied through the CRGT at different subcooling and flow rates. The experiments show that additional 10-20 kW of heat could be removed through the CRGT test section. This corresponds to the heat flux in the CRGT wall of 100-200 kW/m^2. Lipinski model for the dryout heat flux in a particulate debris bed, with the additional heat removal through the CRGT taken into account, provided good comparison with the measured dryout heat flux. A zero-dimensional model for the quenching time provided good agreement with the measured values of quenching time.	Chapter 5 App. F
14	A high temperature (up to 1100°C) experiment with the particulate debris bed in the COMECO facility was carried out in order to assess the quenching phenomena at higher temperatures (compared to the POMECO facility). It was found that the analysis model developed could predict the measured data obtained for the higher temperatures.	Chapter 5
15	Experiments on high temperature melt pool coolability with the presence of a model of CRGT in the COMECO facility were performed. Various flow rates and liquid subcooling were employed in the CRGT and open/closed upper bypass was used. The experiments on the molten pool supported the findings of the POMECO experiments: additional 10-20 kW of heat could be removed from the test section through the CRGT. This corresponds to an average heat flux in the CRGT model of the COMECO facility equal to about 300 kW/m^2. A zero-dimensional model for the	Chapter 5 App. G

	prediction of the molten pool quenching time was developed. The model provided good comparison to the measured quenching time. The model also allowed estimating the influence on the presence of the CRGT in the test section on the quenching time.	
16	Analysis of the film boiling heat transfer during the COMECO was performed, using the Berenson equation for the film boiling. The model provided a good prediction of the heat removal values during the film boiling phases of the COMECO experiments.	Chapter 5 App. G
17	Analysis of the crust formation and crust growth on the top of the melt pool during the COMECO experiments was carried. Farmer's model for crust formation and crust growth under dry and wet conditions was applied. For both dry and wet cavity cases, the Farmer's model provided a good estimation of the experimental crust growth and water ingression rates. The Farmer's model for the water ingression was supplemented with the additional relationship to take into account the change in the dryout heat flux during the quenching process. This allows obtaining good predictions of the COMECO experimental results. The analysis had shown that the presence of the CRGT in the melt pool significantly increases the crust growth rate and the water ingression depth.	Chapter 5 App. G
V. Investication of the CCI process in porous medium		
18	POMECO experiments on quenching of the particulate debris beds with non-condensable gas injection from the bottom were performed. The onset of the CCFL for the low and high porosity bed compositions was noted. It was found that for low porosity beds (ε=0.26) the CCFL could be exceeded at gas generation rates, similar to the gas release from the limestone-common sand concrete during the CCI. This indicates that quenching of low porosity beds could be difficult.	Chapter 6 App. H
19	The data of the POMECO experiments with the non-condensable gas injection were applied for the CCFL analysis using Wallis and Marshall/Dhir CCFL correlations. It was found, that for the high porosity debris beds (ε=0.4), the Wallis CCFL correlation provides good prediction for the onset of the CCFL. For the low porosity bed composition (ε=0.26), the Marshall-Dhir correlation provides a better prediction for the CCFL.	Chapter 6 App. H

Chapter 1

INTRODUCTION

The Chernobyl accident took place in 1986. Its consequences affected the future of nuclear power all over the world. They also generated an intensive effort on the part of Soviet nuclear community to improve the safety of the RBMK type reactors. Much of the effort went to improve the safety of the core e.g. by reducing the positive void reactivity coefficient, by increasing the speed and worth of the control rods, etc. These efforts were directed primarily towards the prevention of a Chernobyl type reactivity induced accident (RIA).

Concurrently with the work in Soviet Union the West was busy in performing experiments and developing methodology for prediction of the consequences of severe accidents in LWRs of the type experienced in TMI-2 reactor in USA. The work is still continuing and part of this thesis is devoted to the research in LWR severe accidents.

The RBMK-type reactors, designed and built in the former Soviet Union were not known to the Western nuclear community. The Chernobyl tragedy generated series of investigations of this reactor type, applying the Western tools and methodologies, with the aim to understand this reactor type and to prevent future accidents. The adoption and application of the codes of Western design for the RBMK reactor performance and safety assessment is still an on-going process. Since the analysis codes developed in the West are intended for LWRs (PWRs and BWRs), the direct application of the codes is in most cases incorrect and not possible. Therefore, the codes have to be modified and validated as much as possible before they can be used for the RBMK safety analysis.

The LWR severe accidents that are the subject of intensive research since the TMI-2 accident are usually defined as accidents, during which the melt down of the reactor core occurs. The progression of the severe accident in the LWR may be classified into the in-vessel and ex-vessel phases. These phases involve extreme conditions and high temperatures. The investigations of the severe accident consequences require scaled experiments and numerical simulations in order to describe and assess the complex processes, which are involved at various stages of the accident. The knowledge and understanding of these processes is needed to devise methods to prevent accidents and to mitigate their consequences through accident management.

Particulate debris bed and melt pools occur during the in-vessel and ex-vessel phases of the severe accident. The stabilization and termination of a severe accident requires the cooling and quenching of the debris beds and melt pools in the vessel or when melt-concrete interaction is taking place.

1.1. RBMK reactor core analysis

The analysis and safety assessment of the RBMK type reactor core steady state and transient behavior is performed in a way similar to that for the Western-type LWR: the computer model of the reactor core is developed, using a validated and verified core neutronic analysis code. The neutronic data, such as macroscopic cross sections for different fuel types or various other structures, which are present in the reactor core, are calculated using either deterministic codes (which solve the neutron transport equation using the numerical procedures) or Monte-Carlo codes (which use the statistical approach to obtain the same data sets). The generated cross section data are used in the neutron kinetics calculations, employing 3-D neutron kinetics codes, which take into account the space-time effects of the RBMK core. In order to obtain reliable values the 3-D neutron kinetics code has to be supplemented with an appropriate thermal hydraulic model, which could correctly estimate the thermal hydraulics feedbacks in the neutron kinetics equations.

For the RBMK reactor physics calculations, the two group neutron cross section libraries are generated (Burlakov, et al, 1998, 2000) where the various cross sections are represented as a function of fuel and graphite temperatures, fuel burnup, Xenon-135 concentration and coolant density. For the calculations, performed in Russia the cross section data was calculated with the WIMS-D4 code. The more recent calculations are also carried out employing Monte Carlo codes MCNP4A and MCU (Alexeev, 1998, Burlakov, et al, 2000). However, the methodology of the generation of the cross section data for RBMK type reactors is not fully documented. As well, several corrections were made in the WIMS-D4 generated cross section libraries during the years to obtain better predictions of the experimental results for the RBMK's. In addition to this, the two neutron kinetics codes, developed for the RBMK reactor calculations at RRC Kurchatov Institute (STEPAN code) and RDIPE (SADCO code) employ so-called 'recovery procedures' to correct the calculated radial neutron flux distribution to normalize it to that measured by the neutron detectors installed in the core. These procedures are not fully documented, lack transparency and it is not clear why they have to be employed for RBMK core and not for a western LWR. An independent core analysis methodology, which would use no corrections and recovery procedures, would allow more objective core analysis for the RBMK type reactors. The development of such a methodology was the aim of the work, presented in the first part of this Thesis.

In the RBMK type power plants, similar to the LWR plants, the key safety features, which have to be maintained under normal operation and accident conditions, are:

- Reactivity Control. To avoid inadvertent criticality and to shutdown the reactor from any operational or accident state. The effectiveness, speed of action and the shutdown margin have to be such that the specified safe operation limits are not exceeded.
- Core Cooling. The reactor and auxiliary cooling systems should ensure that the fuel is cooled under all circumstances and that the decay heat is

removed. The capability of the emergency core cooling system to provide adequate short and long term cooling required to limit the escape of fission products in the event of loss of coolant accident.

- Containment of radioactive materials. The capabilities of the reactivity removal, accident localization, leak tight compartments and reactor pressure suppression systems to prevent/limit the release of the radioactive materials.

For the safe operation of the RBMK NPP's safety-related core, system parameters and conditions are defined by the designer and regulators. The parameters must not be violated during the anticipated and postulated design basis accidents. The limits are used as evaluation criteria (acceptance criteria) for the groups of initiating events. Different sets of acceptance criteria are used for anticipated transients, postulated design base accidents and for the anticipated transients without scram (BDBA) (IAEA, 2001).

1.2. Corium debris/melt coolability

The Reactor Pressure Vessel (RPV) is one of the main barriers against the release of the radioactive material into the environment during the severe accident in a LWR.

The RPV comes under severe thermal attack when the core melt drops from the original core boundary into the lower head during the later part of the in-vessel accident progression. The lower head, most probably, will contain water at that time in the scenario and the interaction of the melt discharged to the lower head with water would lead to the formation of a particulate debris bed. If the water supply is not restored, the lower head water will evaporate in time and a melt pool will be formed which will circulate in the lower head and thermally load the vessel to fail it.

It is important to determine (a) can the particulate debris bed be cooled, while it is immersed in water, (b) can the particulate debris bed be cooled when it is dry by flooding it with water from the top and (c) can the melt pool be cooled by flooding it with water from above. If the particulate debris bed/melt pool can be cooled the vessel wall temperatures will not reach so high that the vessel lower head either creeps to failure or melts to failure.

If the vessel cannot be saved the next and last barrier to the radioactivity release to the environment is the containment. The discharged melt from the vessel falls on the concrete in the reactor cavity and attacks the concrete basemat. This attack generates much non-condensable gases and containment will fail unless the melt pool can be cooled to temperatures below the concrete ablation temperature. The easiest accident management action is to flood the cavity. It is imperative to determine whether water flooding will cool the melt pool enough to stop concrete attack.

Several studies of quenching of particle debris beds either by flooding from top or bottom have been reported in the literature (Magallon et al, 1999, Lindholm, 2000, Lipinski, 1982, 1984). Cho and Bova (1983) found that during top flooding, the penetration of liquid was faster in the middle of the particulate layer. Ginsberg at al.

(1982), however, concluded from their experiments that the quenching process was characterized by a two step bi-frontal process with a partial quench front propagating downward and another front traveling upward after the downward front had reached the bottom of the bed. They also proposed a model based on counter-current flooding limitation (CCFL). Tung et al (1986) studied experimentally and analytically the quenching by top flooding when a certain amount of gas was injected at the bottom and heat was generated in the particles. Their model also utilizes CCFL.

In-vessel melt coolability by top flooding of a melt pool circulating in the lower head of a PWR has been investigated recently through the EC-FOREVER-5 and –6 experiments conducted recently at KTH (Sehgal et al, 2003). In these experiments a simulant material melt pool circulated in a 1/10 the scale vessel with a pressure level of 25 bars. The melt pool was flooded and its coolability was measured. It was found that only the top 5-7 centimeters could be cooled. The remaining melt did not cool down.

Ex-vessel melt coolability research on the melt pool flooding with water has been carried out over many years. The most extensive experimental work had been performed at the MACE facility (Sehgal, 1992 et al, Farmer et al, 2000), where the corium masses up to two tons were employed. The series of experiments performed have led to a partial coolability; the complete cool down of the melt was not achieved. Earlier, melt coolability research was also performed at the Sandia National Laboratory: SWISS (Blose, 1987) and WETCOR (Blose, 1993) experiments with stainless steel and corium melts respectively were performed. High-pressure corium quenching tests were performed in FARO facility (Magallon et al, 1999). A series of low temperature simulant material experiments have been conducted by Theofanous et. al. (1998). The melt coolability research was also pursued in Germany (Alsmeyer et. al. 1998) in the COMET project where large scale (several hundred kilograms) melt pools were cooled and stabilized by injecting water at the bottom of the pool. It had been found out that this mode of water addition is much more effective than that of the cooling with the water overlayer alone. These results were confirmed by the smaller scale earlier COMECO and DECOBI (Paladino, 2000) experimental series, carried out at the NPS Division of RIT.

The Swedish BWRs designed by the ASEA Co. have a lower drywell and the vessel is very high above the bottom of the lower drywell. The accident management strategy employed by the Swedish BWRs establishes a pool of water in the lower drywell of 7 to 11 meters depth. The water level, however, is much below the vessel lower head and cannot provide the coolability potential needed for the retention of the core melt within the lower head.

A number of tests were carried out throughout the world on the debris bed coolability issues (with and without gas addition). Schrock et al (1986) have studied the flooding of an isothermal particle bed by steam and water. Hu and Theofanous (1984) investigated the deep volumetrically heated debris beds (up to 101.6 cm deep). Series of DCC tests were carried out at Sandia National Laboratory (Reed et al, 1985) to verify the accuracy of existing coolability models. Kernforschungszentrum Karklsruhe (KfK) (Barleon et al, 1984) carried out series of experiments to measure

dryout heat fluxes and quenching in inductively heated small particle beds. Tung et al (1986) have performed coolability tests at UCLA with volumetrically heated particle beds with top flooding and simultaneous air injection from the bottom, to simulate the gas release from concrete erosion. The experimental test section consisted of a stainless steel particles and Freon-113 was used as a coolant. More recently, SILFIDE tests were carried out at EdF (Decossin, 1999) and POMECO tests at KTH in Stockholm (Konovalikhin and Sehgal, 1999).

1.3. Present work

The present work consists of two parts: first part is devoted to the RBMK-1500 type reactor core analysis. The aim of the work was to develop a fully independent RBMK-1500 core performance and safety analysis methodology. In order to do that, an independent RBMK-1500 macroscopic neutron cross section library was generated using the HELIOS code. The HELIOS calculations were benchmarked with the WIMS-D4 code. No corrections were used in the developed HELIOS cross section library. The library was validated with comparisons of the 3-D neutron kinetics calculations of the RRC KI RBMK Critical Facility experiments, against the measurements. The developed and validated HELIOS neutron cross section library was implemented into the CORETRAN code for the 3-D core neutron kinetics analysis. The CORETRAN code also includes VIPRE-02 module for the fuel assembly thermal hydraulic calculations. The VIPRE-02 code CHF and post-CHF heat transfer models were assessed against experimental data for long (approx. 7 m) tubes and fuel bundles. Additional CHF correlations for the upper and the lower fuel assemblies of the RBMK-1500 type reactor and for low mass flux region of RBMK and VVER type reactor were implemented into VIPRE-02. The CORETRAN model of the RBMK-1500 core was validated against the available RBMK-1500 reactor experimental data and benchmarked against the STEPAN code. The CORETRAN model proved to be fully functional and a number of transient calculations (included in the scope of standard Safety Analysis Report) were performed. Coupled neutronic-thermal hydraulics analysis of the core parameters was carried out for selected cases.

The second part of the thesis deals with the severe accident issue of melt/debris coolability for a LWR. An experimental program on the enhancement of the coolability potential of the particulate corium debris beds and the corium melt pools provided by the presence of control rod guide tubes (CRGTs) was carried out. Two experimental facilities were employed: POMECO facility for the particulate debris bed coolability investigations and the COMECO facility for the corium melt pool coolability investigations. A number of tests with various test section configurations was carried out. For the particulate debris beds, the enhancement of the dryout heat flux and the dry bed quenching rate due to the presence of a CRGT were measured. For the melt pool, the enhancement of the melt pool quenching time, crust growth and water ingression rates due to the presence of this additional heat removal structure (CRGT) were measured.

For the ex-vessel coolability scenario, an investigation on the POMECO test facility of the debris bed coolability with non-condensable gas addition, due to the molten corium-concrete interactions (CCI) was performed. The test section of the

POMECO facility was supplemented with the air supply system to simulate the generation of the non-condensable gases in various types of concrete. The debris beds of different porosities and mean particle sizes were investigated. The effect of the porosity on the quenching time and on the establishment of CCFL was examined.

Chapter 2

Neutron Transport Calculations and Cross Section Library Generation for the RBMK-1500 Reactor.

2.1. Objectives

The objective of the work, presented in this Chapter is to develop and validate a new set of RBMK-1500 neutron cross section data, using the HELIOS code. The library is intended to be used in an independent RBMK-1500 performance and safety analysis methodology, employing 3-D neutron kinetics calculations (described in the Chapter 4). The need for an independent neutron cross section data library for the RBMK-1500 arises from the fact that the recent RBMK-type reactor neutron kinetics codes use WIMS-D4 code generated cross section data, developed almost two decades ago. The generation of the cross section library with WIMS-D4 code was not fully documented. As well, several corrections were introduced into the WIMS-D4 library over the years, e.g. to take into account the presence of various Erbium isotopes in the RBMK-1500 fuel (the Er isotopes were not included into the microscopic cross section database used with WIMS-D4), or to provide correct predictions of the experimental results (voiding effects, etc). The new set of the cross sections was benchmarked against the available WIMS-D4 code calculation results, and validated against the RBMK Experimental Critical Facility tests.

2.2. Introduction and background

For the RBMK reactor physics calculations two group neutron cross section libraries are generated (Burlakov, et al, 1998, 2000) where the neutron cross sections are represented as functions of fuel burnup, fuel and graphite temperatures, Xenon-135 concentration and coolant density. A homogenized cell model is used, having reflecting boundary conditions for multi-group one- or two-dimensional neutron transport equation solution. The spectrum obtained is then employed to collapse the multi-group cross-sections to two-group cross sections.

The developed HELIOS library uses the same approach: 2-D lattice models of various RBMK-1500 geometry compositions (such as fuel channels, control rods, detector channels, etc.) were created and the fast and thermal group library was generated, where the relevant cross sections are included as functions of fuel burnup, coolant density, moderator and fuel temperatures. No corrections were made into the HELIOS generated cross section data in order to obtain a better agreement with the experimental results.

The RBMK Critical Facility at RRC Kurchatov Institute imitates the typical construction of a RBMK type reactor (Davydova, et. al, 1995, Burlakov et al, 2000, etc.). The facility is a graphite stack with the size of 450×450×410 cm. The stack is penetrated with 324 (18×18) vertical holes, located in square graphite lattices with 25 cm pitch. The Critical Facility elements, such as fuel channels, fuel assemblies, control rods, additional absorbers, etc., are identical to the similar RBMK reactor components. These components can be arranged in various configurations, to represent the RBMK-like core structure. A series of measurements (reactivity, voiding, filling with coolant effects, control rod worth measurements, etc.) were carried out during the Critical Facility experimental program.

2.3. HELIOS code

2.3.1. General

The HELIOS code has been developed by Studsvik Scandpower Company. It is widely used for the neutron cross-section data generation for LWR reactors around the world. The code is also used for fuel assembly design, multi-assembly calculations, analysis of lattice irregularities, gamma physics (instrument response, gamma smearing), fuel storage criticality, isotopic accounting, waste disposal calculations, analysis of experiments, etc. (Studsvik Scandpower, 1998). Calculations by the HELIOS code are performed in two-dimensional geometry. Any two-dimensional system can be calculated with HELIOS, allowing for geometric irregularities.

Neutron transport equation is solved employing current coupling and collision probability (CCCP) method. At each calculation point ('reactivity point'), the essential results are particle fluxes and currents, and in case of a burnup or a time step, the new material number densities. Nuclear-data library is ENDF/B-VI based Master library with 190 neutron and 48 gamma groups (Table 1). In order to accelerate the calculation process also the working library with 45 neutron and 18 gamma groups can also be used. There are 286 isotopes, elements and mixtures included in the HELIOS database, including all materials needed for RBMK-1500 macroscopic cell calculations, 28 heavy isotopes and 121 fission products. The code also contains resonance tables for 39 resonance isotopes (11 heavy isotopes, 5 fission products and 23 burnable absorber and control isotopes). Isotopic compositions are automatically saved if they are to be used for branchoff calculations. Compositions (e.g. boron contents, water density, temperatures and material densities), temperatures and power level can be changed during burnup as well as in branchoffs.

Table 1. Neutron energy group structure used in HELIOS calculations.

Lower limits of the 190/112/45-group libraries.

Group	Lower limit (eV)	Group	Lower limit (eV)	Group	Lower limit (eV)
000	2.0000E+07				
001	1.7000E+07	071	3.3546E+03	141	1.2351E+00 27
002	1.4919E+07	072	2.9604E+03	142	1.1664E+00
003	1.3380E+07	073	2.6126E+03	143	1.1254E+00 28
004	1.2000E+07	074	2.3056E+03	144	1.0987E+00
005	1.0000E+07	075	2.0347E+03 10	145	1.0722E+00 29

006	8.8250E+06	076	1.7956E+03	146	1.0623E+00
007	7.7880E+06	077	1.5846E+03	147	1.0525E+00
008	7.4082E+06	078	1.3984E+03	148	1.0427E+00
009	6.0653E+06 1	079	1.2341E+03	149	1.0137E+00 30
010	5.2205E+06	080	1.0891E+03	150	9.9200E-01
011	4.7237E+06	081	9.6112E+02	151	9.7100E-01 31
012	4.4933E+06	082	8.4818E+02	152	9.5065E-01
013	4.0657E+06	083	7.4852E+02	153	9.1000E-01 32
014	3.6788E+06 2	084	6.6057E+02	154	8.7642E-01
015	3.1664E+06	085	5.8295E+02	155	8.3368E-01
016	2.8650E+06	086	5.1445E+02	156	7.8208E-01 33
017	2.7253E+06	087	4.5400E+02	157	7.3000E-01
018	2.4660E+06	088	4.0065E+02	158	6.7000E-01
019	2.3650E+06	089	3.5358E+02	159	6.2506E-01 34
020	2.3457E+06	090	3.1203E+02	160	5.7000E-01
021	2.2313E+06 3	091	2.7536E+02	161	5.3000E-01
022	2.0189E+06	092	2.4301E+02	162	5.0323E-01
023	1.8268E+06	093	2.1445E+02	163	4.5000E-01
024	1.7377E+06	094	1.8926E+02	164	4.1704E-01
025	1.5724E+06	095	1.6702E+02	165	3.5767E-01 35
026	1.3534E+06 4	096	1.4739E+02	166	3.2063E-01
027	1.1649E+06	097	1.3007E+02 11	167	3.0112E-01
028	1.0540E+06	098	1.1479E+02	168	2.9074E-01
029	1.0026E+06	099	1.0130E+02	169	2.7052E-01 36
030	8.2085E+05 5	100	8.9398E+01	170	2.5103E-01
031	7.0651E+05	101	7.8893E+01 12	171	2.2769E-01
032	6.3928E+05	102	6.9623E+01	172	1.8443E-01 37
033	6.0810E+05	103	6.1442E+01	173	1.5230E-01
034	4.9787E+05 6	104	5.4222E+01	174	1.4572E-01 38
035	4.2852E+05	105	4.7851E+01 13	175	1.1157E-01 39
036	3.8774E+05	106	4.2229E+01	176	8.1968E-02 40
037	3.6883E+05	107	3.7267E+01	177	6.7000E-02
038	3.0197E+05	108	3.2888E+01	178	5.6922E-02 41
039	2.5991E+05	109	2.9023E+01 14	179	5.0000E-02
040	2.3518E+05	110	2.5613E+01	180	4.2755E-02 42
041	2.2371E+05	111	2.2603E+01	181	3.5500E-02
042	1.8316E+05 7	112	1.9947E+01	182	3.0613E-02 43
043	1.4996E+05	113	1.7603E+01	183	2.5500E-02
044	1.4264E+05	114	1.5536E+01	184	2.0492E-02
045	1.2907E+05	115	1.3710E+01 15	185	1.2396E-02 44
046	1.1109E+05	116	1.2099E+01 16	186	6.3247E-03
047	8.6517E+04	117	1.0677E+01	187	2.2769E-03
048	6.7379E+04 8	118	9.4225E+00	188	7.6022E-04
049	5.2474E+04	119	8.3153E+00 17	189	2.5399E-04
050	4.0868E+04	120	7.3382E+00 18	190	1.0000E-04 45
051	3.6066E+04	121	6.8680E+00		
052	3.1828E+04	122	6.4760E+00 19		
053	2.8088E+04	123	5.7150E+00 20		
054	2.6058E+04	124	5.0435E+00 21		
055	2.4788E+04	125	4.4509E+00 22		
056	2.1875E+04	126	3.9279E+00 23		
057	1.9305E+04	127	3.4663E+00		
058	1.7036E+04	128	3.0590E+00		
059	1.5034E+04	129	2.6996E+00		
060	1.3268E+04	130	2.3824E+00 24		
061	1.1709E+04	131	2.1024E+00		

The 112-group library has boundaries that are the following sub-set of the 190 groups:

1-110, 132, 190

062	1.0333E+04	132	1.8554E+00 25	Range	Groups
063	9.1188E+03 9	133	1.7896E+00		
064	8.0473E+03	134	1.7261E+00	Fast	001-063
065	7.1017E+03	135	1.6592E+00		
066	6.2673E+03	136	1.5949E+00	Reso	064-132
067	5.5308E+03	137	1.5246E+00		
068	4.8810E+03	138	1.4574E+00 26	Up-scatt	127-190
069	4.3074E+03	139	1.3806E+00		
070	3.8013E+03	140	1.3079E+00		

The HELIOS code validation database consists of critical experiments calculations (101 Uranium lattices, 30 MOX lattices, TRX1, KRITZ-BA, KRITZ-MOX BWR mock-up, VIP-MOX PWR mock-up, Hexagonal TIC lattices), measured isotopics (Yankee Rowe benchmark, OECD/NEA Isotopic Prediction Benchmark), benchmarks (Mosteller Doppler, OECD/NEA WPPR, IAEA Pu/Th, WPPR Inert Matrix Fuel, MCNP comparisons for fuel assemblies and cores), etc.

2.3.2. Neutron cross section and fission spectra

For most of the components, the macroscopic cross sections in HELIOS are calculated from:

$$\Sigma_x = \sum_{i=1}^{I} N_i \sigma_{xi} \tag{1}$$

where, for component i, σ_{xi} is the microscopic cross section of type x, and N_i its number density, including the density-correction factor of the region. For a given component i, the library contains cross section tabulations at more than one temperature. Then its microscopic cross section of the type x at temperature T is obtained by the linear interpolation, according to:

$$\sigma_x(T) = \frac{T_j - T}{T_j - T_{j-1}} \sigma_x(T_{j-1}) + \frac{T - T_{j-1}}{T_j - T_{j-1}} \sigma_x(T_j) \tag{2}$$

where T_{i-1} and T_j are the nearest tabulation temperatures below and above T. If T is smaller than the lowest tabulation temperature, T_1 or greater than the highest, T_j, Eq. (2) would become an extrapolation. To avoid this, either j-1=1 or j=J is used.

Two types of gamma cross sections are also calculated by HELIOS code: the cross sections that describe the interactions of gammas with matter and the (n,γ) production matrix, which describes the gamma production due to neutron interaction with the nuclei of a material. At each reactivity point, for each material and at each energy group, the following macroscopic cross sections are calculated by HELIOS:

Table 2. Neutronic data calculated by HELIOS.

Σ_g	total	Σ_{0g}	P_0 scattering
Σ_{ag}	absorption	Σ_{1g}	P_1 scattering
Σ_{rg}	removal	$\Sigma_{tr,g'\to g}$	P_0-scaterring matrix
Σ_{fg}	fission	$\Sigma_{1,g'\to g}$	P_1-scaterring matrix
$(\nu\Sigma_f)_g$	fission-neutron production	χ_g	fission spectrum

$(\kappa\Sigma_f)_g$ fission-energy production	

All of the above data, except for the fission spectrum, are macroscopic cross sections, calculated according to Eq. (1), with the microscopic cross sections interpolated or obtained from resonance calculations.

2.3.3. Resonance treatment in HELIOS code

The energy dependence of the cross sections in the library has been discretized dividing the energies into ranges, from 10 MeV to 10^{-4} eV (see Table 1). These cross sections have been obtained by flux-averaging the point cross sections. Groups and spectra have to be chosen so that the library cross sections are insensitive to the variations of the flux spectra in their anticipated range of application. But this procedure is impractical for the resonance isotopes in the range from about 100 keV to about 1 eV. In that range, the cross sections exhibit many resonances and hence behave so wildly that thousands of energy groups would be required in order to satisfy the energy discretization.

The main task of the resonance calculations is to find for each resonance isotope in each resonance group its effective group-averaged absorption cross-section, $\hat{s}_a$, regardless of the shape of the region. In HELIOS, the expression used to find $\hat{s}_a$ is (Casal et al, 1991)

$$\hat{s}_a = \frac{\int_{\Delta u} s_a(u) f(u) \mathrm{d}u}{\int_{\Delta u} f(u) \mathrm{d}u} \cong \frac{\sum_n w_n s_n f_n}{\sum_n w_n f_n} \tag{3}$$

In Eq.(3) $f_n = f(s_n)$ are the fluxes at discrete values of s_a, s_n, which represent the (seven) subgroups into which the s range has been subdivided. According to the subgroup method, the same set of weights and cross-sections can be used for numerator and denominator. These sets, the subgroup constants, are stored in the nuclear-data library for each resonance isotope, in each resonance group, for about five different temperatures. They have been obtained by a least-square fits to exact values of the integral in the numerator of Eq.(3), the resonance integral.

To evaluate $\hat{s}_a$ it suffices to find the seven fluxes f_n in each region of the system, e.g. an RBMK assembly. First, four flux calculations with four different absorption cross-sections s_m of the resonance absorber yield four fluxes f_m in each region, from which an effective so-called background cross-section $s_{b,m}$ is found according to the relation:

$$f_m = \frac{s_{b,m}}{s_m + s_{b,m}} \Rightarrow s_{b,m} = \frac{s_m f_m}{1 - f_m} \tag{4}$$

The first term of the Eq.(4) expresses the balance: sources = losses, or: in-scattering = absorption + out-scattering. In formula: $s_{b,m} = (s_m + s_{b,m}) f$. Here the

flux above a resonance has been normalized to unity, while it is assumed that there is a single type of resonance isotope so that the microscopic cross-sections refer to that isotope. In that case, the background cross-section can be written as

$$\sigma_{b,m} = \frac{1}{N}\left(\sum_i N_i \lambda_i \sigma_{pi} + \Sigma_{e,m} \right) \tag{5}$$

In Eq.(5), N is the number density of the resonance isotope and the summation is over all isotopes i in the region. Further, $\lambda_i \sigma_{pi}$ is the product of the intermediate resonance factor (Sehgal and Goldstein, 1966) and the potential scattering cross-section of isotope i. In the case of an infinitely narrow resonance λ=1, i.e. any scattering will remove the neutron from that resonance; at the same time any neutron scattered into the resonance comes from outside (zero self-scattering). In the case of an infinitely wide resonance λ=0, i.e. all scattering is self-scattering - there is no out- nor in-scattering. Each isotope has for each energy group in the resonance range its $\lambda_i \sigma_{pi}$ in the library.

$\Sigma_{e,m}$ in Eq.(5) is the so-called macroscopic equivalence cross section of the region. It represents the heterogeneity of the region with the resonance material, e.g. a fuel pin. For a homogeneous material (infinite region) $\Sigma_{e,m}$=0. For a finite region there will be a contribution to the source from neutrons that slowed down outside the region into the energy width of the resonance and subsequently entered the region. Likewise, though not all scatterings remove a neutron out of the energy width of a resonance (self-scattering), these neutrons can still be lost if they leave the region. The fact that the same $\Sigma_{e,m}$ can be used to describe the contribution to the source as well as the contribution to the losses is a consequence of the so-called equivalence relations (Dresner, 1956; Chernick and Vernon, 1958).

Next, for each region of the system, interpolation in these four $\sigma_{b,m}$ gives seven $\sigma_{b,n}$. Using Eq.(4), they yield the seven subgroup fluxes for use in the quadratures of Eq.(3).

So far, only a single resonance absorber has been considered. Usually, however, there are several resonance absorbers in the system, e.g. U-235, U-238, Pu-239 and the dysprosium isotopes. In that case, they are grouped together in resonance categories and for each category the above outlined process is repeated. This yields for each category its own set of $\sigma_{b,m}$ values. The predominant resonance absorber U-238 is always put in a category of its own to avoid unduly shielding of the other resonance isotopes that are present in much smaller concentrations.

Finally, in a material that contains a mixture of resonance isotopes, $\hat{\sigma}_{ai}$ of a given resonance isotope i is found by assuming that the effective cross-sections of the other resonance isotopes j act as a background cross-section. Using Eqs (3) and (4), this assumption leads to the following expression for $\hat{\sigma}_{ai}$:

$$\hat{s}_{ai} = \frac{\sum_n w_{ni} \frac{s_{ni} s_{b,ni}}{s_{ni} + s_{xi} + s_{b,ni}}}{\sum_n w_{ni} \frac{s_{b,ni}}{s_{ni} + s_{xi} + s_{b,ni}}} \tag{6}$$

where

$$s_{xi} = \frac{1}{N_i} \sum_{j \neq i} N_j \hat{s}_{aj} \tag{7}$$

Equations (6) and (7) imply an iterative process. The initial set of $\hat{s}_{aj}$ values was obtained without the interaction of the other resonance isotopes, i.e. $s_{xi} = 0$. When introduced in Eq.(7) they produce s_{xi} values which, when used in Eq.(6), give the second set of $\hat{s}_{aj}$ values; et cetera.

HELIOS accounts also for the fact that the flux depression caused by the resonance absorption extends to neighboring regions that may not contain resonance isotopes. Typically, the flux dip in the fuel pins extends, though weaker, to the clad and even the coolant outside the fuel pins. This slightly reduces the scattering out of the resonance groups and is described by a correction factor. The correction is small and is based on the assumption that below 100 eV the flux dip is caused by a single resonance in the lethargy center of the resonance group, and above 100 eV by a uniform resonance distribution inside the group.

2.3.4. Transport calculations in HELIOS

In HELIOS, two or three particle-transport calculations are required per reactivity point. The first is done as a part of the resonance treatment to obtain the fluxes from which the lethargy dependence of the equivalent cross sections is established: the second yields the neutron fluxes from which the power distribution and the reaction rates for burnup are obtained. The third is optional, it gives the gamma fluxes from which the gamma-smearing effect on the power distribution and gamma-detector responses are evaluated.

To solve the transport equations its variables must be discretized. The energy variable is discretized by dividing the energy range of interest into groups. The transport method in HELIOS is called CCCP method (Current Coupling – Collision Probability). The system is partitioned into a number (L) of space elements (Villarino and Stamm'ler, 1996). The space elements are discretized into flat–flux regions i. The peripheries of the space elements are discretized into flat–current segments, at each of which the angular currents are discretized into cosine-current sectors. The fluxes, currents and sources are volume and segment–sector integrated. The fluxes ϕ in all the regions of the system can be written as linear combinations of the sources Q in all the regions and the in-currents j^- at all the sectors of the system:

$$f = XQ + Yj^- \tag{8}$$

Here X and Y are diagonal matrices of L×L blocks. Each block is a local matrix of a space element and has vectors X_i or Y_s as columns.

The in-currents in the Eq. (8) are solved by current coupling. The out-currents at all the sectors of the system can be written as a linear combination of all sources and in-currents (Villarino and Stamm'ler, 1996):

$$j^+ = EQ + Tj^- \tag{9}$$

where E and T are diagonal block matrices of L×L blocks and each block is the local matrix of a space element and has the vectors E_i or T_s as columns.

The multiple-flight coefficients of the CCCP equations (8) and (9) are obtained form the first–flight probabilities. The sources are due to in scattering, including fission for neutrons and pair production for gammas. Finally, in- and out- currents are related to the current continuity condition (out-current at a sector is an in-current at another sector):

$$j^+ = Hj^- \tag{10}$$

In Eq. (10) H is a sparse, square matrix with as many rows as the total number of sectors in the system, and only one non-zero entry per row.

2.4. Estimation of reactivity coefficients

Reactivity is the quantity, which describes the multiplying properties of a reactor as a whole. In principle, a full core calculation is required to compute this parameter and the relevant contributions.

In order to assess how a part of a core (e.g., a fuel bundle) would behave from the neutronics point of view under a given change of conditions, the coefficients can also be assessed on a cell level, without the lengthy core calculations. On this level, the infinite multiplication factor for the cell can be used to compute reactivity. Assuming the reactivity change between two states of the infinite system, the reactivity coefficient α associated with the change in a property x is defined as:

$$a_x = \frac{\partial r}{\partial x} \approx \frac{\Delta r}{\Delta x} \tag{11}$$

Thermal reactors of current interest are heterogeneous, i.e. the fuel and moderator are separate. In this case, a distinction has to be made between the fuel temperature coefficient and moderator temperature coefficient of reactivity (Glasstone and Sesonske, 1994). The fuel and moderator coefficients are generally different in magnitude, and sometimes in sign because they depend upon entirely different characteristics of the system.

2.4.1. Fuel temperature reactivity coefficient

As a consequence of the Doppler effect, the resonance peaks are broadened and neutron resonance absorption is increased with increase in temperature. Since resonance capture occurs primarily in U-238, at least in thermal reactors fueled with

natural or moderately enriched uranium, Doppler broadening will reduce the resonance escape probability. This is a negative contribution to the fuel temperature coefficient. The fuel temperature coefficient has a relatively large negative value in all thermal reactors employing either natural or moderately enriched uranium as fuel. The fuel temperature coefficient is affected by the changes of the fuel burnup.

2.4.2. Moderator temperature reactivity coefficient

The moderator temperature coefficient has a significantly higher time delay constant than the fuel temperature coefficient, i.e. the time required for a temperature change to produce an appreciable change in reactivity is much longer for a moderator.

For RBMK fuel the moderator temperature coefficient is determined by the thermal utilization (without taking into account poisons and other impurities), which can be written as:

$$f = \frac{V_F \Sigma_{aF}}{V_F \Sigma_{aF} + V_M \Sigma_{aM} Rf} = \frac{\tilde{N}_F}{\tilde{N}_F + \tilde{N}_M R_s Rf} \qquad (12)$$

where

$$Rf \equiv \frac{f_M}{f_F} \text{ and } R_s = \frac{s_{aM}}{s_{aF}}$$

and $\tilde{N}$ terms are equal to VN, the total numbers of fuel and moderator nuclei in the reactor. Thus, the moderator temperature coefficient is determined by the effect of the temperature on the R_ϕ, R_σ and $\tilde{N}$ terms.

The quantity R_ϕ is called the disadvantage factor for thermal neutrons and is the ratio of the thermal flux in the moderator to the thermal flux in fuel. Due to the large neutron absorption in the fuel, R_ϕ is larger than unity, but it decreases towards unity as the temperature increases. Therefore, it provides a positive contribution to df/dT.

The cross section ratio R_σ increases with temperature if the reactor fuel consists of U-235 and U-238, and the moderator's absorption cross section exhibits a 1/v behavior. That is because the neutron-flux spectrum hardens with increasing moderator temperature which causes more neutrons to be absorbed by the U-238 resonances. This constitutes a negative contribution to df/dT. However, the Pu-239 produced from U-238 during reactor operation may cause df/dT to become positive for the same reason as mentioned in Section 2.4.1. Because the spectrum hardening is here more significant than in the case of the fuel temperature coefficient, df/dT eventually becomes positive with burnup. In other words: as burnup proceeds, the increase of R_σ with increasing temperature in fresh fuel, eventually turns into a decrease of R_σ with increasing temperature as burnup advances; the initial negative df/dT becomes positive. Some compensation will be provided by the Pu-240 formed by the Pu-239 (Glasstone and Sesonske, 1994).

Since a relatively long time, which is required for a change of the moderator temperature, compared to the fuel temperature change, a positive moderator coefficient is generally not a hazard. Such a positive reactivity contribution develops so slowly that it can be readily controlled.

2.4.3. Power coefficient of reactivity

For the practical purposes, power coefficient of reactivity is commonly used instead of the temperature coefficients. The power coefficient is a composite quantity, which, besides the isothermal coefficient allows also for the temperature difference between the fuel and moderator, which depends on the power level and for other quantities, like poisoning, which may also vary the reactor power.

2.4.4. Void effect

The voiding of the coolant changes the effectiveness of moderator and thus the reactivity of the LWR. The effect of the voiding is complex. E.g. for the RBMK type reactors, where the moderator is graphite, the additional voiding reduces neutron absorption in the coolant and therefore might lead to a positive reactivity coefficient.

2.5. Development and validation of RBMK-1500 Neutron Cross Section library

The neutron cross section data library for the RBMK-1500 type reactor was calculated using the HELIOS code. The library comprised 2 energy groups and 25 various types of cells over the whole range of reactor conditions (graphite temperature from 300°C to 1500°C; fuel temperature from 300°C to 2100°C: coolant density from 0.001 to 1.0 g/cm^3; fuel burnup from to 0 to 30 MWd/kg).

Two models were developed for the HELIOS calculation of RBMK-1500. The first model represents the fuel cell. During the calculations of cross sections the fuel cell was treated as a stand-alone cell with mirror boundary conditions.

A second model was developed to facilitate calculations of the cross sections of the non-fuel assemblies. These cells have to be surrounded by 8 fuel cells (sources of neutrons). An example of the HELIOS mesh for the control rod (shown at left bottom) is given in Figure 1. Using this model, homogenized macroscopic cross sections for non-fuel assemblies, were condensed to two energy groups. The advantage of such a model is that it imitates the true situation of a control cell surrounded by fuel cells. The graphite temperature was assumed to be uniform in the whole macro-cell.

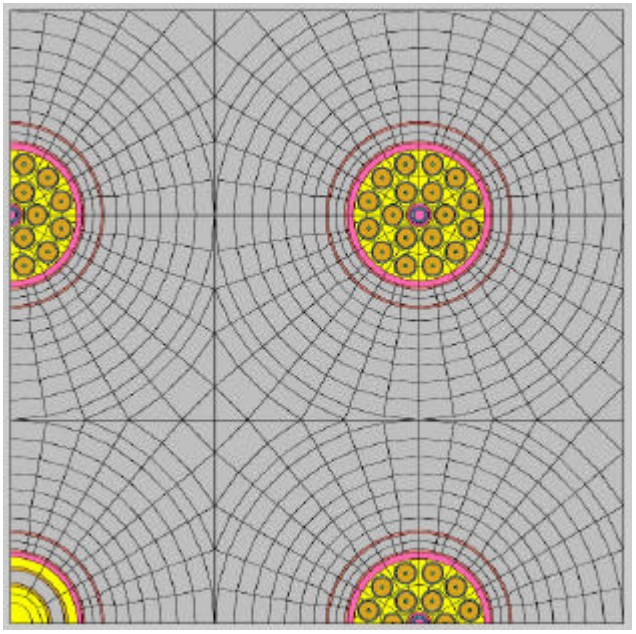

Figure 1. Illustration of a quarter of 3×3 macro-cell mesh model used in the HELIOS calculations.

2.6. Results of HELIOS calculations

The cross section library for RBMK-1500, generated with HELIOS code was benchmarked with the WIMS-D4 code library, implemented in the Russian neutron kinetics code STEPAN, which is used for routine RBMK-1500 plant calculations.

The HELIOS library was also validated by performing 3-D neutronic calculations with the CORETRAN code and comparing with measured data. The RBMK Critical Facility experiments were modeled with CORETRAN and calculated with two neutron cross section data libraries: WIMS-D4 (as the reference library for comparison) and the new HELIOS library.

2.6.1. Comparison of HELIOS and WIMS-D4 results

2.6.1.1. Single cell models – cold conditions

The Experimental Critical Facility tests were carried out at room temperature. The set of cross sections was generated with the HELIOS code for various lattice configurations. Several fuel assembly types were present in the Experimental Critical Facility (ECF) tests (containing 1.8 %, 2.0 % and 2.4 % enriched fuel). Also, different fuel assembly designs were employed (assemblies with and without the additional spacer grids). Accordingly, all these different fuel assemblies and non-fuel channels with control rods, rod imitators, water columns, etc. were modeled and calculated with the HELIOS.

The HELIOS code calculation results were benchmarked against these performed with the WIMS-D4 code. Since the cross sections, calculated at a single burnup,

temperature and coolant density point are not sufficient for drawing conclusions about the correctness of the model, HELIOS calculations over the whole range of the so-called 'cold' reactor conditions were carried out. The calculation conditions were defined as follows:

Coolant density 1.0-0.78 g/cm^3;
Fuel temperature 300-557 K;
Graphite Temperature 300-557 K.

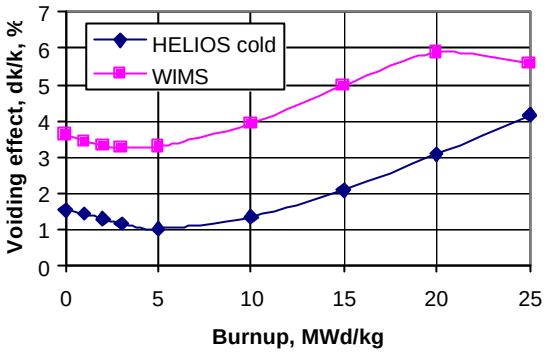

Figure 2. Void reactivity effect for the cold reactor conditions.

Figure 2 presents void reactivity effect calculation results obtained from both HELIOS and WIMS-D4 codes. The effect is calculated as:

$$a_v = \frac{k_{\inf 1} - k_{\inf 2}}{k_{\inf 1}}, \% \qquad (13)$$

Where

$$k_{\inf} = \frac{n\Sigma_{f1} \cdot \Sigma_{a2} + n\Sigma_{f2} \cdot \Sigma_{s12}}{\Sigma_{r1} \cdot \Sigma_{a2}} \qquad (14)$$

As it is shown on the Figure 2, HELIOS predicts substantially lower void reactivity effect compared to the WIMS-D4 code results. The same trend exists also for the 'hot' reactor state (at the temperatures above 557K); only the difference between the two effects in the 'hot' state is about 1% (in the void reactivity effect; see the next section). For the cold conditions the difference increases up to ~2%. The analysis of the data had shown that both codes provide very close predictions for the k_{inf} when a sufficient amount of coolant is present in the fuel channels (Figure 3). But at a high void content in the channel, HELIOS estimates lower k_{inf} than the WIMS-D4.

The fuel and graphite temperature reactivity coefficients are calculated using the following formulas:

$$a_f = \frac{k_{\inf 1} - k_{\inf 2}}{T_{f1} - T_{f2}} \qquad (15)$$

$$a_g = \frac{k_{\inf 1} - k_{\inf 2}}{T_{g1} - T_{g2}} \qquad (16)$$

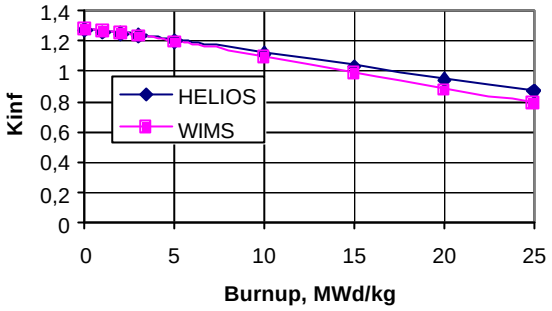

Figure 3. k_{inf} comparison for channel with coolant (coolant density 1.0 g/cm³).

There is one limitation for the WIMS-D4 neutron cross section library in the domain of the cold reactor conditions: the fuel and graphite temperatures were set to be equal (while the coolant density was varried) during the generation of the cross sections for the 'cold' (T=300-557 K) reactor conditions. This means, that it is not possible to perform fuel temperature variations while keeping the graphite temperature constant and vice versa.

The coefficients, calculated using this methodology are shown in Figure 4. They are different from the 'hot' reactor state coefficients (for the 'hot' conditions, the fuel and graphite temperatures change independently). The reason for the change in the methodology for the WIMS-D4 cross section generation was the assumption, that during reactor startup (cold reactor state) the fuel and graphite temperatures are equal to each other. But this is not necessarily true, since graphite and fuel are at the isothermal state only before the reactor startup. Later on, due to different properties, such as the specific heat and heat transfer coefficients, the temperatures do not behave in a similar way: the fuel temperature increases (and decreases) faster than the graphite temperature.

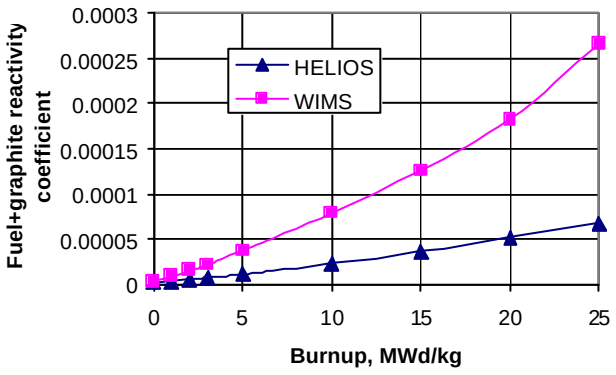

Figure 4. Fuel and graphite temperature reactivity coefficients, calculated assuming $T_f=T_g$.

Thus, for the WIMS-D4 code, the coefficient calculation methodology changes, when changing from cold to hot operational conditions. This creates a discontinuity in the values of the coefficients when switching between cold and hot conditions.

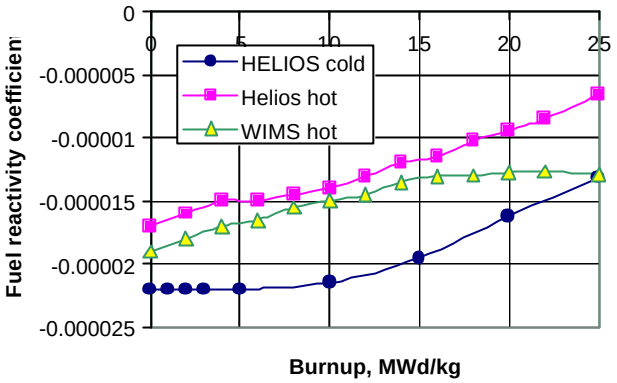

Figure 5. Fuel temperature reactivity coefficient, calculated assuming independent variation of T_f and T_g.

In order to employ the same methodology over the whole temperature range the HELIOS cross section library was generated making independent variations on fuel and graphite temperatures so that independent fuel and graphite temperature reactivity coefficients can be obtained.

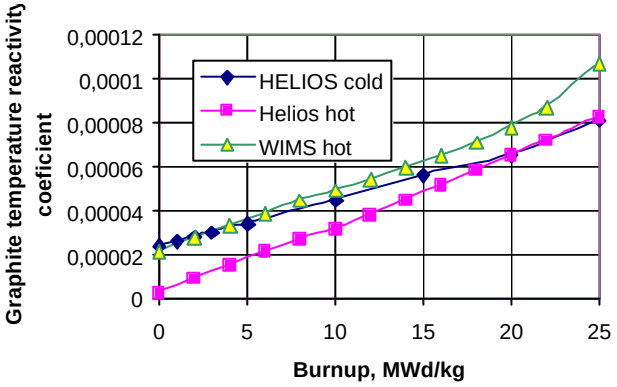

Figure 6. Graphite temperature reactivity coefficient, calculated assuming independent T_f and T_g.

Figure 5 shows the fuel temperature reactivity coefficient, calculated by HELIOS employing the above-described methodology where the graphite temperature was kept constant.. Here, the series 'HELIOS cold' were calculated for the cold temperature range, i.e. T_f between 300 and 557 K. In this Figure the HELIOS and WIMS-D4 generated fuel temperature reactivity coefficients for 'hot' reactor conditions (above 557 K) are presented. In the case of the independent temperature variation the reactivity coefficient different in value and in sign is obtained (compare with Figure 4).

The graphite temperature reactivity coefficient, calculated using independent variations of fuel and graphite temperatures, is in a close agreement with the case when $T_f=T_g$ (compare Figure 6 and Figure 4).

2.6.1.2. Single cell models – hot conditions

Recently, the reactor units at the Ignalina NPP have been loaded with two main fuel types: 2.0% and 2.4% U-235 enriched fuel (with 0.41% Erbium admixed as burnable absorber). Erbium is introduced to reduce the positive void reactivity coefficient, which is a specific feature of RBMK reactors. Recently also 2.6% U-235 enriched fuel has been introduced with additional 0.5% of Erbium. And in the future use of 2.8% enriched fuel is planned. This would help to reach an even lower positive void reactivity coefficient and will allow increased burn up of the fuel in the reactor. The HELIOS neutron cross sections were generated for all the types of fuel assemblies, which are, or will be, present in the reactor. The HELIOS calculation results were compared with WIMS-D4 code results.

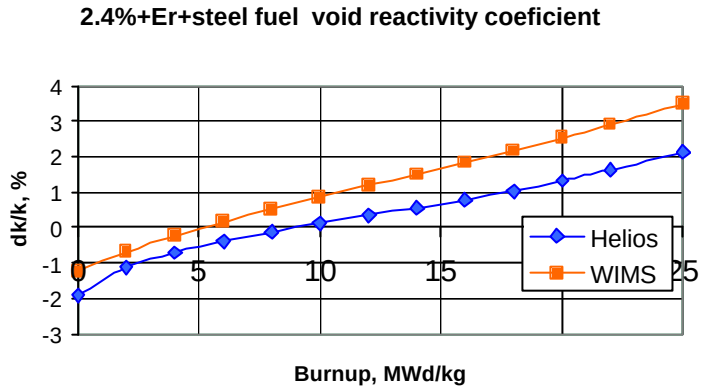

Figure 7. Void reactivity effect in the fuel cell.

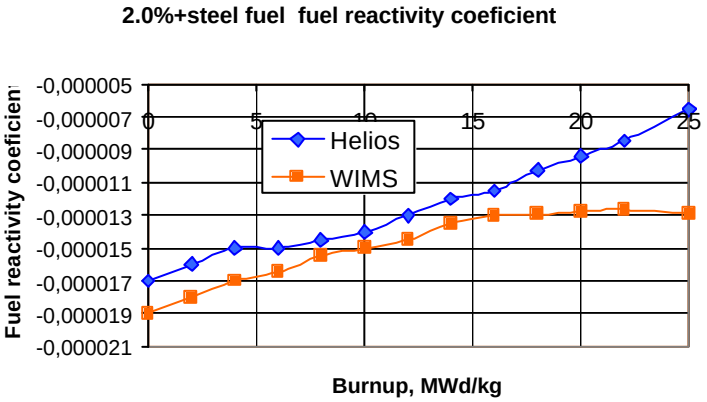

Figure 8. Comparison of HELIOS and WIMS-D4 results for fuel temperature reactivity coefficient calculations.

Figure 7 presents the void reactivity effect calculated by HELIOS and WIMS-D4. As is seen from Figure 7, HELIOS predicts a lower void reactivity effect than WIMS-D4. As it was already discussed in the previous sub-chapter, both codes provide very close predictions for k_{inf} when there is a considerable amount of coolant present in the fuel channels. But for a high void content, HELIOS estimates lower k_{inf} than the WIMS-D4 code.

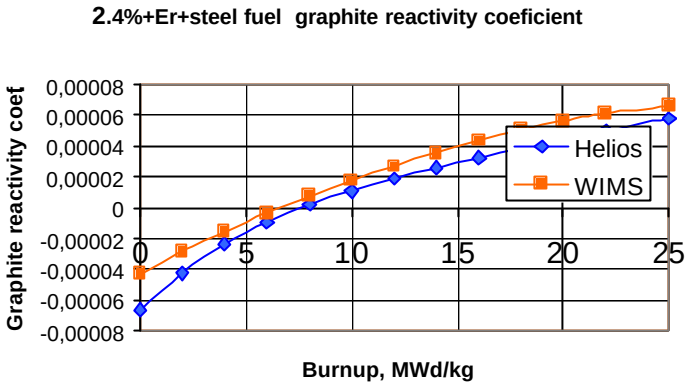

Figure 9. Comparison of graphite temperature reactivity coefficient.

An example of the fuel temperature reactivity coefficient is presented in Figure 8. The difference in the predicted coefficients between the two codes grows as the fuel burn up increases. But for the average burnup value (which for the RBMK-1500 reactor core is 11 MWd/kg) the agreement between the predictions of the two codes is rather good. The graphite temperature reactivity coefficient (Figure 9) calculated by HELIOS agrees well with the WIMS-D4 code predictions.

2.6.1.3. Multicell models

To generate cross section data for non-fuel channels (control rod, additional absorber, axial detector, etc.), 3x3 multicell models were used (Figure 1).

Table 3. Comparison of HELIOS and WIMS-D4 calculated cross sections for MCR absorber.

Const.	With coolant in CPS			Without coolant in CPS		
	WIMS-D4	HELIOS	Discre-pancy, %	WIMS-D4	HELIOS	Discre-pancy, %
D_1	1,0792	1,1053	*2,4%*	1,1229	1,1477	*2,2%*
D_2	0,8102	0,7991	*-1,4%*	0,8579	0,8499	*-0,9%*
$S_{1->2}$	5,6859E-03	5,9661E-03	*4,7%*	3,4931E-03	3,8057E-03	*8,2%*
S_{a1}	2,4187E-03	2,5686E-03	*5,8%*	2,6128E-03	2,7714E-03	*5,7%*
S_{a2}	5,6704E-03	5,7513E-03	*1,4%*	6,3767E-03	6,2588E-03	*-1,9%*

For the non-fuel cell calculations, the sets of neutron cross sections were obtained by varying graphite temperature and coolant density in the surrounding fuel channels, and also the coolant density in the non-fuel channel. The HELIOS results for different cross sections were compared to the WIMS-D4 code calculations. The example comparison for the Manual Control Rod (MCR) lattice cross sections is presented in the Table 3.

In general, as can be seen from the example in the Table 3, the HELIOS calculated cross sections for all non-fuel cell types are in close agreement with those of WIMS-D4, with the discrepancies remaining below 10% for all the non-fuel assemblies types.

2.6.2. Assessment against Experimental Critical Facility (ECF) experiments

2.6.2.1. General description

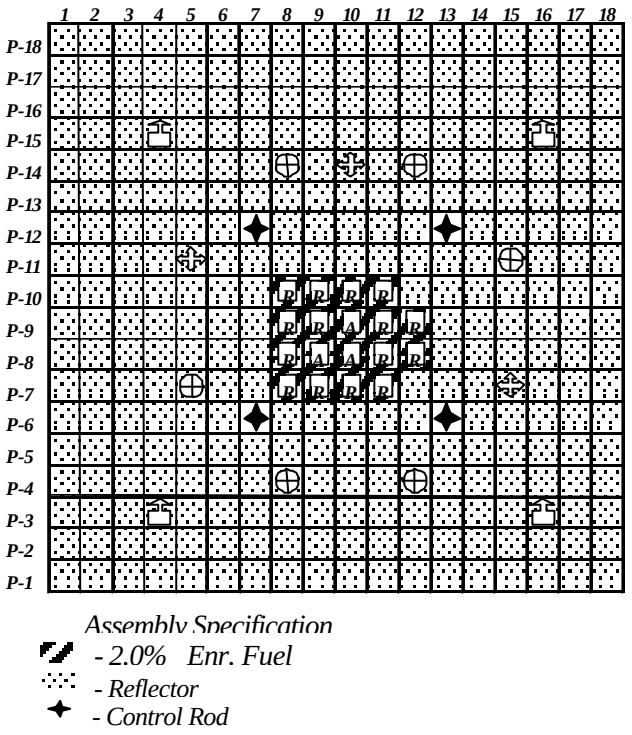

Figure 10. Experiment A1 core loading map.

A number of experiments was carried out at the RBMK Experimental Critical Facility of the RRC Kurchatov Institute. The experiments were carried out with small configurations of up to 22 fuel assemblies and large configurations of over 200 fuel assemblies and other structures. Different measurements were carried out during the experiments. This Chapter summarizes the validation of the HELIOS cross section data library and presents a comparison with WIMS-D4 results. The neutronic calculations for the critical experiments were carried out with the code CORETRAN, using both HELIOS and WIMS-D4 generated cross section data libraries.

2.6.2.2. Experiments with small number of fuel assemblies

The first five experiments were conducted with 14-22 fuel assemblies of different design and fuel enrichment and 4 control rods. A typical layout of the facility for these experiments is given in
Figure 10. Fuel channels were either filled with coolant or empty during the experiments. The following sections discuss the results of the simulation for this type of experiments.

Excess criticality with control rods fully withdrawn

Several measurements were performed to evaluate the excess criticality for the system with control rods fully withdrawn. The usual experimental procedure to evaluate the total system criticality was to sum the partial reactivity values, i.e.: to withdraw some of the control rods while keeping the position of the other control rods unchanged. Excess criticality for the system with all control rods fully withdrawn was determined as a sum of several independent measurements. Calculation results with HELIOS and WIMS-D4 cross section sets are given in Table 4.

Table 4. Excess criticality calculation results.

Exp. No.	Experimental reactivity value, β_{eff}	HELIOS, β_{eff}	WIMS, β_{eff}
A1-1	0.23	0.255	0.57
A2-1	0.19	0.15	-
A3-1	0.23	0.22	0.289
A4-1	*0.23*	*0.388*	*0.532*
A5-2	-0.38	-0.498	-0.492

The data, presented in Table 4, shows a close agreement between experimental results and calculations performed using the HELIOS generated cross section data, except for the experiment A4-1, where both HELIOS and WIMS-D4 cross section sets provide a large overestimation of the system reactivity. This is due to the lack of information on the initial conditions (i.e. the insertion depth of the control rods) for this particular experiment. Since the initial insertion depths were not given in the experimental report (Davidova, et al, 1995), the initial conditions (criticality) were established by inserting control rods into the core in CORETRAN model, until k_{eff} was equal to unity. This was considered as an initial state. Control rods were fully withdrawn from this state.

Experiment A5-2 showed a negative reactivity for the ECF after the removal of the control rods, because in addition to the removal of the control rods one fuel assembly was also removed from the Critical Facility during the experiment.

Radial and axial neutron flux distribution

The radial neutron flux distributions were measured at critical conditions. All four cases, calculated with CORETRAN, resulted in a very good agreement between

experimental and calculated values. As the results of the four experiments are very similar, only the results for one experiment (A1-2) are presented here.

Results of CORETRAN calculations using the HELIOS cross sections and deviations from the experiment data are presented in Figure 11. The radial neutron flux distributions, calculated with WIMS-D4 generated cross section data, are shown in Figure 12.

80,0	**100,0**	**104,0**	**92,0**		**Measured**
76,9	*97,8*	*103,1*	*90,9*		*Calculated*
-4,0	*-2,3*	*-0,8*	*-1,2*		***Discrepancy, %***
95,0	**123,0**	**129,0**	**112,0**	**82,0**	
94,1	*120,8*	*128,0*	*112,2*	*82,5*	
-0,9	*-1,8*	*-0,8*	*0,2*	*0,6*	
93,0	**121,0**	**127,0**	**111,0**	**79,0**	
93,0	*120,1*	*127,4*	*111,6*	*81,6*	
0,0	*-0,8*	*0,3*	*0,6*	*3,2*	
74,0	**90,0**	**98,0**	**90,0**		
73,4	*95,8*	*101,7*	*89,2*		
-0,8	*6,0*	*3,6*	*-0,9*		

Figure 11. Experiment A1-2 radial neutron flux distributions. HELIOS cross sections.

The calculated axial neutron flux distributions (see the example in Figure 13 also agree well with the experimental data, both with HELIOS and with WIMS-D4 cross section libraries.

80.0	**100.0**	**104.0**	**92.0**		**Measured**
76.4	*96.9*	*101.6*	*89.0*		*Calculated*
-4.7	*-3.2*	*-2.4*	*-3.4*		***Discrepancy, %***
95.0	**123.0**	**129.0**	**112.0**	**82.0**	
94.2	*121.1*	*127.5*	*112.6*	*81.8*	
-0.9	*-1.6*	*-1.2*	*0.5*	*-0.2*	
93.0	**121.0**	**127.0**	**111.0**	**79.0**	
94.2	*121.0*	*127.4*	*112.5*	*81.7*	
1.3	*0.0*	*0.3*	*1.4*	*3.4*	
74.0	**90.0**	**98.0**	**90.0**		
76.4	*96.7*	*101.3*	*88.8*		
3.1	*7.0*	*3.3*	*-1.4*		

Figure 12. Experiment A1-2 radial neutron flux distribution. WIMS-D4 cross sections.

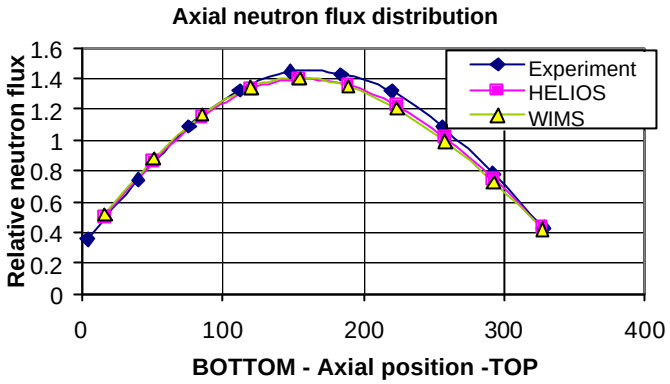

Figure 13. Axial neutron flux distribution.

Changes in the system configuration

During this experiment a fuel assembly was moved from one channel location to another. All channels with fuel assemblies were filled with coolant.

Experimental reactivity value was $\rho=0.20\ \beta_{eff}$.
Calculations using HELIOS cross sections provided $\rho=0.229\ \beta_{eff}$.
WIMS-D4 cross sections predicted $\rho=0.23\ \beta_{eff}$.

Channel pipe efficiency

This excess criticality measurement was performed after removal of one fuel assembly from the facility and removal of the aluminum pipes from the channels that surround the core. All control rods were withdrawn during this test.

Experimental reactivity value was $\rho=0.12\ \beta_{eff}$.
CORETRAN calculations using HELIOS cross sections yielded $\rho=0.20\ \beta_{eff}$ reactivity.
No comparison with the WIMS-D4 cross section data was made for this case as the employed WIMS-D4 library did not include the cross section data for aluminum pipes.

Coolant voiding effect

Experiments started at critical conditions, with the control rods partially inserted into the core. Then the coolant was drained from the fuel channels. At the same time, the control rods were fully withdrawn.

Experimental value for the voiding effect of fuel assemblies is $\rho=-4.6\ \beta_{eff}$.
CORETRAN calculations (with HELIOS cross sections) provided $\rho=-2.07\ \beta_{eff}$.

Fuel assembly effectiveness

In order to measure the efficiency of one fuel assembly, the assembly was removed from its channel; the control rods were fully withdrawn and all fuel assembly channels were drained.

Experimental reactivity of the system was $\rho = -1.26\ \beta_{eff}$. Calculations employing both HELIOS and WIMS-D4 data resulted in underprediction of the reactivity value.

HELIOS calculations gained $\rho = -0.81\ \beta_{eff}$ reactivity.

WIMS-D4 cross sections resulted in $\rho = -0.843\ \beta_{eff}$ reactivity.

Fuel assembly effectiveness with control rods inserted

The 2.0% enriched fuel assembly was removed from a channel. The position of the control rods was kept unchanged.

Experimental value for reactivity after the fuel assembly was removed: $\rho = -1.06\ \beta_{eff}$.

Calculations with HELIOS cross section library: $\rho = -1.156\ \beta_{eff}$.

WIMS-D4 calculations resulted in $\rho = -0.436\ \beta_{eff}$.

2.6.2.3. Large core configuration experiments

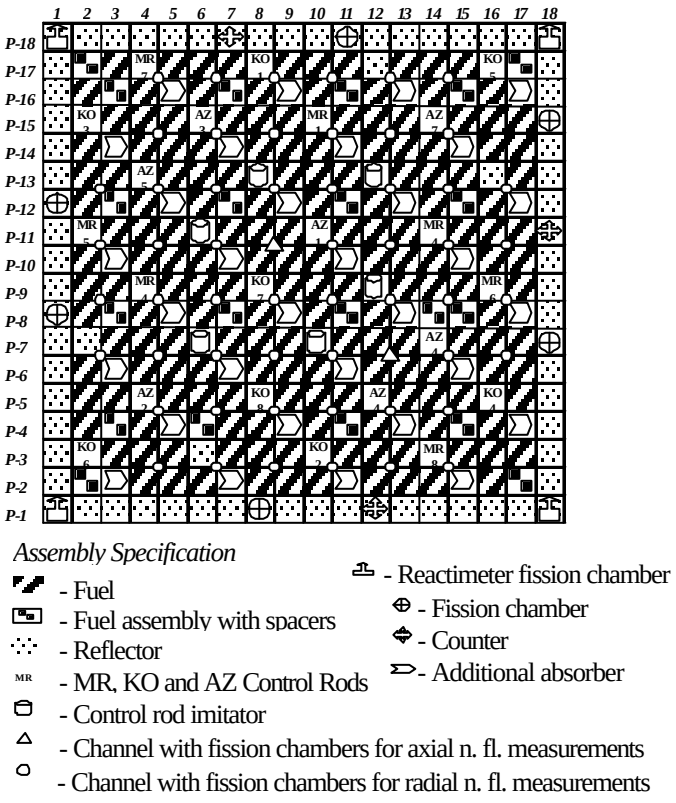

Figure 14. Experiment A11 core loading map.

The remaining tests in the Experimental Critical Facility represent more complex parts of the prototypic RBMK core. The facility layout includes fuel assemblies of different design and enrichment (e.g. with and without the additional spacer grids), control rods, additional absorber rods, control rod imitators (control rods whose axial position cannot be changed), etc. An example of the Critical Facility composition for large core configuration experiments is presented in Figure 14.

Excess criticality

A series of system criticality measurements were carried out for the larger critical assemblies. The conditions, which preceded the measurements, were different for each experiment. Table 5 presents a summary of the experiment simulations and comparisons.

Table 5. Comparison of excess reactivity experimental measurements with calculated results.

Exp. No.	Experimental, β_{eff}	HELIOS, β_{eff}	WIMS, β_{eff}
A6-1			
Rod P13-8	0.12	0.097	0.083
Rod P7-10	0.14	0.10	0.084
Rod P11-6	0.12	0.118	0.083
Rod P9-12	0.15	0.123	0.083
Total:	***0.53***	***0.438***	***0.333***
A7-1			
Rod P15-10	0.26	0.258	0.284
-"- and P5-8	0.51	0.472	0.566
-"-andP11-14	0.75	0.682	0.856
P5-8&P11-14	0.49	0.44	0.55
A8-1	0.17	0.193	-
A9-1	0.12	0.149	0.17
A10-1	-0.14	-0.147	-
A11-1	0.30	0.34	0.458

Four control rods were present in the experimental core configuration of experiment A6-1: total excess reactivity was estimated to be the sum of the partial reactivities, introduced by the removal (one–by–one) of all the control rods. For this experiment, CORETRAN predicted a slightly lower 'weight' for the control rods with both HELIOS and WIMS-D4 cross section libraries.

In experiment A7-1, the system reactivity was measured after the insertion of several control rods into the core. In this case an underprediction was obtained for the control rod weight with HELIOS cross sections and an overprediction with WIMS-D4 cross sections. During the experiments A8-1 and A9-1 one control rod was moved. In the experiment A10-1 all control rods were withdrawn during the subcriticality measurements. In addition to this, one fuel assembly was removed from its channel. This resulted in a negative system reactivity. Test A11-1 evaluated the system criticality after having all the control rods, except one, fully inserted into the core. The last control rod was inserted gradually, until the system was made critical. After this

the same rod was fully removed from the core. System criticality was measured at this state.

Neutron flux distribution

For the large ECF core configurations, radial and axial neutron flux distributions were measured during some experiments.

	8	9	10
P15	**75.7** *88.0* *14.0*	**53.8** *50.0* *-7.6*	**64.3** *66.1* *2.7*
P13	**90.8** *102.8* *11.7*	**76.9** *73.0* *-5.3*	**77.2** *75.2* *-2.7*
P11	**87.3** *91.3* *4.4*	**139.0** *138.0* *-0.7*	**112.2** *111.7* *-0.4*
P9	**116.5** *118.7* *1.9*	**153.0** *148.6* *-3.0*	**103.1** *94.7* *-8.9*
P7	**91.4** *93.6* *2.4*	**118.7** *109.2* *-8.7*	**128.5** *129.5* *0.8*
P5	**104.9** *107.5* *2.4*	**133.0** *125.5* *-6.0*	**123.1** *124.9* *1.4*
P3		**90.9** *93.3* *2.6*	**59.2** *58.0* *-2.1*

Measured
Calculated
Discrepancy, %

Figure 15. Experiment A11-2: radial neutron flux distribution. HELIOS cross sections.

As all the CORETRAN experiment calculations gave similar results, the results of the experiment A11-1 are presented here (the core configuration is shown in Figure 14).

The measurements were carried out in 20 fuel channels. CORETRAN calculation results based on HELIOS cross sections are presented in Figure 15, while Figure 16 presents based on WIMS-D4 generated cross sections. The radial neutron flux distributions obtained are similar to the HELIOS results.

For all the experiments, where the axial neutron flux distribution was measured, CORETRAN predictions using both HELIOS and WIMS-D4 generated cross sections, are close to the experimental values. An example of a comparison between the experiment and the CORETRAN calculations with HELIOS and WIMS-D4 data is given in Figure 17.

	8	9	10
P15	**75.7** *88.8* *14.7*	**53.8** *49.9* *-7.8*	**64.3** *65.8* *2.2*
P13	**90.8** *103.4* *12.2*	**76.9** *72.5* *-6.1*	**77.2** *74.5* *-3.6*
P11	**87.3** *91.7* *4.8*	**139.0** *137.9* *-0.8*	**112.2** *110.9* *-1.2*
P9	**116.5** *119.1* *2.1*	**153.0** *148.5* *-3.0*	**103.1** *94.5* *-9.1*
P7	**93.9** *92.3* *-1.7*	**118.7** *109.0* *-8.9*	**128.5** *129.4* *0.7*
P5	**104.9** *108.3* *3.1*	**133.0** *125.9* *-5.6*	**123.1** *125.0* *1.5*
P3		**90.9** *93.6* *2.9*	**59.2** *57.8* *-2.4*

Measured
Calculated
Discrepancy, %

Figure 16. Experiment A11-2: radial neutron flux distribution. WIMS-D4 cross sections.

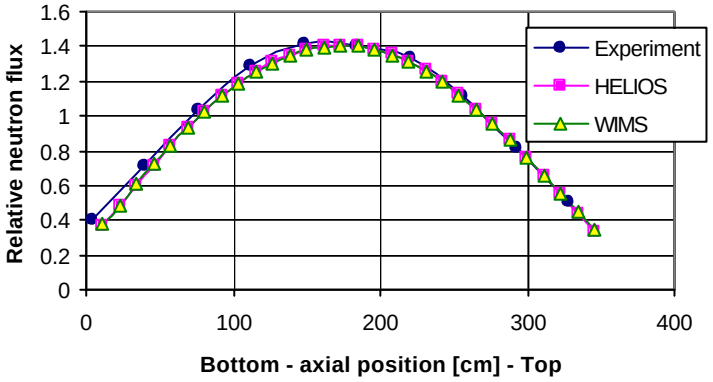

Figure 17. Axial neutron flux distribution.

Fuel assembly efficiency

An additional fuel assembly of 1.8 % enrichment was loaded into a fuel channel. There was no coolant in the channel. The rest of the fuel channels (23 channels) were filled with coolant.

Experimental reactivity after that assembly was removed from the channel: ρ=-1.18 β_{eff}.

CORETRAN calculations with HELIOS cross section data: ρ=-0.746 β_{eff}.
1.8% enriched fuel data was not available with the WIMS-D4 library.

System voiding effect

Three system-voiding measurements were carried out:

1. Experiment A7-2. During this experiment coolant was drained from all 45 fuel assemblies and 4 additional channels. The initial sub-criticality of the system was: ρ=-1.3 β_{eff}.

Experimental voiding effect: $\Delta\rho$=-2.9 β_{eff}.
HELIOS input resulted in $\Delta\rho$=-1.66 β_{eff}.
WIMS-D4 result: $\Delta\rho$=-0.939 β_{eff}.

2. Experiment A8-2. The coolant was removed from all 71 fuel assembly channels in the subcritical state. Additional absorber channels were also without coolant. The initial system subcriticality was equal to: ρ=-0.22 β_{eff}.

Experimental coolant voiding effect: $\Delta\rho$=-2.41 β_{eff}.
CORETRAN calculated reactivity with HELIOS data: $\Delta\rho$=-1.93 β_{eff}.
CORETRAN calculated reactivity with WIMS-D4 data: $\Delta\rho$=-1.59 β_{eff}.

3. Experiment A9-3. Control rod imitators were removed from three channels. The coolant was removed from all the fuel channels. All the control rods were fully withdrawn.

Experimental reactivity value for the voiding of all fuel channels: ρ=0.14 β_{eff}.
CORETRAN results with HELIOS cross sections: ρ=0.162 β_{eff}.

Effect of filling the system with coolant

In this experiment the fuel channels were filled with water. Two control rods were partially inserted into the core. During the first part of the experiment the system reactivity with the control rods fully withdrawn was determined. Each control rod was withdrawn separately while keeping the position of the other control rods unchanged. System reactivity was calculated for the withdrawal of one control rod. The total reactivity of the system without control rods was determined as the sum of the reactivities of the separate withdrawals.

System reactivity for the withdrawal of the first control rod: ρ=0.20 β_{eff}. For the withdrawal of the second rod the reactivity was ρ=0.19 β_{eff}. Sum reactivity for the control rods fully withdrawn: ρ=0.39 β_{eff}. Experimental value for the filling of the fuel channels with water: ρ=-0.14 β_{eff}.

Results for the calculations with HELIOS data: reactivity for the withdrawal of the first control rod P: ρ=0.237 β_{eff}. Reactivity for the second rod withdrawal: ρ=0.245

β_{eff}. Sum reactivity: ρ=0.482 β_{eff}. For the fuel channels filled with water: ρ=-0.148 β_{eff}.

Results obtained with WIMS-D4 data: reactivity for the first rod withdrawal ρ=0.158 β_{eff}. Withdrawal of the second rod: ρ=0.119 β_{eff}. Sum reactivity: ρ=0.277 β_{eff}. Fuel channels filling with coolant: ρ=-0.66 β_{eff}.

Effect of voiding the additional absorber channels

In these experiments, the fuel channels were filled with water. Coolant was removed from the additional absorber channels. Results for the voiding effect calculations are presented in Table 6.

Table 6. Additional absorber channel voiding.

Exp. No.	Experimental, β_{eff}	HELIOS, β_{eff}	WIMS, β_{eff}
A7-3	-1.67	-0.895	-0.939
A9-4	-0.75	-0.86	-1.29

For the first test A7-3, CORETRAN gave almost two times lower values for the voiding effect for the additional absorber channel voiding. In the second test, the results with HELIOS cross sections were close to the experimental data, while using WIMS-D4 cross sections resulted in a large error compared to the experiment data.

Effect of filling the control rod imitator channel with coolant

The effect of filling the channels with the control rod imitators with coolant was measured having the control rods fully inserted into the core.

Experimental reactivity value: ρ=0.31 β_{eff}.
CORETRAN calculations using the HELIOS cross sections: ρ=0.253 β_{eff}.
WIMS-D4 data predicted ρ=0.38 β_{eff} reactivity.

2.7. Major findings and accomplishments

A neutron cross section library for RBMK-1500 fuel was generated with the HELIOS code. The HELIOS calculation results were benchmarked with WIMS-D4 code. The WIMS-D4 cross section library used for the comparison is employed in the STEPAN code calculations of the RBMK-1500 reactor.

The HELIOS cross section data were validated against the RBMK Critical Facility experiments, performed at the RRC Kurchatov Institute.

For fuel and graphite reactivity coefficients, and void reactivity effects for various types of fuel in the RBMK-1500 reactor core, the results obtained with HELIOS data are similar to those obtained with WIMS-D4 data. Both codes provide similar values for the fuel and graphite temperature coefficients as well as the voiding effect of fuel assemblies under hot reactor conditions. There are discrepancies between the HELIOS

and WIMS-D4 calculated results for the cold reactor conditions due to the differences in methodologies, used for WIMS-D4 and HELIOS data generation (the fuel and graphite temperatures were assumed to be equal: no independent temperature variations for the cold conditions during WIMS-D4 calculations). HELIOS gives lower k_{inf} values for the voided states than WIMS-D4, although for fuel assemblies filled with coolant both their k_{inf} values are similar. This results in a lower void reactivity effect when HELIOS cross section data are used.

HELIOS results for the non-fuel cell calculation are in good agreement with the WIMS-D4 code results, with the deviations for all types of the non-fuel channel macroscopic cross sections being less than 10%.

Critical experiments, performed on the Experimental Critical Facility of the Kurchatov Institute (Russia) were calculated with the CORETRAN code. The neutron cross section data used by CORETRAN, both for fuel and non-fuel cells, were calculated by HELIOS. In total, 25 sets of cross section data were generated. The calculation results were compared to CORETRAN/WIMS-D4 calculations. The main conclusions of this work are:

1. There is an acceptable level of agreement with the experimental data for the CORETRAN calculations, performed using HELIOS cross sections for criticality state calculations, control rod reactivity worths, fuel assembly reactivity worths, channel pipe efficiency, the effect of filling fuel channel and control rod imitators with coolan and radial/axial neutron flux distribution measurements.
2. In the case of core voiding, system voiding, additional absorber channels voiding and control rod voiding experiments, the CORETRAN calculated effects with both HELIOS and WIMS-D4 cross sections, are significantly lower, than the experimental values. Calculations with HELIOS cross section sets provided better agreement with the experimental data.
3. In general, the HELIOS cross section library provides better results for 3-D neutronics calculations of the Critical Facility experiments than the WIMS-D4 library; even though the WIMS-D4 cross sections have already been 'corrected' to better fit the experimental results.
4. The methodology employed in the WIMS-D4 cross section library for 'cold' reactor conditions provides large discrepancies of the fuel and graphite temperature reactivity coefficients between the 'cold' and 'hot' reactor state calculations. The methodology used for the generation of HELIOS library provides consistent results in all the temperature range (both cold and hot conditions).

Chapter 3

VIPRE-02 code development and assessment

3.1. Objectives

The aim of this work was to assess the thermal-hydraulic part of the CORETRAN code package (code VIPRE-02) for the RBMK-1500 type reactor applications. Similar to the most of the up-to-date codes, CORETRAN was initially intended for the Western-type LWR calculations, where the heated length of the fuel rods is almost one half of that in the RBMK-1500 (the two fuel assemblies in the RBMK fuel channel comprise about 7 m of the heated length). Therefore, the existing VIPRE-02 CHF and post-CHF correlations were assessed and new RBMK-1500 reactor-specific correlations were implemented into the VIPRE-02 code.

The assessment was carried out in 2 stages: first, the CHF and post-CHF heat transfer correlations were validated against long single-channel heated tube experiments, which were carried out at KTH, Stockholm and EREC, Russia. Afterwards, the VIPRE-02 sub-channel model of the RBMK-1500 fuel channel was developed and the calculations using the various CHF correlations were validated against the CHF experiments for the RBMK-1500 fuel assemblies, which were performed at the RRC Kurchatov Institute in Russia.

Three additional CHF correlations were implemented into the VIPRE-02 code: Osmachkin correlation, which is used for the lower fuel assemblies of the RBMK-1500, RRC KI correlation for the upper fuel assemblies in the RBMK-1500 fuel channel, and Khabenski correlation, which is based on VVER and RBMK fuel assembly experimental results for low coolant mass fluxes.

The CHF calculation results with VIPRE-02 were additionally benchmarked against RELAP5/MOD3.3 calculations. The RELAP5 code is widely used in the system thermal hydraulic analysis of various reactor types (including RBMKs).

3.2. Introduction and background

The Critical Heat Flux (CHF) is the heat flux, at which the sudden deterioration of the heat transfer rate occurs. As the result the LWR fuel element surface temperature would increase at a constant heat generation rate. The CHF is of critical importance in the reactor safety assessment, since the temperature rise of several hundred degrees could occur at the heated surface, which most likely will cause the failure of the cladding (Sesonske, 1973).

Many terms had been used to define the CHF conditions (Todreas and Kazimi, 1989). The departure from nucleate boiling (DNB) is the term originally used to describe the CHF conditions in pool boiling; also it can be encountered in flow boiling when the bubble formation is rapid enough to cause a continuous vapor film to form at the wall. Dryout is the term, reserved for the liquid film dryout in an annular flow.

3.2.1. CHF at low quality (DNB)

For the flow boiling, a nucleate boiling regime exists for the low-quality flow conditions. In the case of a high heat flux, a vapor blanket may occur on the surface. When this occurs, the surface temperature rises rapidly to a high value. The overall CHF increases with the increase of mass flux (Tong and Weisman, 1970).

3.2.2. CHF at high quality (dryout)

At high quality flow conditions, mostly vapor exits the core of the reactor. The flow pattern is usually annular and a liquid layer covers the heated surface. When the evaporation rate reaches high enough values, dry patches may develop in the liquid layer, as the increasing vapor velocities drag portions of surrounding liquid, and the CHF occurs. Since the velocity of the vapor core is higher, the heat transfer in this case is larger than that for the low quality cases. Therefore, in the dryout case the wall temperature rises are lower and less rapid, compared to the DNB cases (Tong and Weismann, 1970).

3.2.3. CHF at cross flows

For the cases, where the cross flows exists between the fuel bundles (e.g. in the PWR type reactors), the heat transfer coefficients for the cross flows are higher than for the parallel flow, e. g., Coffield et al (1967) examined the CHF in a crossed-rod matrix with the Freon 113 coolant and found that the critical flux is about 200% higher for the cross flow compared to the parallel flow cases. Therefore, the flow mixing increases the CHF. This practice was used also for a RBMK plant (RRC KI, 1971) upper assemblies, to upgrade the reactor power from 1000 to 1500 MW_e for the RBMK-1500.

3.2.4. CHF at low mass flows

The CHF at low flow rates is important for the reactor transient analysis in some accident regimes, such as RCS depressurization (Khabenski, et al, 1998), etc. The CHF mechanisms at zero or low flow conditions can differ from those for the high mass flux velocities.

3.2.5. Post-CHF heat transfer

After the critical heat flux has been exceeded, the flow regime (transition boiling) may consist of entrained droplets in a central vapor core (Sesonske, 1973). Droplets,

striking the wall are evaporated if the wall temperature is below the Leidenfrost temperature. However, if the wall temperature exceeds the Leidenfrost point, no wetting of the wall occurs and the stable film-boiling mode of heat transfer is established.

The post-CHF region may occur in the reactor operations by design (e.g. in heat exchangers operating in the once-through mode, where superheated vapor exits the steam generator). The post-CHF region could occur at the off-normal operating conditions in the reactor core, after the CHF is exceeded (Yoo and France, 1996). Thus, the knowledge of this region is important to determine the clad temperatures for reactor safety analysis and assessment.

3.3. Prediction of CHF and post-CHF heat transfer

Three types of methods are used for the CHF prediction: semi-empirical theoretical models, empirical correlations and look-up tables (Cheng et. al, 1997).

The CHF phenomena are in general governed by the heat and mass transfer processes which occur under the two-phase flow conditions. Thus, only having adequately described these processes one hopes to create a realistic (semi-empirical) physical model, which is capable of predicting the critical heat flux. This problem is still far from being solved, as the number of the local parameters, which are to be taken into account, is very large, even for the simple flow conditions. If the influence of each parameter is non-linear, even neglecting the parameters with little influence, this can still result in a correlation with up to 243 empirical coefficients (Olekhnovitch et al, 1999).

A better representation of the CHF might be obtained by using certain parameters, which will be affected by the same physical mechanisms as the critical heat flux. The CHF is dependent on the geometrical configuration as well as on the thermal-hydraulic conditions, such as the pressure, mass flux, steam quality, power distribution, fuel rod configuration and diameter, pitch to rod diameter ratio, axial power distribution, spacers, etc.

A number of phenomenological models has been developed for the relevant physical processes, which lead to the CHF. Many of the published models are based on the postulated mechanisms and cannot be verified directly due to difficulties in performing direct flow visualization for the near-wall region at high heat fluxes approaching CHF. Several different mechanisms were postulated for the DNB region: e.g. 'boundary layer separation model' was proposed by Kutateladze et al (1966). The method postulates that CHF is caused by the flow stagnation due to the vapor injection from the heated wall. The 'near wall bubble crowding model' was proposed by Weisman and Pei (1983). In this case the turbulent interchange between the bubble layer and the core region is the limiting mechanism for the CHF onset. In 1988 Lee and Mudawar proposed the 'liquid sublayer dryout method', according to which a thin liquid sublayer exists beneath the vapor blanket flowing over a heated surface. Dryout in the liquid sublayer occurs then the sublayer mass loss due to evaporation exceeds that of the liquid entering the sublayer from the core region. Several mechanistic

models were suggested based on this concept by Katto (1990), Celata et al (1998, 2000), Liu et al (1999), etc. The main difference between these models is the calculation of the thickness of the vapor blanket.

The dryout mechanism is better understood, compared to the DNB. The flow rate of the liquid film is determined by the evaporation, droplet entrainment and droplet deposition. CHF corresponds to the condition in which the film flow rate falls to zero. The dryout process was first described by Whalley et al (1974) by the means of so-called 'annular flow model'. This model was extended by Hewitt at al (1990) and a good agreement between the model and the test data for uniformly heated tubes was obtained.

A large number of empirical correlations have been developed during the last several decades but, in spite of a great quantity of available experimental data and theoretical studies, the knowledge of the CHF is still incomplete. Since the correlations have been developed for particular CHF conditions and particular flow geometries and conditions, they cannot be used outside their domain of application. The extrapolations of the correlation results may lead to high uncertainties (Groenevald, 1995, Hall and Mudawar, 2000, etc.).

Nowadays a huge amount of data is available in different flow channel geometries and for different fluids. Basing on this data, more than 700 CHF correlations were developed during the last several decades (Groenevald, 1996).

Among the correlations available, the W-3 (Tong, 1967), Levitan (Levitan, 1975), Kato (1984), Shah (1987), EPRI (1972), Bowring (1973) correlations are often used.

For the rod bundle flow geometries the CHF results can be predicted either by the sub-channel or bundle average flow conditions (Cheng, 1997). The use of the sub-channel method is more favorable since it allows the better understanding of the physical mechanisms, which cause the CHF. The use of sub-channel CHF correlations requires use of a sub-channel code, as the inter-channel mixing strongly affects the results of the empirical models. Also, the accuracy of the CHF prediction in the sub-channel code is closely coupled with the accuracy of the determination of the sub-channel flow conditions by the code.

The other approach to standardize the empirical correlations is to employ the CHF look-up tables. This method was applied mostly in Canada and Russia and was assessed by a large number of researchers (Becker et. al, 1992, Baek et al, 1995, Cevolani, 1997, etc.).

The look–up table method is used at the Chalk River Nuclear Laboratory (Groenevald, et. al, 1986), at the Institute of Physics and Power Engineering in Russia (Kirilov, et. al, 1989, 1995), etc. The look-up tables are usually developed for a fixed tube diameter (e.g., of 8 mm) and the application is extended to different diameters or geometries by using the geometry correction factors (Cheng et. al, 1997).

The CHF at low-pressure low-flow (LPLF) conditions received much interest and a number of investigations were carried out for this flow region. The CHF phenomenon becomes more complex under the LPLF conditions, as an important role is played by buoyancy forces, flow instabilities, test loop design parameters, etc. (Khabenski et al, 1998, Kim, et al 2000). One of the first correlations for the LPLF conditions was developed by Lowdervik et al (1958). The later works of Mishima et al (1985), Mishima and Nishihara (1987), etc. involved systematic experimentation under the LPLF conditions, emphasizing buoyancy effects and inlet flow throttling. The CHF experiments and correlations were also conducted and presented by Weber and Johannsen (1990), Chang et al, (1991), Kirilov (1994), etc.

The research in the post-CHF area covers a variety of conditions. A compilation of the research results can be found in (Hewitt et al, 1993). In general, three types of modeling approaches for the post-CHF region were attempted (Park, 2003):

(i) Empirical correlations, where no assumption about the post-CHF mechanisms are made and only functional relationships between the independent variables and heat transfer coefficient are described;

(ii) Correlations, which treat the departure from thermal hydraulic equilibrium conditions and attempt to calculate 'true' vapor quality and temperature, different from T_{sat};

(iii) Semi-theoretical models, which attempt to examine and derive the equations for individual hydrodynamic and heat transfer processes, occurring in the heated channels. Groenevald (1973) compiled a bank of post-dryout data in tubular, annular and rod bundle geometries.

3.4. VIPRE-02 code

VIPRE-02 code, incorporated in the CORETRAN package for thermal hydraulic analysis and the thermal hydraulic feed back to the neutronic analysis, contains 6 equations for mass, energy and momentum variables of liquid and vapor fields. Homogeneous Equilibrium Model (HEM) could be used if desired. Method of Characteristics (MOC) numerics could also be employed as an option for e.g. BWR stability analysis. Both HEM and two-fluid models can be employed in the 3-D rod bundle sub-channel analysis with estimation of cross flow across the lateral contact between sub-channels. Both models are designed to perform steady state and transient calculations under normal operational conditions and wide range of abnormal events and accidents. Information, available from HEM and two-fluid models includes fluid velocity and state, pressure drop, rod temperatures, heat transfer coefficients, critical heat flux (CHF), critical power ratio (CPR), departure from nucleate boiling ratio (DNBR), etc. (EPRI, 1997). Statistical analysis on the occurrence of CHF also can be performed in order to derive the operational set points.

Several CHF and CPR correlations are available in VIPRE-02. The CHF correlations include major vendor correlations published in 1970s-1980's plus several correlations, which span over the wide range of both BWR and PWR operating parameters (EPRI, 1997). Among these are Babcock & Wilcox (Gellersted, et al, 1969), Westinghouse W-3 (Tong, 1967), Bowring (Bowring, 1979), EPRI (EPRI,

1982) and other correlations. A capability to incorporate user-defined correlations into VIPRE-02 code is provided.

For PWR (high pressure) conditions, three correlations are available in VIPRE-02:

(i) Babcock & Wilcox #2 CHF correlation (Gellersted et al, 1969). The correlation predicts CHF in rod bundles at high pressure and high heat flux conditions.

(ii) Westinghouse W-3 CHF correlation, which was developed for PWR rod bundles and was derived using a proprietary Westinghouse sub-channel analysis code over a wide range of parameters. The correlation also takes into account the effects of grids on CHF and incorporates various grid factors, developed for standard Westinghouse grids (i.e. simple S grids, mixing vane or R/L type grids). This correlation was initially formulated by Tong (1972) and implements corrections into the original correlation for non-uniform axial heat flux and cold wall channels (EPRI, 1997).

(iii) CE-1 CHF correlation. The correlation was developed, based on the proprietary data from Combustion Engineering 14×14, 16×16 and 17×17 fuel rod bundles. It was derived for uniform axial heat flux.

For low pressure conditions (in some cases extendable also into high pressure range) the following correlations are available in VIPRE-02:

(iv) Bowring's correlations for mixed flow clusters (Bowring, 1977) and for sub-channel analysis of fuel bundles (Bowring, 1979). The correlations were developed for critical heat flux predictions during the blowdown transients in the computer code RELAP-UK and for the use with the sub-channel analysis code HAMBO (Gellersted, 1969). The correlation was validated over a large range of parameters for pressure tube reactors (PTR), BWRs and PWRs (EPRI, 1997).

(v) EPRI correlation, developed at Columbia University (EPRI, 1982). The correlation was developed using a wide range of data from BWR and PWR type fuel bundles. This is the default correlation in VIPRE-02. The correlation gives the CHF as a function of inlet subcooling, local quality, mass and heat flux. Also, spacer grid factors were incorporated into the correlation to extend the applicability of the correlation to fuel assemblies with various grid spacers.

For the post-CHF region several different correlations are implemented in VIPRE-02. The correlations could be applied over a large range of fluid parameters (EPRI, 1997).

Three transition boiling correlations are available in VIPRE-02:

(i) Modified Condie-Bengston correlation (INEL, 1978). The correlation was developed for high flow rate transition boiling.

(ii) Modified Tong-Young correlation (Tong and Young, 1974).

(iii) Bjornard-Griffith correlation (Iloeje et al, 1975). This correlation is a method to interpolate between the critical heat flux and the minimum film boiling point. The minimum film boiling heat flux is calculated using the

film boiling heat transfer coefficient from the selected correlation and continuous post-CHF boiling curve is defined.

Four film boiling correlations are implemented into VIPRE-02. Three of them:

(i) (Groenevald 5.7 (1973);
(ii) Groenevald-Delorme (1976);
(iii) Dougall-Roshenow, (1973)

were developed for a dispersed flow film boiling and take into account the vapor superheat effect on surface heat transfer rate.

The

(iv) Bromley (1950) correlation was developed for pool boiling and is accurate for low quality, low mass flux conditions.

3.5. Test Facilities

The experimental investigations have to be performed for each specific reactor design in order to assess the CHF for its different subassemblies. Due to the limitations of the technical feasibility and the economic constraints, scaling techniques are often used in the CHF experiments. Two different techniques are available: geometric modeling and fluid modeling (Cheng, 1997). In the geometrical modeling simplified flow channels, as circular tubes, instead of the rod bundles are used. The use of the simple flow channels allows the systematic studies of the different parameter effects on the CHF in a wide range of flow parameters. The use of the substitute fluids (like Freon) instead of the original fluid (water) allows the operating pressure, temperature and the required heating power to be significantly decreased.

3.5.1. Overview of the world-wide test facilities

Many test facilities had been build worldwide to perform the CHF investigations. Among the largest are the heat transfer research facilities of Columbia University (Yang, 1996), where CHF experiments in PWR, BWR and PHWR rods bundles are conducted. Two large test facilities are available at CEA for water and Freon-12 coolants (Omega and Graziella loops, Courtaud, 1988). Several test facilities exist in Russia, at IPPE, EREC and RRC KI for different purposes. There are several PWR and BWR rod bundle test facilities at NUPEC (Kitamura et. al., 1998). Large scale Freon-12 facility was built at the Research Center Karlsruhe in Germany (Cheng, 1997).

The available experimental database can be divided into several groups according to the flow geometry (circular tubes, rod bundles) and the working fluids (water, Freon).

The circular tubes are the most common geometry. Many databanks exists on this type of the experiments (Thompson and Macbeth, 1964, Becker, 1971, Celata, 1991, etc.). Also, databanks for specific purposes (transient CHF, CHF for fusion engineering, etc.) exist. Two big databanks were compiled during the 80's by

Groenevald et al, (1986) and Kirilov at al (1989), with more than 15000 data points each over a wide range of parameters. More recently, even larger data bank was derived (Groenevald et al, 1999) with more than 30000 data points.

Similar to the round tube experiments, a large number of the CHF experiments in rod bundles were carried out both in models and full-scale simulations of fuel bundles of various reactor types. Some of the test data for these experiments are proprietary and not available for public use. The data bank on the water flow in fuel bundles was compiled in the 60's (Thompson and Macbeth, 1964). The databank contains experimental data for several various rod bundle geometries. Later on, in the year 1974, Hughes compiled a CHF data base for more than 4200 data points obtained in 126 test sections (Cheng, 1997). Some years later the Columbia University (Fighetti et al, 1982) collected over 11000 data points from 235 test sections of US, British, Canadian, Japanese reactor vendors and designers into a databank, which still remains the largest databank of this kind in the world and which covers a wide range of BWR, PWR and PHWR parameters.

Regarding VVER and RBMK bundle geometry, experiments have been performed in the Eastern Europe and former Soviet Union (Bobkov, 1997). VVER rod bundle geometry data bank was created by the Czech scientists (Cizek et al, 1997). This data bank contains more than 2600 data points from 27 hexagonal test bundles. For the RBMK rod bundles a series of experiments were carried out at RRC KI and EREC during 70's and 80's.

3.5.2. KTH test loop

CHF and post-CHF measurements in electrically heated round tubes were carried out in the Department of Nuclear Reactor Technology at the Royal Institute of Technology (KTH) (Becker et al, 1983). More than 15000 heat transfer coefficients have been obtained for the post-CHF mode over a wide range of flow parameters. The main aim of the tests was to provide additional experimental data, necessary for the assessment of different correlations.

The test facility (Figure 18) was designed for operating pressures of up to 25 MPa. The test section length could be up to 7.3 m. The maximum power supply to the test section was up to 6000 amps at voltages up to 140 volts.

Before the test section, the coolant was filtered and preheated. The preheater was used to adjust the inlet water temperature. After the test section the steam-water mixture flowed through a condenser, after which the water entered a circulation pump.

Water temperature was measured before the flow meter, before the test section and after the test section. Test section temperature was measured by thermocouples, positioned at 5-20 cm distances along the test section axis. Power input was obtained by measuring current and voltage over the test section.

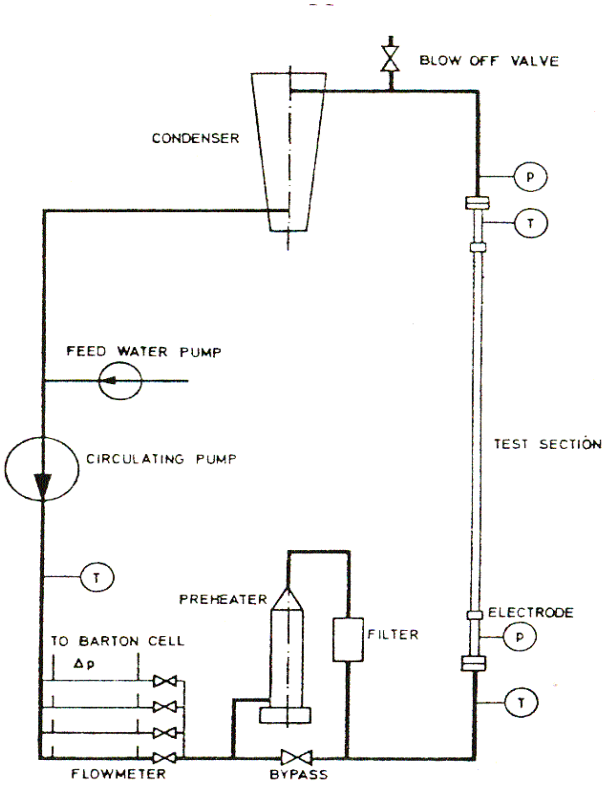

Figure 18. KTH test facility.

In the experiments, which were used for this work, the test section was 7.0 m long and had inner diameters of 0.0149 and 0.01 m. Outer diameter was 0.0208 m and 0.0140 m respectively. Inlet water subcooling at the test section inlet was 5 ÷ 10 ºC.

3.5.3. E-108 Test Facility

The Electrogorsk test facility E-108 was constructed at the Electrogorsk Research and Engineering Center (EREC), Russia. The Facility was designed to investigate flow instabilities in parallel heated tubes. Tests were conducted in the range of system pressures of 2-7 MPa and tube power input from 0.06 to 0.77 MW/m² (Urbonas, 1998). During some of the tests the CHF occurrence was recorded. We chose to analyze these tests with VIPRE-02 code.

The test section consisted of six parallel heated channels (Figure 19). The channels were connected to pumps, headers, steam separators, etc. Each channel in the test section was also connected to separate coolant communications through the header at the inlet and to steam-water piping at the outlet of the test sections. Electrical heaters were capable of producing up to 500 kW power output.

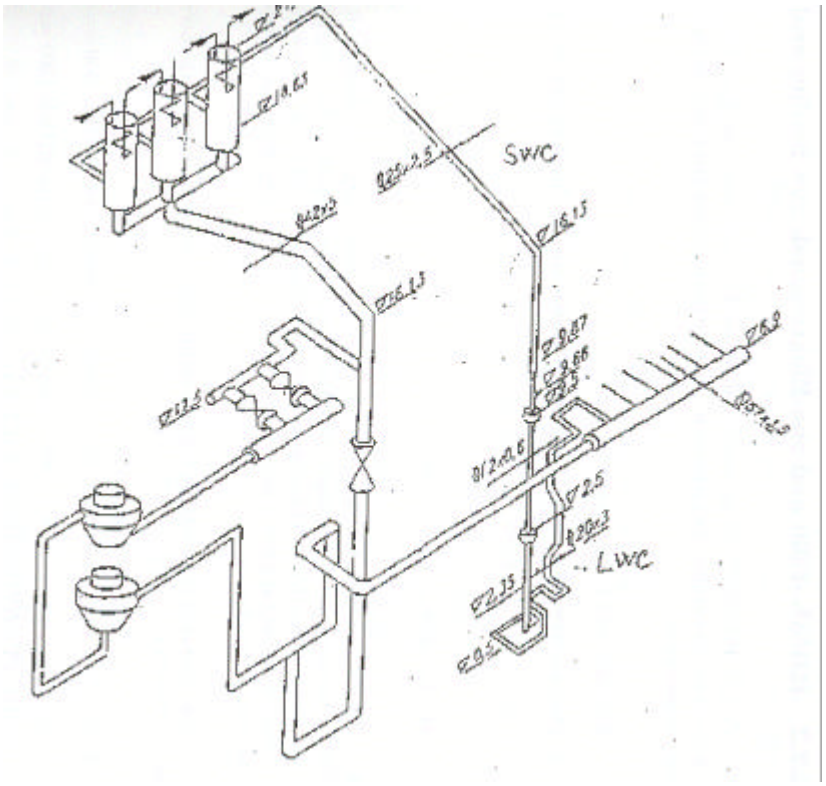

Figure 19. Electrogorsk 108 test facility.

Each test channel was 7.3 meter long; the heated section was 7.0 m long. During the experiments, performed in the years 1982 and 1984, the heated tubes were 10 mm in diameter, and of 1 mm wall thickness. Uniform axial heat flux distribution was employed during the experiments.

3.5.4. RRC KI Test Facility

The KS test facility constructed in Kurchatov Institute in 1967 included two identical models of fuel channels for the RBMK reactor (Figure 20).

The test facility consisted of two loops for high and low pressure (Osmachkin, 1974): high pressure loop was maintained at up to p=10.79 MPa (110 kgf/cm^2) and the low pressure loop was at p=0.98 MPa (10 kgf/cm^2). The loops consisted of two pumps, test sections, separators, condensers and heat exchangers. The flow rates of up to 8.5 kg/sec could be reached through each of the channels. Electrical power of the test section was up to 6 MW. The inner diameter of the fuel channel was 80 mm. Heated test section consisted of 18 rods, with the outside diameter of 13.5 mm and wall thickness of 3.5 mm and the central non-heated rod, with the outside diameter of 15 mm. Heated length of the test section was 7 m. The pressure was measured at the inlet and outlet of the test section. And the rod wall temperatures were measured in a number of elevations along the test section axis.

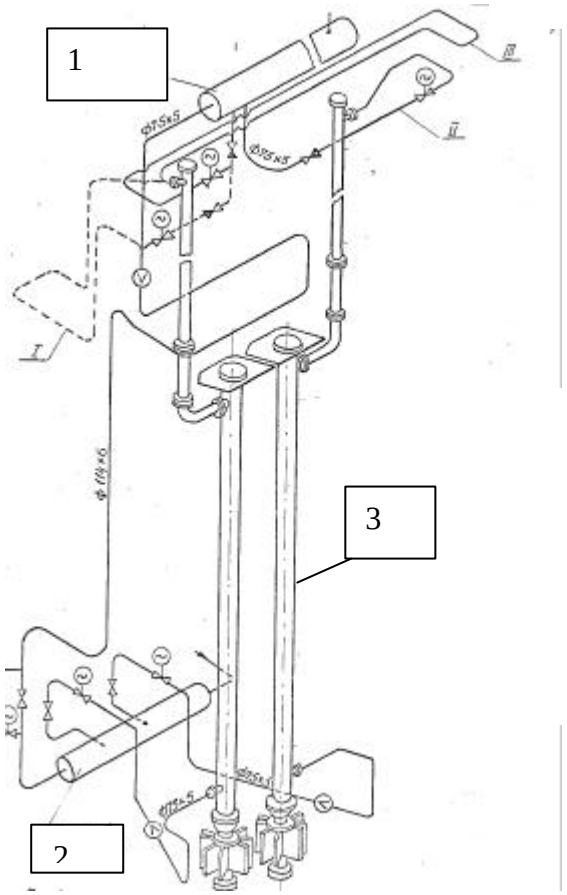

Figure 20. RBMK fuel channel models at the KS test facility. 1–upper collector; 2-lower collector; 3-RBMK fuel channel models.

The CHF conditions during the experiments were reached in two ways: either by increasing the channel power, while keeping the pressure and mass flow rate constant or by reducing the mass flow rate at constant pressure and test section power.

3.6. CHF correlations, implemented into VIPRE-02 at KTH

Additional CHF correlations, relevant to the RBMK-1500 reactor geometry and parameters, were implemented into the VIPRE-02 code. Three correlations were added to the standard code version.

3.6.1. Osmachkin correlation for lower RBMK-1500 fuel assembly

Osmachkin correlation for the lower RBMK-1500 fuel assembly (Osmachkin, 1974) is the modification of the Macbeth formula (Sesonske, 1973). The general form of the Macbeth correlation is:

$$\left(\frac{q}{A}\right)_{crit} \times 10^{-6} = A - \frac{C}{4} dGc_e h_{fg} \qquad (17)$$

where A and C are functions of mass velocity, diameter and pressure, χ_e is the quality and h_{fg} is the latent heat of vaporization. The correlation had proved to be successful for a vast amount of data in bubble and annular flow regimes.

The modified Macbeth formula is used also for the RBMK-1000 type reactor CHF analysis. Osmachkin correlation, developed on the basis of the Macbeth correlation, also includes the dependence of the CHF on viscous forces/liquid surface tension (Weber number), gravity, critical mass evaporation rate, temperature coefficient of conductivity, flow regime (Prandl and Reynolds numbers), etc.:

$$q_{cr} = \frac{2.899 \cdot (0.94 - 0.286 \cdot x_{cr} \cdot We^{1/5})}{1 + \frac{1}{3.54} \cdot \frac{1}{\Phi'(z)} \cdot \int_o^z \Phi(z) dz} \cdot rr' gd_{th} (ga)^{1/3} (\mathrm{Pr}')^{1/3} (\mathrm{Re})^{1/5} \quad (18)$$

The formula contains:

x_{cr} – critical mass evaporation rate:

$$x_{cr} = 1 - 0.86 \cdot \exp\left(\frac{-19}{\sqrt{We}}\right) \quad (19)$$

We – Weber number, calculated as:

$$We = \frac{(rw)^2}{r's} \quad (20)$$

$\Phi(z)$ – linear relative power (heat) distribution along the height of the heated channel, W/m:

$$\Phi(z) = \Phi_0 \sin \frac{p(z+d)}{H} \quad (21)$$

Φ_0 – linear heat rate in the reactor central plane, W/m:

- for maximum loaded channel

$$\Phi_0 = \frac{Q_{th} k_z}{H_0 N} \quad (22)$$

- for average loaded channel

$$\Phi_0 = \frac{Q_{th} k_v}{H_0 N} \quad (23)$$

k_v – volumetric peaking factor:

$$k_v = k_r k_z \quad (24)$$

k_r – radial peaking factor:

$$k_r = \frac{2.405 \cdot \frac{R_0}{R}}{2R \cdot I_1 \cdot \left(2.405 \cdot \frac{R_0}{R} \right)} \quad (25)$$

k_z – axial peaking factor:

$$k_z = \frac{pH_0}{2H} \sin \frac{pH_0}{2H} \quad (26)$$

H_0 – core height, m;

H – extrapolated core height, m:

$$H = H_0 + 2d \quad (27)$$

δ – effective (extrapolated) addition, m (usually δ=0.8 m for RBMK's);

Q_{th} – reactor thermal power, W;

R – core radius, m;

R_0 – core radius, taking into account effective additions (R_0=R-δ), m;

N- number of fuel channels in the core;

ρw – coolant mass flux, kg/(m^{2}s);

ρ' – water density in steam-water mixture, kg/m^3;

σ - coolant surface tension coefficient, N/m ;

Φ'(z) – relative heat release at point z, W/m ;

Φ(z) – linear energy release distribution along the height of the fuel assembly, W/m:

$$\Phi(z) = \Phi_0 \sin \frac{p(z+d)}{H} \quad (28)$$

r – latent heat of vaporization, kJ/kg;

g – gravity acceleration, m/s^2;

d_{th} – hydraulic diameter, m;

a – temperature coefficient of conductivity, m^{2}s;

Pr' – Prandl number:

$$\mathrm{Pr}' = \frac{n'}{a} \tag{29}$$

ν' – kinematic viscosity coefficient, m^2/s;

Re – Reynolds number:

$$\mathrm{Re} = \frac{r w d_{th}}{m'} \tag{30}$$

μ' – water dynamic viscosity coefficient, Pa·s.

The application range of the Osmachkin correlation (Osmachkin, 1974) is:

- pressure p=6.5 to 8.0 MPa;
- mass flux ρw=1000 to 4000 kg/m^2s;
- coolant temperature at channel inlet t_{in}=220 to 270 °C.

3.6.2. RRC KI correlation for upper RBMK-1500 fuel assembly

An extensive experimental program on the selection of flow intensifiers for the upper fuel assemblies of RBMK type reactor had been carried out at the RRC Kurchatov Institute (RRC KI) during the 80's. The aim of this program was to assess the possibility to upgrade the RBMK reactor power from 1000 to 1500 MW_{el}. The main issue for the power upgrade was to maintain the existing safety margins, such as critical power ratio.

The principal solutions to increase the power could be (RRC KI, 1977):

1. Increase the coolant mass flux through the fuel assembly.
2. Change the design of the fuel assembly.
3. Introduce the additional flow intensifiers for the fuel assemblies.

The first case would require an increase of the coolant flow rate up to 6000 kg/m^2s (vs. design value of 3000 kg/m^2s), which was not acceptable from the construction point of view.

The change of the fuel assembly design would cause serious changes in the existing reactor design and in the technological processes of the fuel assembly fabrication and was considered to be too expensive.

The introduction of the additional flow intensifiers was considered to be the most efficient way for the RBMK reactor power upgrade. In this case the only difference between the fuel assemblies of RBMK-1000 and RBMK-1500 reactors would be the additional flow intensifiers, installed on the RBMK-1500 upper fuel assemblies. Therefore, an extensive experimental program involving various types of flow intensifiers was carried at RRC KI.

The axially–twisted flow intensifiers were selected as the most suitable for the RBMK power upgrade. The experimental data for this flow intensifier type was plotted as $q_{CHF}=f(x)$, where q_{CHF} is the critical heat flux and x is the average steam quality at the fuel channel outlet. The experimental data was obtained at various coolant mass fluxes (ρw=1500-3500 kg/m^{2}s), for fuel assemblies of various lengths (2.0 and 7.0 m) and for fuel assemblies with uniform and non-uniform axial power distribution. The experimental data followed the same linear trend: the CHF was decreasing with the increase of the steam quality at the fuel channel outlet.

Therefore, it was decided to write a simple relation, using the least-square fit of the experimental date for the critical heat flux as the function of exit quality for the upper assemblies of the RBMK-1500 reactor and the RRC KI correlation was developed:

$$q_{CHF} = 2.23 - 2.05 \cdot x \ , \text{MW/m}^2 \qquad (31)$$

This relationship was validated for the parameter region:

- pressure at inlet p=6.37 -8.14 MPa;
- coolant mass flux ρw=1300-3520 kg/m^{2}s;
- coolant temperature at inlet t=210-270 °C;
- quality at exit x=0.325-0.76;
- heat flux q"=0.49-1.61 MW/m^2.

3.6.3. Khabenski correlation for low mass fluxes

Khabenski correlation was developed using the data of CHF experiments for RBMK and VVER rod bundles (Khabenski, et al, 1998).

The correlation developers were using the following physical tendencies:

1. The minimum critical heat flux at $(\rho w)_{in}$=0 is determined by the known relationships for rod bundles with no inlet mass flow (Balunov et al, 1987, Spart et al, 1987);
2. For ρw=0-300 kg/m^{2}s, CHF changes linearly;
3. CHF for ρw=300 kg/m^{2}s is defined by a relationship for rod bundles used for intermediate and high mass flux densities.

It was noted by the authors of the correlation (Khabenski, et al, 1998) that for intermediate and high mass flux densities different mechanisms of CHF are possible. As it was noted during VVER-440 fuel assembly experiments for different mass fluxes (Jukov, 1994), at the high mass flux densities, the relationship $q_{cr}=f(x_{cr})$ has three regions of alternative q_{cr} change. In the first region (low values of x_{cr}) the CHF decreases monotonically with the increase of x_{cr} (DNB region). For the second region (dryout), a steep decrease of the CHF with an increase of x_{cr} is noted (i.e. high values of the derivative $|\partial q_{cr}/\partial X_{cr}|$). The third region corresponds to the monotonous change of the CHF with x_{cr} (the so-called 'wetting crisis'). With the decrease of the mass flux density the first region of CHF grows, and at the $\rho w \leq 500$ kg/m^{2}s this first region (DNB) extends over the whole range of x_{cr} (Khabenski et al, 1998).

The correlation originates from the Smolin and Polyakov (1967) correlation, which was verified against RBMK and VVER rod bundle tests:

$$q_{cr} = 0.65A(p)(rw)^{0.2}(1-x)^{1.2} \quad (32)$$

where

$$A(p) = \begin{cases} 1.3 - 4.36 \cdot 10^{-2} p; & p \geq 3MPa \\ 1.16; & 1.0 \leq p < 3MPa \\ 1.16 p^{0.15}; & p < 1.0MPa \end{cases}$$

Khabenski et al (1998) had adopted the correlation in the following form:

$$q_{cr} = \left(1 - \frac{rw}{300}\right) q_{cr}^{T} + \frac{rw}{150} A(p)(1-x)^{1.2} \quad (33)$$

where A(p) is defined by the Eq. 32 and q_{cr}^{T} is calculated from:

$$q_{cr}^{T} = 6.75 \cdot 10^{-9} \frac{h r_v^{0.5}}{H} [sg(r_l - r_v)]^{0,,25} \quad (34)$$

The equation (33) could be applied for RBMK and VVER rod bundles for ρw=0-300 kg/m^{2}s.

3.7. VIPRE-02 calculation results

The three additional CHF correlations, described in the Section 3.6 were implemented into the VIPRE-02 code and the KTH, E-108 and RRC KI experiments were modeled. For the KTH and E-108 experiments a single heated channel VIPRE-02 model was written. CHF and post-CHF heat transfer correlations (in a single channel mode) were assessed against the experimental data. The sub-channel model for RBMK-1500 fuel assembly (consisting of 30 channels) was written for the RRC KI experiment simulation. The assessment of the CHF correlations in the sub-channel mode was carried out.

The VIPRE-02 results were benchmarked against RELAP5/MOD3.3 calculations. The RELAP5/MOD3.3 is the most recent version of the code. The RELAP5 code implements critical heat flux correlation for rod bundles based on the tabular data. Also, users can activate a new set of CHF correlations that were developed by the Nuclear Research Institute Rez in the Czech Republic (PG-CHF correlations). These correlations replace the CHF table look-up method. For the benchmarking of the VIPRE-02 calculations standard RELAP5/MOD3.3 CHF look-up table correlation was used.

3.7.1. Single channel model: KTH experiments

The calculations in the pressure range 3-20 MPa were carried out. The VIPRE-02 CHF and post-CHF correlations provide different results for the heat transfer in the

high (16-20 MPa), medium (about 7-12 MPa) and low pressure (2-3 MPa) regions and the results for each case will be discussed separately.

3.7.1.1. High pressure experiments (16-20 MPa)

For the higher pressure range (16-20 MPa) the occurrence of the CHF was predicted well with the EPRI CHF correlation, which is implemented in the standard VIPRE-02. The 16 MPa pressure corresponds to the pressure in a typical PWR.

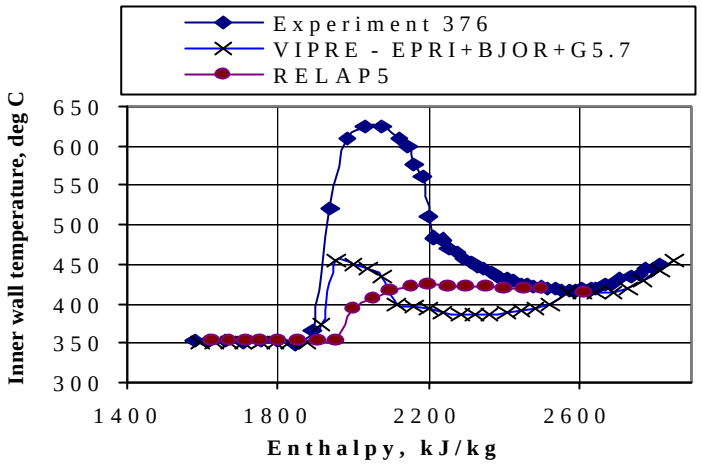

Figure 21. VIPRE02 and RELAP 5/MOD3.3 calculation results for P=16 MPa. Flow rate 2000 kg/m²s. Here EPRI-EPRI CHF correlation; BJOR - Bjornard-Griffith; COND – Condie-Bengston; DOUG – Dougall-Rohsenow; G5.7 – Groeneveld 5.7 correlations.

Figure 21 presents the example of the calculation results for some of the correlations. Close CHF predictions were obtained with both VIPRE-02 (EPRI correlation) and RELAP5 codes. For the prediction of post-CHF heat transfer, however, there is a large disagreement between the experimental data and calculation results for the transition boiling mode. Standard VIPRE-02 correlations, such as Condie-Bengston, Tong-Young and Bjornard-Griffith underpredict the wall temperatures in this flow regime by 150-200ºC. Bjornard-Griffith correlation provides the closest agreement but still the temperature difference is too high. For the film-boiling region the VIPRE-02 predictions are very close to the experimental data (Figure 21).

3.7.1.2. Medium pressure experiments (7-12 MPa)

Pressure of 7 MPa is the most interesting part of VIPRE-02 validation against CHF and post-CHF heat transfer modes in long tubes. This pressure corresponds to the nominal pressure in BWR and RBMK type reactors. The RBMK reactors have core height of about 7.0 m. Thus assessment of VIPRE-02 code predictions against the measurements would allow better estimations for CHF occurrence and post-CHF heat transfer in the RBMK type reactors.

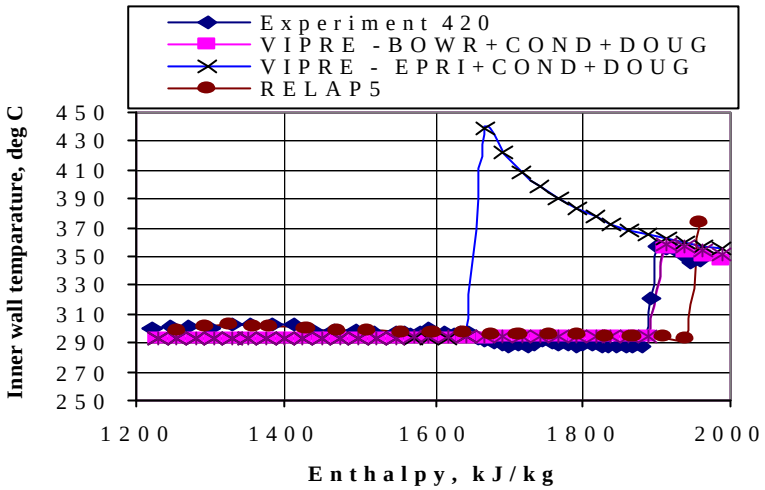

Figure 22. VIPRE-02 and RELAP 5/MOD3.3 calculation results for P=7 MPa. Mass flux 2000 kg/m²s. Here EPRI-EPRI CHF correlation; BJOR - Bjornard-Griffith; COND – Condie-Bengston; DOUG – Dougall-Rohsenow correlations.

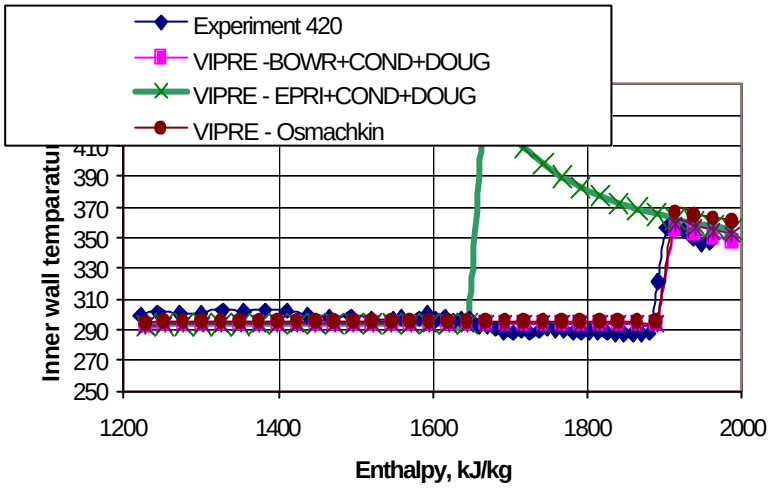

Figure 23. VIPRE-02 calculation results. Flow rate 2500 kg/m²s. Here BOWR – Bowring CHF correlation; EPRI-EPRI CHF correlation; COND – Condie-Bengston transition boiling correlation; DOUG – Dougall-Rohsenow film boiling correlation, Osmachkin - Osmachkin correlation.

For the medium pressures (7-12 MPa), the EPRI correlation provides an early prediction of the CHF occurrence in the single-channel models. The Bowring correlation and Osmachkin (as well as RRC KI) correlation provide good agreement with the experimental data for this pressure range (examples of the calculations are given in Figure 22 and Figure 23).

3.7.1.3. Low pressure experiments (2-3 MPa)

At lower pressures (see example of calculations in Figure 24) VIPRE-02 predictions using Bowring CHF correlation came closest with the experimental CHF measurements.

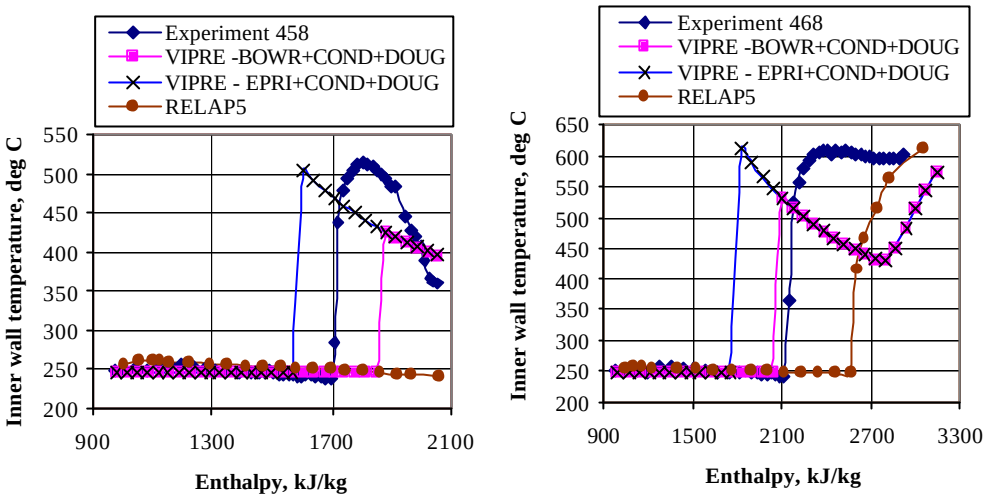

Figure 24. VIPRE-02 and RELAP5/MOD3.3 calculation results. Mass fluxes 2000 kg/m^{2}s (left) and 1000 kg/m^{2}s (right).

However, the close agreement with the experimental data can be obtained only in the range of coolant mass flux between 1000-2000 kg/m²s. Outside this range the CHF predictions by Bowring correlation are in large disagreement with the KTH experimental data.

3.7.2. Single channel model: E-108 experiments

During the EREC E-108 facility experiments, maximum wall temperature was recorded. Experimental data at two pressures are available: 2 and 7 MPa. During E-108 experiments, the test section power was kept constant and the coolant flow rate was gradually reduced from about 0.2 kg/sec until the occurrence of flow instabilities. Therefore the data analysis allows estimating the time and corresponding mass flow rates for occurrence of the CHF and the maximum wall temperature.

3.7.2.1. EREC E-108 experiments at 7 MPa

Figures 25-28 present examples of VIPRE-02 calculations for p=7 MPa. The coolant at the test section inlet was subcooled by about 100 ºC during the tests, presented in the Figures.

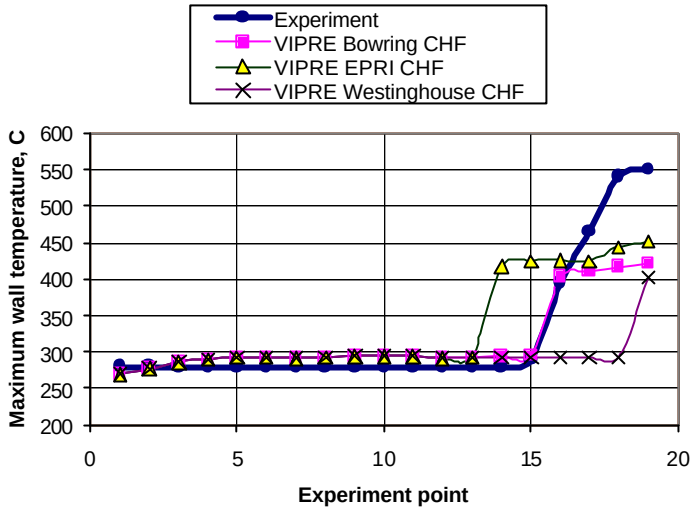

Figure 25. E-108 test calculations at P=7 MPa. CHF occurrence.

Several VIPRE-02 CHF correlations were applied at the pressure of 7 MPa. Figure 25 presents VIPRE-02 calculation results with three correlations: Bowring CHF correlation estimates CHF occurrence in E-108 test very well. EPRI correlation predicts the CHF at higher coolant flow rates and Westinghouse W-3 correlation underestimates the CHF. Also, for the pressure of ~7 MPa, user-coded Osmachkin and RRC KI correlations provide very close agreement with the experimental results (see example in Figure 26).

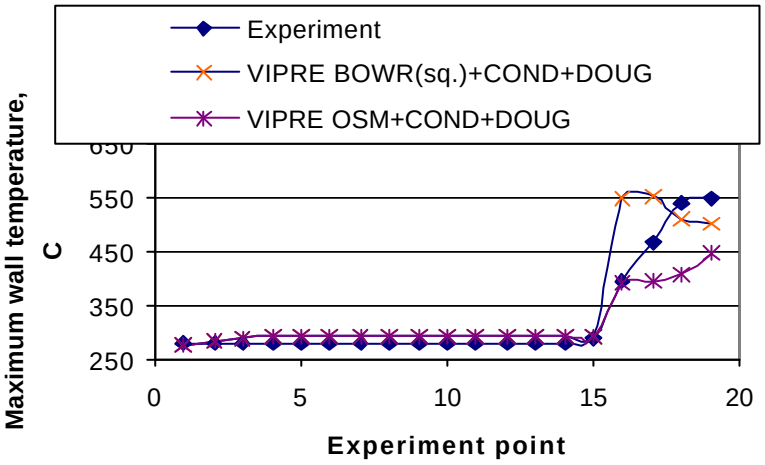

Figure 26. E-108 test calculations. Osmachkin correlation results.

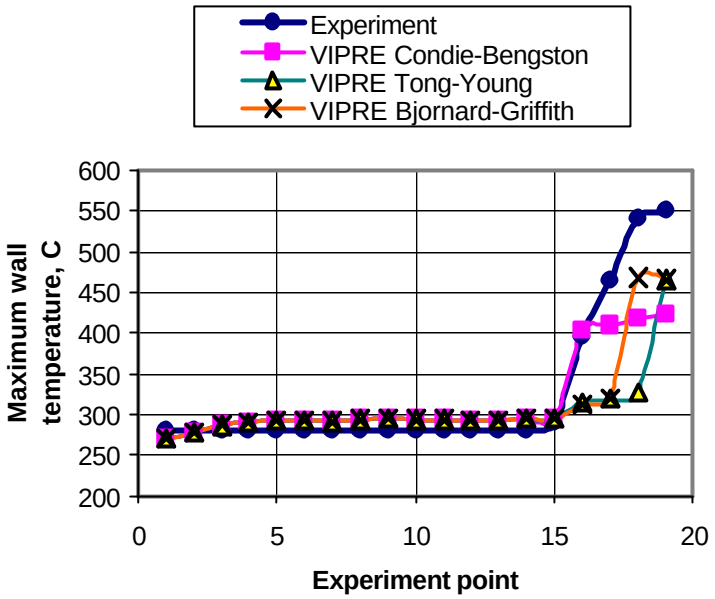

Figure 27. E-108 test calculations at P=7 MPa. Transition boiling.

For the transition boiling, Condie-Bengston correlation and Dougall–Rohsenow correlation for film boiling were used during the calculations, presented in the Figure 25. Although the CHF occurrence was predicted very accurately, post-CHF heat transfer calculation results do not agree with the experimental data. Post-CHF heat transfer correlations are investigated next.

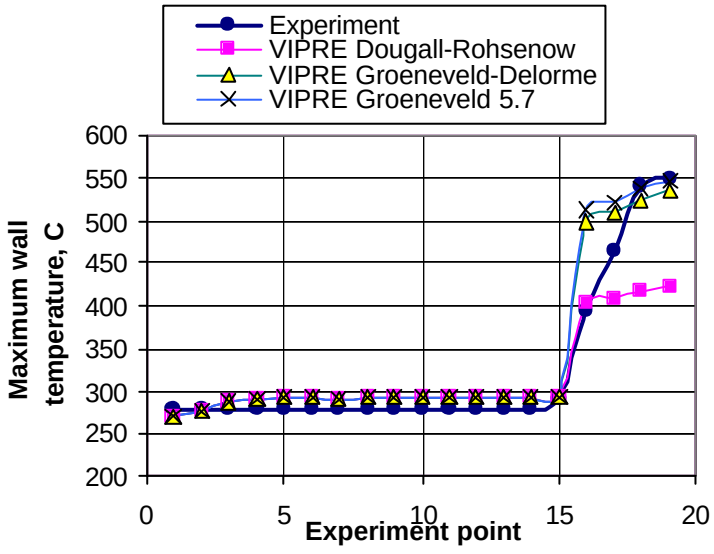

Figure 28. E-108 test calculations at P=7 MPa. Film boiling.

Example of the investigation of transition boiling mode is presented in the Figure 27. Three available correlations for transition boiling were applied: Condie-Bengston (default VIPRE-02 correlation), Tong-Young and Bjornard-Griffith. As seen from the

Figure 27, the closest agreement with the experiment data is obtained using the Condie–Bengston correlation for transition boiling.

For the film boiling model, three film boiling correlations of the standard VIPRE-02 code are available: Groeneveld 5.7 (default VIPRE-02 correlation), Groeneveld-Delorme and Dougall-Rohsenow correlations. The example of calculation results is presented in Figure 28. At the pressure of about 7 MPa, Groeneveld 5.7 film boiling correlation provides the closest agreement with the E-108 experiment data.

3.7.2.2. EREC E-108 experiments at 2 MPa

For the pressures of 2 MPa EPRI CHF correlation is recommended to be used with VIPRE-02. However, Bowring correlation also proved to provide rather good estimation, even though the recommended validity pressure range of this correlation is 3.4-15.9 MPa (EPRI, 1997).

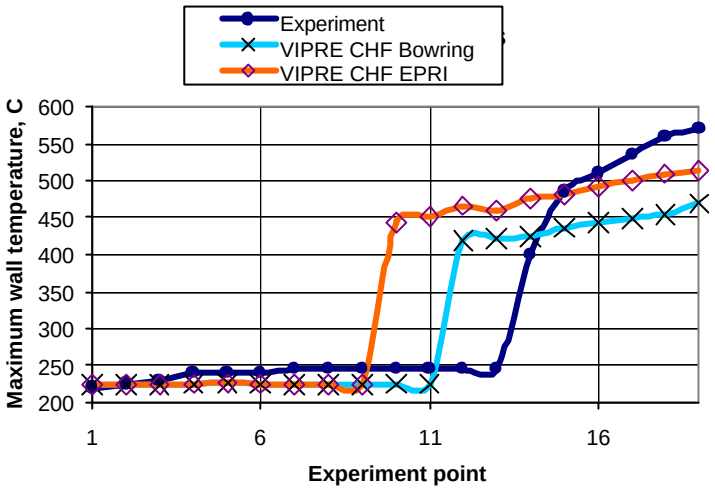

Figure 29. E-108 test calculations P=2MPa. CHF occurrence.

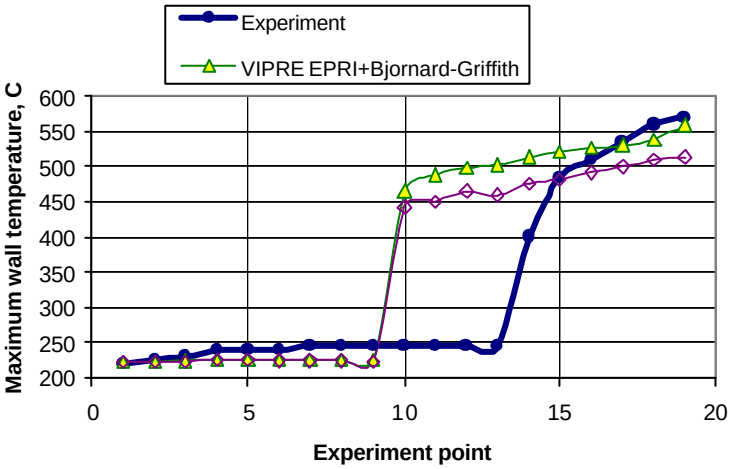

Figure 30. E-108 test calculations P=2MPa. Transition boiling.

Figure 29 presents an example of calculations performed for 2 MPa pressure. Initial flow rate through the test section was 0.2 kg/sec; the flow rate was gradually reduced until 0.054 kg/sec (experiment point 19). CHF occurrence was calculated to occur at much higher, compared to experimental, flow rates, with both EPRI and Bowring CHF correlations. However, Bowring correlation gave more exact estimation of the CHF (Figure 29) in this pressure range, which suggests that the use of Bowring correlation could be extended to lower pressures.

Comparison of calculation results with different transition boiling correlations is given in Figure 30. Condie-Bengston and Bjornard-Griffith correlations can be used, when the system pressure is about 2 MPa. Condie-Bengston is a default transition boiling correlation in VIPRE-02. The results for transition boiling, obtained with this correlation are close to the experimental results.

3.7.3. Summary of single channel model experiments

Over 100 cases of VIPRE-02 single-channel model calculations of KTH and EREC E-108 experiments were carried out. The available experimental data was in the pressure range from 2 to 20 MPa. VIPRE-02 correlations available with the standard code version for CHF, transition and film boiling were validated against the experimental data. In addition, user-coded Osmachkin and RRC KI CHF correlations were applied for the calculations at p=7 MPa.

Table 7. Summary of KTHand E-108 experiment calculations.

P, MPa	KTH experiments			E-108 experiments		
	CHF	Transition	Film boiling	CHF	Transition	Film boiling
2	-	-	-	Under-estimation	Bjornard-Griffith	-
3	Bowring (in limited ρw range)	Under-estimation	Over-estimation	-	-	-
7	Bowring, Osmachkin, RRC KI	All VIPRE-02 correlations	All VIPRE-02 correlations	Bowring, Osmachkin, RRC KI	Condie-Bengston	Groenevald-Delorme, Groenevald 5.7
12	EPRI	All VIPRE-02 correlations	All VIPRE-02 correlations	-	-	-
16	EPRI	Under-estimation	Groenevald-Delorme, Groenevald 5.7	-	-	-
20	EPRI	Under-estimation	Groenevald-Delorme, Groenevald 5.7	-	-	-

The results of the VIPRE-02 calculations are summarized in the Table 7. Here, the name of the correlation, which provides the best agreement with the experimental results for the given pressure, is provided. In case, when all available correlations

provide incorrect results, the main trend (underestimation or overestimation) is given. As it is seen from the Table 7, the best agreement with the experimental data was obtained for the medium pressure range (7-12 MPa). Good estimation of the CHF and the maximum wall temperatures during the film boiling was also obtained for the high pressure mode (P=16-20 MPa), exception at this pressure range being the transition boiling region, where all VIPRE-02 transition boiling correlations underestimate the maximum wall temperatures.

User-coded Osmachkin and RRC KI correlations provided good agreement with the KTH and EREC E-108 experimental CHF data for the pressure of p=7 MPa.

3.7.4. Subchannel model: KS experiments at RRC KI

A series of experiments on the RBMK rod bundles, carried out at the Russian Research Center Kurchatov Institute (RRC KI) during the years 1967-1990 were modeled with VIPRE-02. During the first test series (in 1967-1980) CHF and heat transfer measurements were performed for the RBMK-1000 reactor assemblies and the nominal RBMK parameters. During the later test series, various types of flow intensifiers for the RBMK-1500 upper fuel assemblies were tested.

The experimental results were used for the validation of the VIPRE-02 code for RBMK-1500 applications. The fuel channel in the VIPRE-02 model was divided into 30 square and rectangular sub-channels, which allowed lateral flows between various parts of the fuel assembly.

3.7.4.1. VIPRE-02 model of RBMK fuel channel

In order to facilitate the sub-channel analysis, the experimental RBMK fuel channel was modeled as a set of 30 triangular and square sub-channels with lateral connections (Figure 31). Flow intensifiers and fuel rod spacer grids were modeled at their axial locations in the RBMK-1500 fuel assemblies.

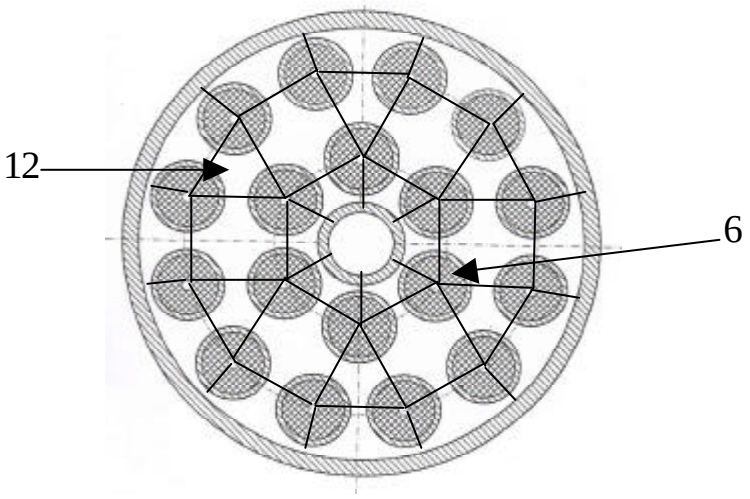

Figure 31. Cross section of the RBMK-1500 fuel channel model with VIPRE-02.

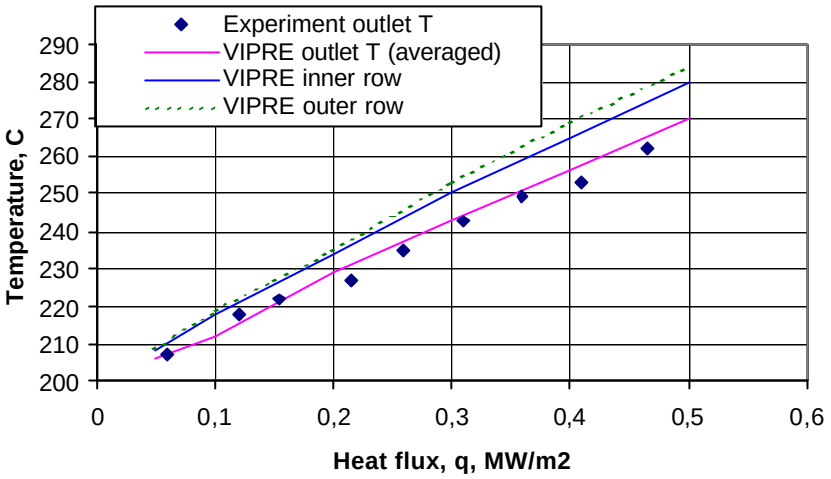

Figure 32. Distribution of the temperatures at the outlet of the fuel channel. Fuel assembly with additional flow intensifiers.

As it is seen from the Figure 32, the sub-channel model allows predicting the non-uniformities of the fuel rod wall temperatures at various locations of the channel. In the given case, the temperature difference between the rods in the 1st and 2nd ring of the fuel rods is ~6 °C, which corresponds rather well with the measurements, carried out during the experiments at RRC KI (as noted in the RRC KI experiments, the temperature difference between various rods in the assemblies with no additional flow intensifiers reaches up to 19°C; presence of the flow intensifiers reduces the temperature difference down to about 8°C).

3.7.4.2. RRC KI (KS) experiment calculations

Occurrences of the CHF on both lower and upper fuel assemblies were investigated. The system pressure ranged from 6.87 to 9.41 MPa and the coolant inlet temperature varied from 230 to 265°C.

The VIPRE-02 calculations had shown, that RRC KI correlation for the upper RBMK-1500 fuel assembly provides a good prediction for the CHF occurrence. Khabenski correlation for the low mass flux region also provides a good agreement with the experimental results. Bowring correlation, included in the standard VIPRE-02 version, gives a slight underestimation of the CHF.

For the lower fuel assembly of the RBMK-1500, EPRI CHF correlation, also included in the standard VIPRE-02 code, provides good predictions of the experimental results (for fuel assemblies with no additional flow intensifiers) at the pressures of about 7 MPa. For the single channel models the same correlation predicts the CHF occurrence at significantly lower power levels. However, at the sub-channel level the EPRI correlation proves to be a reliable tool to evaluate CHF in the lower assemblies of RBMK-1500 fuel channels.

Bowring correlation provides close predictions for the CHF occurrence on the upper fuel assemblies in the RBMK-1500 fuel channels (Figure 33).

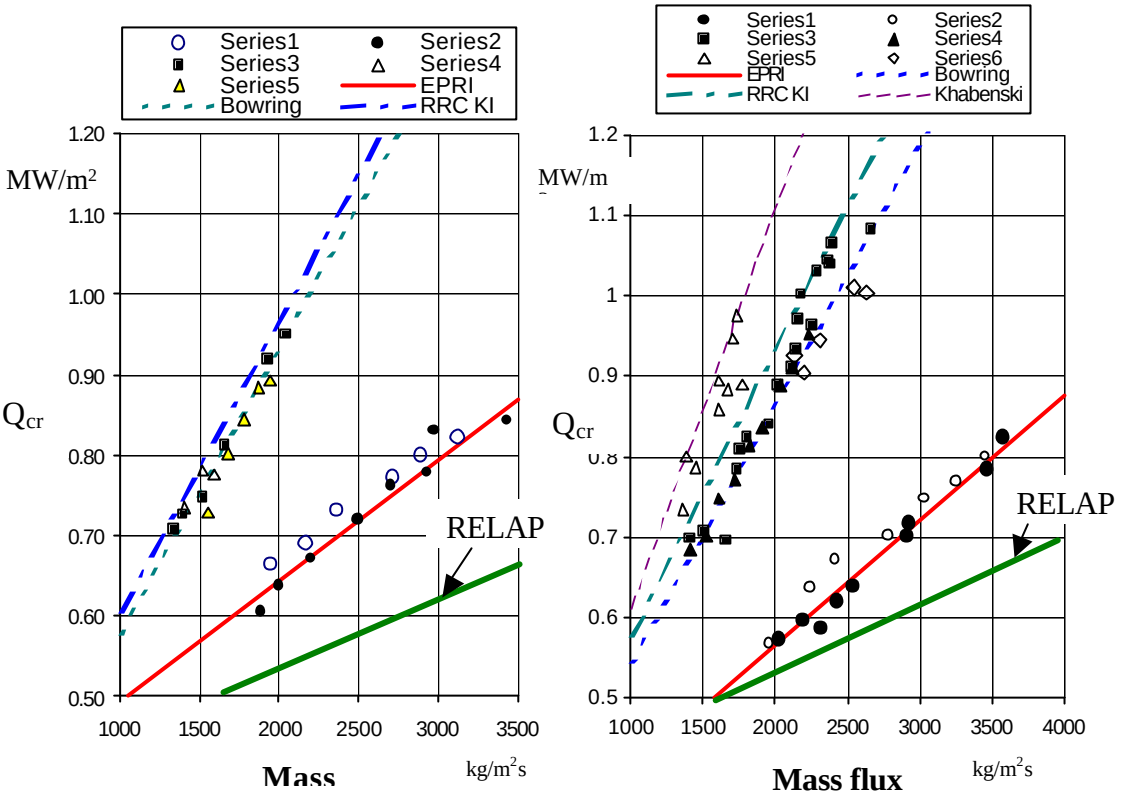

Figure 33. CHF occurrence in the RBMK-1500 rod bundle at various inlet subcooling (t_{in}= 230-240°C on the left and t_{in}=260-264°C on the right). Series 1 and 2: lower RBMK-1500 fuel assemblies; Series 3-6 upper RBMK-1500 fuel assemblies with flow intensifiers.

RRC KI correlation, on the other hand, predicts the CHF occurrence at lower flow rates but the predictions are very close to the data, measured during the experiments. Khabenski correlation provides a close agreement with the experimental data for the CHF occurrence in the low coolant mass flux region. For higher coolant mass fluxes (≥2000 kg/m^{2}s) the Khabenski correlation starts to overpredict the CHF.

Surprisingly, the Osmachkin correlation, which had provided a good agreement in the single channel model calculations (see Chapter 3.7.3), strongly overpredicts the CHF in the sub-channel model. This may be a result of the fact, that the Osmachkin correlation was developed as a 'global' correlation for average channel operational conditions rather than the 'local' type of correlation, which is needed for predictive sub-channel code calculations.

As it is seen from the Figure 33, RELAP5/MOD3.3 code standard CHF correlation, based on look-up table, underpredicts the occurrence of CHF in the rod bundles under all investigated flow conditions.

3.8. Major findings and accomplishments

Series of experiments, carried out at KTH, EREC E-108 and RRC KI test facilities were analyzed with the VIPRE-02 code. The aim of the work was to validate the CHF and post-CHF correlations, implemented in VIPRE-02 code against the experimental data for heat transfer in 7 m long channels. The VIPRE-02 simulation results were benchmarked against the CHF predictions with the RELAP5/MOD3.3 code (standard tabular CHF correlation). Three additional CHF correlations, developed for the RBMK type reactors were implemented in the VIPRE-02 code.

A series of KTH experiments were modeled with the test section pressures ranging from 3 to 20 MPa. For high pressures (16-20 MPa) close agreement with the experimental data was obtained using EPRI CHF correlation. Both CHF occurrence and film boiling processes were predicted well. RELAP5/MOD3.3 code calculations also provided good predictions for CHF occurrence at 16 MPa pressure. The maximum wall temperatures were underestimated with all VIPRE-02 transition boiling correlations for this pressure range.

For the intermediate pressure range (7-12 MPa) there was good agreement between the VIPRE-02 calculations and the experimental data. Bowring CHF correlation provides correct estimate for CHF occurrence in this pressure range. For lower flow rates Bowring CHF correlation predicts CHF at higher enthalpies, compared to the experiments. EPRI correlation provides lower enthalpy values for the CHF occurrence at p=7 MPa. Transition and film boiling could be predicted well with all VIPRE-02 correlations over the intermediate pressure range. RELAP5/MOD3.3 code calculations for a single channel model result in an overprediction for the CHF occurrence (CHF is calculated to occur at higher enthalpies).

Good CHF prediction for the p=7.0 MPa in a single channel case was obtained with used-coded Osmackhin and RRC KI correlations.

For lower pressure (~3 MPa) CHF was predicted correctly employing Bowring CHF correlation. But the correlation is valid only when the coolant mass fluxes are between 1000-2000 kg/m²s. For higher mass fluxes the Bowring CHF correlation provides underestimation of CHF and at lower mass fluxes the correlation overestimates CHF. For this pressure range, RELAP5/MOD3.3 code also provides an overpredicted value for the CHF.

The sub-channel VIPRE-02 model of the RBMK-1500 was created in order to assess the sub-channel analysis capabilities of the VIPRE-02 code.

EPRI CHF correlation was in a good agreement with the CHF experimental data for the subchannel fuel bundle model (RRC KI experiments) even though it provided erroneous results for single channel experiments at p=7.0 MPa. This correlation can be recommended when performing RBMK-1000 sub-channel analysis and also when performing CHF evaluation for the lower assemblies of RBMK-1500 fuel channels.

On the other hand, the Osmachkin correlation, which provided close CHF predictions for single channel models, strongly overpredicts the CHF occurrence in the sub-channel model. This indicates that the correlation was derived as 'global' for the average RBMK-1500 channel parameters rather than for the 'local' parameter based CHF prediction.

For upper fuel assemblies of the RBMK-1500 RRC KI correlation provides a good prediction for the critical heat flux. The accuracy of the correlation decreases with increasing liquid subcooling at the entrance of the fuel channel. It can be recommended to employ the RRC KI CHF correlation for estimating the upper assembly CHF values with VIPRE-02 code.

Bowring CHF correlation, implemented in the standard VIPRE-02 version, also provides a close agreement with the experimental results of the CHF for upper assemblies of RBMK-1500.

Sensitivity analysis of the used CHF correlations shows, that there is no significant dependence of CHF on the system inlet pressure. This holds for all investigated CHF correlations. On the other hand, inlet coolant subcooling has a significant influence on the CHF values. For highly subcooled liquid at the entrance, Bowring correlation is recommended for the upper RBMK-1500 assembly CHF predictions.

The standard CHF correlation, implemented in the RELAP5/MOD3.3 code underpredicts the CHF occurrence for all calculated cases for the RRC KI experiments, although the RELAP5/MOD3.3 provides close CHF estimations for the single channel models (KTH experiments).

Chapter 4

Ignalina NPP RBMK-1500 Reactor Core Performance and Safety Analysis

4.1. Objectives

The aim of the work was to develop, verify and validate a fully independent RBMK-1500 reactor core analysis methodology, based on independent codes. The methodology should allow performance of a full spectrum of the RBMK-1500 rector core dynamics and safety analysis and should incorporate an adequate thermal hydraulic module.

The CORETRAN code, developed at EPRI was used as the reactor kinetic code. The neutron cross section data were calculated using HELIOS code (see Chapter 2) and the thermal hydraulic module VIPRE-02 was supplemented with additional CHF correlations, applicable for RBMK-1500 type reactors (see Chapter 3).

The CORETRAN calculations were verified against the Ignalina NPP RBMK-1500 reactor data: steady state and experimental values.

The CORETRAN code is applied for the RIA and ATWS calculations. The core neutron kinetics calculation results were supplemented with additional detailed thermal hydraulic analysis.

4.2. Introduction and background

The RBMK reactors are channel type, water-cooled and graphite-moderated reactors. The first RBMK type electricity production reactor was put on-line in 1973. Currently there are 13 operating reactors of this type. Two of the RBMK-1500 reactors are at the Ignalina NPP in Lithuania.

The core of RBMK-1500 reactor is a large graphite stack (11.8 m in diameter and 7 m high). The stack is penetrated with 2052 channels. Most of these channels (the total number is 1661) contain fuel assemblies. The fuel assembly consists of two parts: upper and lower, which are placed one above another in the reactor fuel channel. There are 18 fuel rods in each fuel assembly. Besides the fuel channels there is a certain number of so-called 'special purpose channels' in the core. These channels contain control rods, various detectors, etc. (Almenas et al, 1998). The reactor fuel is

slightly enriched uranium oxide (initially 2.0%, currently of 2.4% and 2.6% enrichment and planned 2.8% enrichment in U^{235}, containing Erbium). The fuel enrichment was increased from the initial 2% level due to the safety reasons after the Chernobyl accident.

Four operating RBMK plants are considered as the first-generation units (Leningrad-1 and 2, Kursk-1 and 2). They were designed and brought on-line in the early and mid- 1970's, before the new standards on design and construction of the nuclear power plants (OPB-82) were introduced in the former Soviet Union. Units brought on-line since late 1970's and early 1980's are grouped as the second generation RBMK's (Ignalina-1 and 2, Leningrad-3 and 4, Kursk-3 and 4, Smolensk-1 and 2). These units were designed and constructed according the updated standards of 1982. After the Chernobyl accident, the Soviet standards were revised once again (OPB-88) and the third generation units: Kursk-5 and Smolensk-3 were built.

During the whole time of their operation, the RBMK power plants have been the cheapest nuclear energy producers in the former USSR (and now in Russia), with the highest capacity factors (Adamov, et al, 1997). This is due to the unique features of this reactor type, such as the capability for the on-line refueling.

However, there are several disadvantages for the RBMK reactors: the large size of the core makes it difficult to control (there are 211 control rods in the RBMK-1500 power plant). The most serious drawback of the RBMK reactor types is the positive void reactivity coefficient.

Therefore, immediately after the Chernobyl accident in 1986 the safety enhancement programs were initiated at all RBMK plants. Among the safety measures implemented was the improvement of the operational reactivity margin (from 30 to 45 MCR's), installation of additional absorbers in the core in order to inhibit the operation at low power, increase of the scram rod insertion speed, re-design of the control rods, etc.

RBMK reactor power is controlled by the Control and Protection System (CPS). The system consists of two sub-systems: the standard reactor control system and Fast Acting Scram System (FASS). The CPS is cooled by an independent water circuit. There are 3 types of control rods: Manual Control Rods (MCR), Shortened Control Rods (SCR) and Fast Acting Scram Rods (FASR). The MCRs and FASRs are inserted from the top of the core while the SCRs (which are employed to control axial power distribution along the height of the core) are inserted from the bottom. The absorber used in the control rods is B_4C and Dy_2TiO_5.

The core of the RBMK-1500 reactor is divided into 12 Local Automatic Control (LAC) and Local Emergency Protection (LEP) sectors (Almenas et al, 1998). The twelve LEP sectors overlap and fully cover the entire core. In each local zone, there are one automatic regulator (LAR) and two Emergency Shutdown Rods (LAZ) rods. About 350 groups of detectors are in the reactor. Each group comprises of the 2 to 7 detectors. Besides these detector groups, there are 3 groups of the out-of-core detectors, which monitor total reactor power. These detectors generate full reactor

scram signal when the total change of the reactor power exceeds ~10 %. The signals from the sensors in the sectors are processed by the Power Density Distribution Monitoring System (PDDMS). This system generates the signals that are used by the CPS to control the reactor power. PDDMS collects data from flux sensors, distributed discretely in the core. The completely processed information shows the radial and axial power distribution in the reactor, deviation from the power setpoints and other relevant reactor information.

The modification and safety improvement of the RBMK type reactors is still an on-going process. In order to improve the plant economic features (i.e. to increase the fuel burnup) without compromising the plant safety, higher enrichment fuel is being introduced. The initial fuel of 2% enrichment was changed to 2.4% enrichment fuel (with additional Erbium as a burnable poison), which allowed reducing the number of additional absorber rods in the RBMK cores. Now the 2.6% enrichment fuel is being introduced at the Ignalina NPP with future plans to utilize 2.8% enrichment fuel. The continuous changes in the core configuration require also the development of core analysis capabilities in order to assess the safety of new reactor states. Therefore, the development and adoption of western codes for RBMK core neutronics and thermal hydraulic analysis remains an important issue.

4.3. RBMK type reactor safety analysis

The primary objective of the nuclear safety is to protect individuals, society and environment by establishing and maintaining an effective defense against the radiological hazards in the nuclear power plants.

In the RBMK plant safety analysis a proper set of the plant initial conditions has to be defined. The conditions can be sub-divided into three different categories: neutronic characteristics, thermal hydraulic characteristics and characteristics of systems, components, etc. The conditions have to be defined in such a way, that the values, selected for the initial conditions should be those that result in the most conservative (least favorable) sequence with respect to the accident scenario and the acceptance criteria being evaluated. For the state process variables, these should be normally selected at the edge of their operating spectrum. The protection and safety function availability should also be determined by the application of a single failure criterion. The single failure criterion requires that the reactor safety system is able to perform its required functions even if a single failure within the system of its component, required to mitigate the consequences of the event, occurs.

In the case of transient and accident analysis, in which space–dependent neutronic and thermal hydraulic phenomena are important, three-dimensional codes with thermal hydraulic feedbacks should be used to describe adequately and model the RBMK core structure, absence of symmetry, spatial dependence of the feedback effects, etc. Also, the core monitoring and control system (detectors, automatic control rods, etc.) should be represented in the codes to properly account for the specific control features. All models and correlations should be within the range of their validity. Each code has to be verified, validated and qualified prior to the application to the accident analysis.

The earlier RBMK reactor transient and accident analysis codes are of the Russian origin. Recently, also Western thermal hydraulic codes (e.g. RELAP5, ATHLET, CATHARE) and neutron kinetics codes (QUABBOX/CUBBOX, CORETRAN, RELAP-3D) are being used.

Two integral reactor physics codes, developed in Russia are used for RBMK-1500 core analysis. The STEPAN/KOBRA code was developed at RRC KI starting in 1985. It is used for steady state and transient analysis. The neutronic part of the STEPAN is a full-scale 3-D code. It uses two energy group diffusion approximations and solves the equations by the finite difference or nodal methods. The two-group neutron cross-section library is generated by the WIMS-D4 code. The thermal hydraulic part of the code, KOBRA describes all 1661 fuel channels of the core, as well as other reactor MCC components, such as drum separators, downcomers, pumps and headers. Feed water flow and ECCS injection are describes as boundary conditions. The code neutronic and thermal hydraulics parts were validated and verified separately. The STEPAN code neutronics were validated against the RRC KI Critical Facility data and RBMK plant data. The code was verified by the benchmark calculations with MCNP, ARROTTA (now CORETRAN) and SADCO. The thermal hydraulic part of the code, KOBRA was verified by the benchmark calculations (e.g. Edward's pipe) and comparison with RELAP5.

The SADCO (Safety Analysis and Design Code) code was developed at RDIPE during the 90's and was intended for mainly coupled steady state neutronic and thermal hydraulic calculations of RBMK-1000 and RBMK-1500 reactors. The code models reactor kinetics in addition to the reactivity feedbacks due to a change in coolant void, fuel and graphite temperatures. SADCO models only the reactor core with fixed boundary conditions at the Group Distribution Headers and Drum Separators. The rest of the MCC can be simulated using MOUNT1 code (IAEA, 2001).

The combinations of both the STEPAN/WIMS-D4 and the SADCO/WIMS-D4 codes in general are not capable to predict accurately the measured radial power distribution in the INPP. Modifications are made in the cross section data to obtain better fits to the measured power distributions. In the STEPAN code the thermal cross sections for some assemblies are changed while the SADCO code changes the fuel assembly burnups, which change the cross section data for both groups, and also the axial positions of control rods. The correction procedures employed by these two codes are not documented and lack transparency.

The Western codes, originally developed for vessel type LWR calculations are also used for the RBMK investigations since 1989. The core 3-D neutronics codes, such as QUABBOX/CUBBOX, CORETRAN and RELAP-3D are being applied. The codes are well validated for the Western PWR's and BWR's and were adopted for RBMK conditions by the appropriate input modeling. Some specific RBMK features were developed additionally (Clemente, 2000, Knoglinger et al, 1996, Bubelis, 2001).

The main domain of the 3-D neutron kinetic code applications for the RBMK type reactors is the RIA and ATWS calculations. According to the initiating event, there are several Reactivity Initiated Accidents (RIA) to be considered, such as the continuous single rod and rod bank withdrawal from the core, control rod drop into the core and control rod drop-out of the core, refueling error (or incorrect fuel placement) and loss of coolant in the control rod channel cooling system (CPS LOCA).

4.4. RBMK-1500 core transient and accident analysis methodology

The key safety functions for RBMK-1500 are stated in the Lithuanian safety regulations VD-T-001-0-97 (VATESI, 1997) and correspond to the IAEA recommendations (IAEA, 1989).

According the methodology, adopted for RBMK-1500 analysis in Lithuania (INPP SAR, 2001), the detailed accident and transient analysis is performed having defined (postulated) the groups of initiating events. All initiating events were grouped according the reactor initial state into:

- Accidents during reactor startup;
- Accidents at reactor normal operation;
- Accidents during reactor shutdown;
- Accidents at shutdown reactor,
- Other accidents.

Anticipated transients without scram (ATWS) are grouped separately to cover a number of initiating failures together with the complete loss of emergency shutdown function. For RBMK type plants these failures are beyond design basis.

According to the frequency of occurrence the initiating events are classified into DBA, beyond DBA and severe accidents. All the DBA are divided into two groups:

- Anticipated transients;
- Postulated transients.

Anticipated transients are defined as events within the safe reactor operation limits, which are expected to occur at least once in the design lifetime of the plant (this may include, e.g. specific equipment failures or malfunctions). Postulated accidents are not expected to occur during the design lifetime of the plant, their probability of occurrence is usually less than 10^{-2} per reactor year. The postulated accident group includes all accidents with loss of coolant, breaks of feedwater and steam lines.

The transients of the interest for the 3-D neutron kinetic code analysis for the RBMK-1500 can be grouped as:

<u>Anticipated transients:</u>

- Reactivity and power changes in the core:
    - Single rod drop in the center of the core;
    - Single rod drop in the periphery of the core;
    - Drop out of the shortened absorber rod from the core;
    - Voiding of a RCPS circuit cooling;

- Erroneous reloading of fuel assembly.

Postulated accidents:

- Reactivity and power changes in the core:
  - Drop of a group of control rods in core center;
  - Drop of group of control rods in core periphery;

Anticipated transients without scram:

- Maximum reactivity insertion by central or peripheral control rod withdrawal from the core;

Separate sets of acceptance criteria (LEI, 2001) were defined for anticipated transients, postulated transients and anticipated transients without scram. The acceptance criteria take into account fuel pellet, cladding, pressure tube, MCC, reactor cavity, ALS integrity, etc. The accident analysis methodology (LEI, 2001) also defines the definition of the accident sequence, operator actions, modeling assumptions and parameters, etc.

4.5. KTH methodology

An independent 3-D neutron kinetic calculation methodology was developed at the Division of Nuclear Power Safety at Royal Institute of Technology (KTH). The methodology employs Western computer codes (CORETRAN, HELIOS, VIPRE-02) for the RBMK-1500 reactor calculations. The two group neutron cross sections are calculated using the HELIOS code (see Chapter 2), where exact geometry of the various assemblies is employed. The core neutron dynamics calculations are performed using the CORETRAN code, which employs neutron cross sections generated with HELIOS code. No corrections are made to the two group cross sections generated with the HELIOS code.

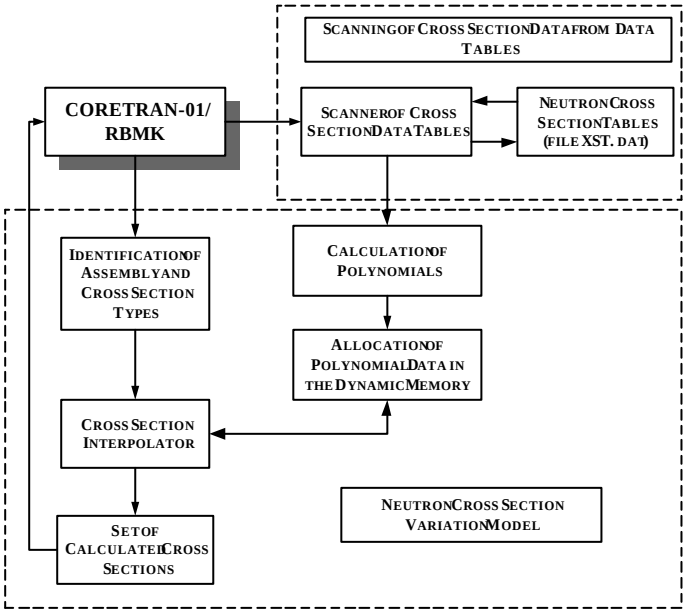

Figure 34. KTH cross section variation model for RBMK assemblies.

The neutron cross-section variation model for the RBMK-1500 applications is based on the logic shown in the Figure 34. The CORETRAN code reads a file with HELIOS code calculated 2-group neutron cross section data, recorded in the form of tables and performs computation of 2-D polynomial coefficients. The coefficients are allocated in the dynamic computer memory during the CORETRAN calculations and are accessed directly each time when a recalculation of each cross section is performed.

The polynomial coefficients define 2-D functions for each cross section of each assembly type. These 2-D functions are used to calculate basic components in the cross section variation model. The basic components are calculated by running an interpolation procedure, which performs interpolation by using polynomial coefficients. The cross section value for the fuel assemblies is calculated as:

$$\Sigma\,(B,D_C,T_F,T_G,) = \Sigma_F(B,D_C,) + \Delta\Sigma(B,T_F,) + \Delta\Sigma(B,T_G,) \qquad (35)$$

Here the neutron cross section $S(B,D_C,T_F,T_G,)$ is a function of fuel burnup B, coolant density D_C, fuel temperature T_F and graphite temperature T_G. The value of the cross section $S(B,D_C,)$ or first basic component, is calculated by interpolating the polynomials that define cross section dependence on fuel burn up B and on coolant density D_C (a 2-D table where variables are B and D_C). The other two terms in Eq. (35) represent differential values added into the 2-D polynomial tables to account for the correction of cross sections due to variations of fuel and graphite temperatures versus fuel burnup. The three terms (basic components) in Eq.(35) are assumed to be independent.

Cross sections for non-fuel assemblies are calculated by employing Eq.(36) where $\Sigma_{NF}(D_{CCPS},D_{CMCC},T_G)$ is cross section of non fuel assembly as a function of coolant presence in the CPS channel D_{CCPS}, average coolant density in the surrounding fuel channels D_{CMCC}, and graphite temperature T_G of surrounding graphite blocks.

$$\Sigma_{NF}(D_{CCPS},D_{CMCC},T_G,)= \Sigma(B,D_C,)_{DCCPS} \qquad (36)$$

In order to calculate cross sections for non-fuel assemblies, two sets of cross section tables are utilized. The first set of data accounts for cross sections calculated by considering conditions, when CPS system cooling water is present and the second set of data is generated by assuming that the CPS channels are empty (without coolant).

For fuel cell calculations, two sets of cross sections were generated for each fuel assembly type. This is due to the reason that the upper and lower assemblies in the reactor core are not identical in the RBMK-1500 reactor. There is additional steel present in the upper assemblies. The steel is in the form of additional flow intensifiers, which increase two-phase flow mixing in the upper part of the core.

Table 8 presents a complete set of cross sections or parameters, which are obtained employing HELIOS calculations for the CORETRAN code input. For fuel assemblies the total number of parameters is 29 and for non-fuel assemblies 7 parameters are required.

Table 8. Cross sections used in the CORETRAN calculations (F-fuel, NF - non-fuel assemblies).

	Cross section or constant	Assembly Type
1.	Diffusion Constant; G1	F & NF
2.	Diffusion Constant; G2	F & NF
3.	Scattering Cross Section (CS);	F & NF
4.	Absorption CS; G1	F & NF
5.	Absorption CS; G2 (Without Xe)	F & NF
6.	ν·Fission CS; G1	F
7.	ν·Fission CS; G2	F
8.	Energy per fission (Ws/fission); G1	F
9.	Energy per fission (Ws/fission); G2	F
10	Effective number of neutrons per	F
11	Effective number of neutrons per	F
12	Inverse neutron velocity; G1	F & NF
13	Inverse neutron velocity; G2	F & NF
14	Delayed neutron yield; DNG 1	F
15	Delayed neutron yield; DNG 2	F
16	Delayed neutron yield; DNG 3	F
17	Delayed neutron yield; DNG 4	F
18	Delayed neutron yield; DNG 5	F
19	Delayed neutron yield; DNG 6	F
20	Decay constant; DNG 1	F
21	Decay constant; DNG 2	F
22	Decay constant; DNG 3	F
23	Decay constant; DNG 4	F
24	Decay constant; DNG 5	F
25	Decay constant; DNG 6	F
26	Microscopic absorption CS of Xe^{135};	F
27	Microscopic absorption CS of	F
28	Effective yield of Xe^{135} per fission	F
29	Effective yield of I^{135} per fission	F

4.5.1 Additional development of CORETRAN code

In order to facilitate the CORETRAN calculations, a number of additional features were added to the code. Among the modifications was an increase in the number of fuel channels calculated by CORETRAN (56×56 map for the RBMK case). In addition to this, a number of additional subroutines were added to the code (Knoglinger, et. al., 1996), which facilitate:

- The reactivity calculation using the inverse point kinetics model (the same type of the reactivity calculations is used when calculating the reactivity using the actual reactor detector data at the Ignalina NPP);
- The operation of the control logics of the CPS system (LAR-LEP system; locations of detectors, grouping of detectors, signal sequences, set points, etc. are defined in this subroutine);
- Adoption of RBMK-1500 neutron cross section library (e.g. HELIOS) for the CORETRAN code calculations and the interface between the cross section library and the 3-D neutronic code;

- Increased number of control rods in the core (the standard CORETRAN version allows only 199 control rods, whereas in the RBMK-1500 reactor there are 211 control rods); etc.;

4.6. CORETRAN calculation results for RBMK-1500 rector

The CORETRAN version, adopted for the RBMK-1500 calculations had to be tested and verified against the plant data in order to assess the functionality of the new RBMK-1500 core model. Some recent aspects of the CORETRAN code validation and analysis, performed at KTH, are presented within the scope of this Thesis.

4.6.1. Cold zero power calculations

Some of the measurements of the RBMK-1500 reactor safety parameters are performed during the reactor maintenance period, at the cold reactor conditions. One of the most important measurements in this phase is the reactor subcriticality at the cold conditions, after the Xenon transient (i.e. about 120 hours after the reactor shutdown). These measurements are performed on all RBMK type reactors at least once a year. The control rod efficiency is also measured during these tests.

The example of the Xenon transient calculations with CORETRAN code using both HELIOS and WIMS-D4 code generated cross section data is presented here. The results of the calculations are compared to the actual plant data (Voroncov, 2002).

The transient conditions were modeled according to the Report (Voroncov, 2002): the reactor core state of 15 February 2001 was used as the initial state. The reactor was shut down. After 72 hours the reactor subcriticality was evaluated. Then the reactor was shut down again and after 120 hours the second subcriticality measurement was made. The experimental data, as well as CORETRAN calculation results are presented in the Table 9.

Table 9. Ignalina NPP-2 reactor subcriticality measurements for cold reactor conditions.

	Time, hours	Experiment-al value	CORETRAN (HELIOS cross section data)	CORETRAN (WIMS-D4 cross section data)
FASS rod efficiency, β_{eff} Reactor subcriticality, β_{eff}	72	1.98 5.6	2.7 5.59	- 5.03
Reactor subcriticality, β_{eff}	120	6.0	5.54	4.99

Closer agreement with the measurements was obtained for CORETRAN calculations with HELIOS code generated neutron cross section data.

4.6.2. Hot reactor states

A series of validation calculations were carried out in order to assess the CORETRAN code calculation results for the hot reactor states (i.e. with parameters, similar to reactor operational conditions).

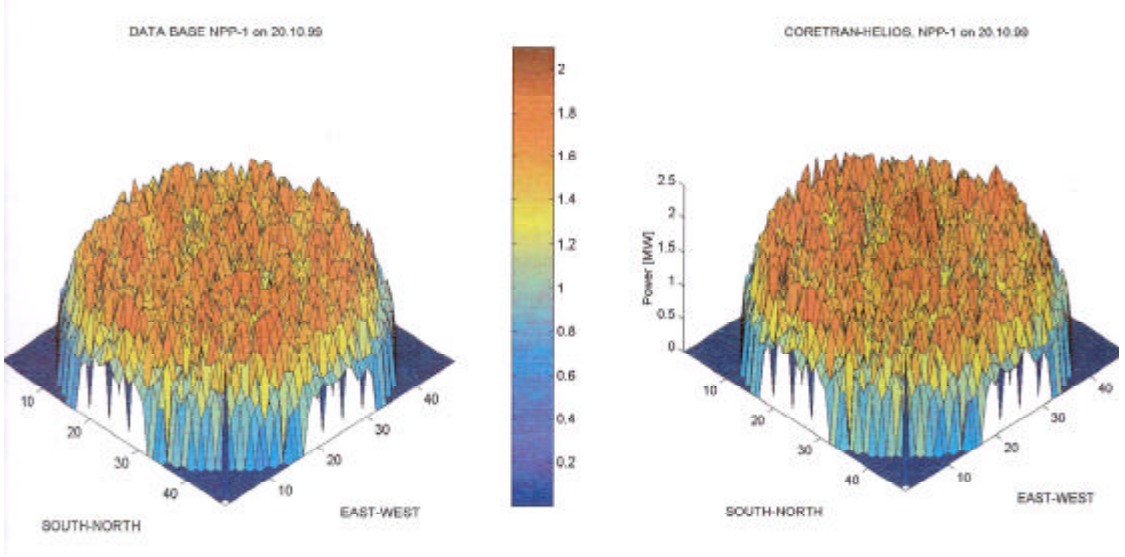

Figure 35. Radial power distribution in the INPP calculated with the CORETRAN code employing the HELIOS neutron cross-section library.

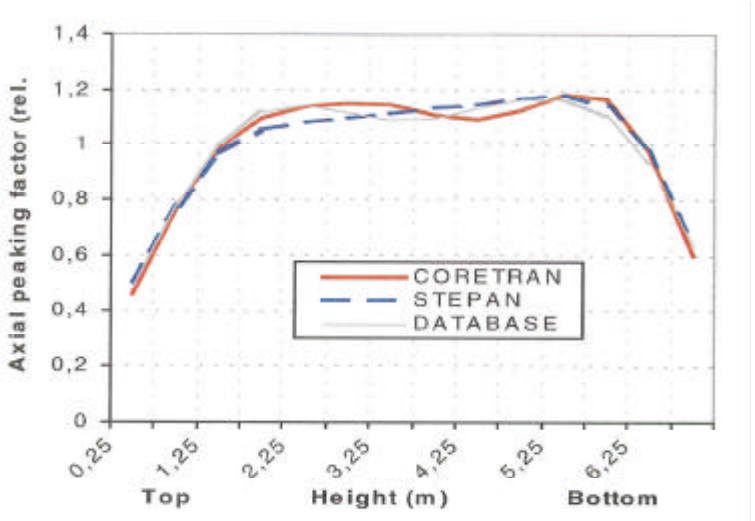

Figure 36. Averaged axial neutron flux distribution.

The results of the calculations were compared to the data, recorded in the Ignalina NPP reactor database (recorded data for the reactor state for each day is available, where the sensor readings allow calculating actual radial and axial power distribution in the operating reactor. This data allows testing the analysis method at operating reactor conditions). The example of comparison of the radial power distribution is presented in the Figure 35.

Table 10. Comparison of steady state calculation results (CORETRAN-HELIOS) with the Ignalina NPP database records (in brackets CORETRAN - WIMS-D4 calculations).

Database	K_{eff} – *eigenvalue*	K_r – *radial peaking factor*	Average deviation of radial neutron field from measured, (%)	K_z - *axial peaking factor*
NPP-1 on 05.05.98	0.9947 (1.001)	1.46 (1.58)	9.1 (10.5)	1.27 (1.15)
NPP-1 on 17.03.99	0.9993 (1.002)	1.46 (1.52)	7.2 (11.9)	1.29 (1.28)
NPP-1 on 20.10.99	0.9976 (1.002)	1.46 (1.47)	5.9 (7.3)	1.19 (1.19)
NPP-2 on 17.03.98	0.9913 (0.9958)	1.49 (1.51)	9.5 (11.6)	1.28 (1.28)
NPP-2 on 01.10.98	0.9924 (0.9968)	1.53 (1.51)	10.3 (12.0)	1.29 (1.23)
NPP-2 on 26.11.98	0.9923 (1.001)	1.52 (1.47)	8.6 (10.5)	1.21 (1.22)
NPP-2 on 29.03.99	0.9954 (0.9985)	1.87 (1.78)	16.0 (14.4)	1.24 (1.17)
NPP-2 on 21.12.99	0.9953 (0.9997)	1.79 (1.68)	15.5 (13.0)	1.18 (1.19)

Table 11. Comparison CORETRAN and STEPAN results for RBMK-1500 reactor

Unit, Data	*Code*	a_{j}, %	$a_{w}\cdot 10^{6}$, 1/MWt	$a_{t}\cdot 10^{5}$, 1/°C	$a_{c}\cdot 10^{5}$, 1/°C	Dr_{MCC},%	Dr_{CPS}, %
2-29.03.99	STEPAN	0.30	-2.30	-1.10	4.10	0.40	1.40
___"___	CORETRAN-WIMS	0.49	-1.40	-1.75	4.12	0.75	1.34
___"___	CORETRAN-HELIOS	0.52	-1.38	-	-	-	-
___"___	Experiment	0.54±0.12	-1.26±0.12	-	-	-	-
2-21.12.99	STEPAN	0.20	-2.50	-1.00	4.00	0.20	1.20
___"___	CORETRAN-WIMS	0.52	-1.32	-1.75	4.19	0.58	1.17
___"___	CORETRAN-HELIOS	0.34	-1.51	-1.76	3.60	0.25	0.76
___"___	Experiment	0.36±0.12	-1.56±0.12	-	-	-	

Figure 36 presents an example comparison of the average axial neutron flux distribution. Here the CORETRAN calculation results are also compared to the STEPAN code calculated values. CORETRAN code provides more realistic representation of the axial flux distribution (the double-humped shape of the curve). Table 10 provides the example comparison of the results of CORETRAN calculations carried out for various reactor states. Here, radial and axial peaking factors, as well as average deviations of the calculated results from the measured data are provided.

Also, during the operation of the Ignalina NPP, measurements of some important parameters, e.g. steam void coefficient, are performed at periodic intervals. A series of such calculations were performed at KTH, comparing results obtained with the

CORETRAN code against data from both reactors at the Ignalina NPP (INPP-1 and INPP-2).

Figure 36 presents an example comparison of the average axial neutron flux distribution. Here the CORETRAN calculation results are also compared to the STEPAN code calculated results. CORETRAN code provides more realistic representation of the axial flux distribution (the double-humped shape of the curve). Table 10 provides the example comparison of the results of CORETRAN calculations carried out for various reactor states. Here, radial and axial peaking factors, as well as average deviations of the calculated results from the measured data are provided.

Table 11 presents the example of the calculations and comparison against the Ignalina NPP data(for Unit 1 and Unit 2). The comparison with the STEPAN code results (which were obtained using WIMS-D4 cross section library) is also presented. In most of the cases, the calculations, performed with the HELIOS cross-section library, provide better agreement with the experiment data. Here $a_j, a_w, a_t, a_C, \Delta r_{MCC}, \Delta r_{CPS}$ are respectively the void reactivity coefficient, the power reactivity coefficient, the fuel temperature reactivity coefficient, the graphite temperature reactivity coefficient, the MCC voiding effect and the CPS voiding effect.

4.6.3. Transient calculations

A number of RBMK-1500 transient calculations was carried out. Calculations of all transients within the scope of the RBMK-1500 safety analysis report (Chapter 4.4) for the 3-D neutronic code calculations were performed. The most interesting results of the transient calculations are presented in this Chapter.

4.6.3.1. Spontaneous withdrawal of a control rod

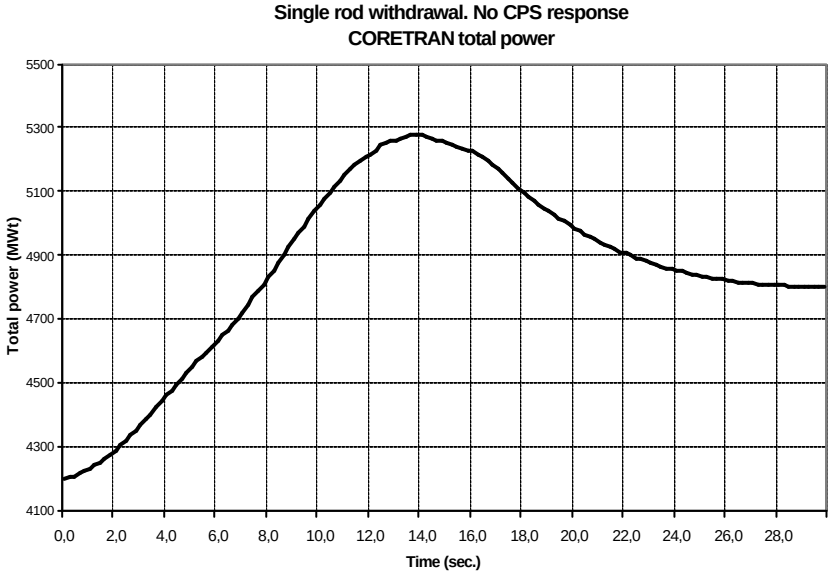

Figure 37. Reactor power during transient with no CPS response.

The spontaneous withdrawal of one control rod represents the Anticipated Transient Without Scram (ATWS) case, which is considered to be beyond design basis accident for the RBMK type reactors. The aim of the transient calculations was to test the operation of the RBMK CPS logics, coded into the CORETRAN and to evaluate the safety limits (maximum cladding temperature) in the maximum power fuel channel. The simplified one-dimesional VIPRE-02 thermal-hydraulic model of the fuel channel was used during the calculations.

Spontaneous withdrawal of one control rod at the periphery of the core was analyzed. All CORETRAN calculations were performed using the actual reactor data (power, flow rates, insertion depths of the control rods, radial and axial power profiles) recorded at the Ignalina NPP. For the reactor database, the core state of January 27, 2001 of the Ignalina NPP Unit-1 was chosen.

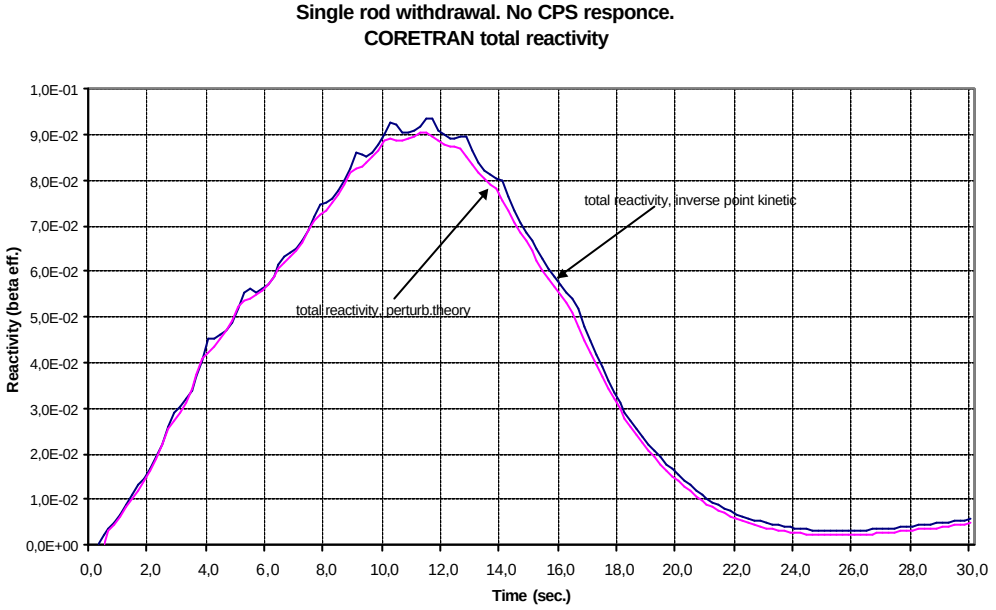

Figure 38. The reactivity behavior during the transient with no CPS response.

Figure 37 presents the reactor power behavior during the transient, in a case, when the LAC-LEP system is not in operation (no automatic control is performed, the reactor power was changing due to the reactivity feedbacks only). The reactor power increases by 25% by the time the control rod is fully withdrawn. Later on, due to the reactivity feedbacks, the reactor power stabilizes at the new power level, 145 MW_{th} higher the initial power. The CORETRAN estimated efficiency of the withdrawn control rod is close to 0.1 β_{eff}, which is close to the average worth of the control rods in RBMK-1500 type reactors.

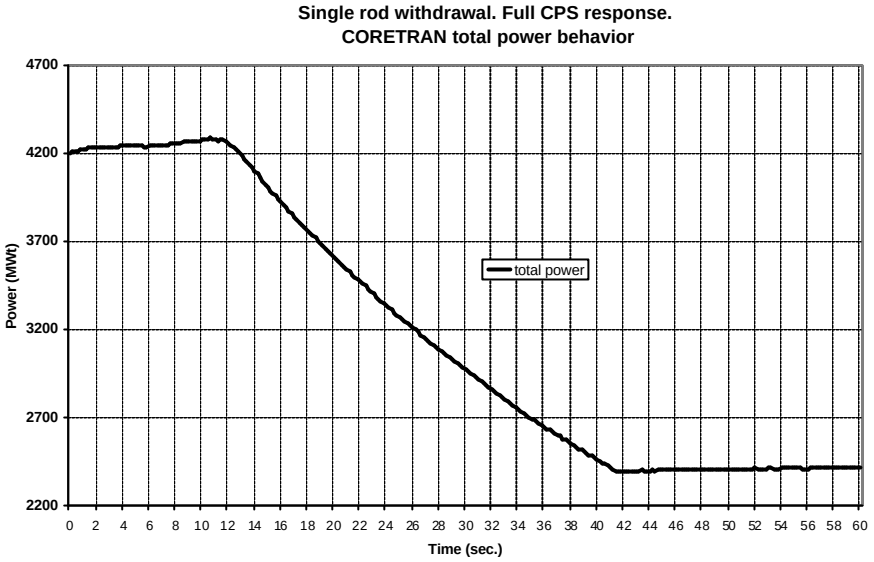

Figure 39. Reactor power during transient with CPS response.

The maximum reactivity value is reached at about 2 sec earlier than the power maximum. CORETRAN calculations also had shown that the 2 methods for reactivity calculations (by perturbation theory and point kinetics) provide close predictions of the reactivity, but the point kinetics model, which is used during the experimental measurements at the RBMK type reactors provides slightly greater reactivity values (Figure 38).

Figure 39 shows the comparison of the reactor power calculated with CORETRAN code with LAC-LEP system active. The values are compared to those, obtained using the Russian code STEPAN.

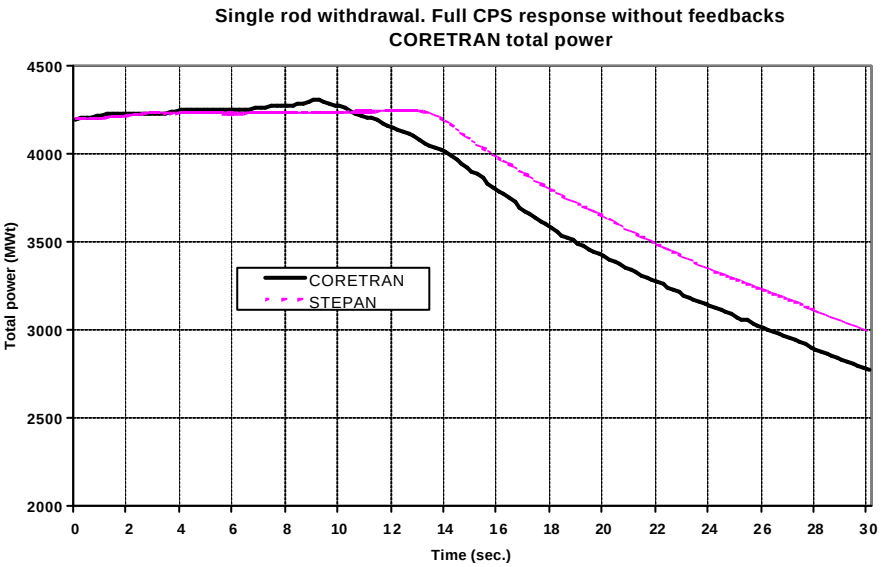

Figure 40. Reactor power during transient with CPS response without feedbacks.

The control rod was fully withdrawn after about 15 seconds from the beginning of the transient. According to the Figure 39, at approximately 10^{th} second of the transient, due to the local change in power in two reactor regions being close to 10%, the emergency reactor power reduction signal AZ-3 was generated. This signal enables the reactor power reduction by 50%. After about 41 second, new power level at 50% of the initial power was reached, and the further movement of the control rods stabilized the reactor at this power level. All the process was calculated automatically, i.e. according the CPS logic, implemented into the CORETRAN. CPS system ensured the stabilization of the reactor power at the new level of 50% (set-point values for the automatic regulation were automatically adjusted by the code for the new power level).

The analysis of thermal hydraulic parameters variation during this transient showed that no design safety limits for fuel, cladding temperature or fuel channel wall temperature were violated during the transient, as the reactor power reduction signal was generated soon after the reactor power started to increase. The maximum fuel temperature of 1411°C to 19.5 sec of the transient, which is below the fuel temperature limit (2100°C). This set of CORETRAN calculations proved the functionality of the RBMK-1500 CPS logics, coded into the CORETRAN.

4.6.3.2. Flow rate blockage in one fuel channel

The other type of transient, presented here, is the flow reduction in the fuel channel while reactor is operating at the nominal power (4200 MWth). The reason of coolant flow rate decrease in one channel can be a flow blockage or erroneous closure of the channel isolation valve. The coolant flow rate decrease in one or several channels is also possible due to the coolant flow rate blockage in one of the group distribution headers.

The calculations were performed in order to evaluate the time limits until the maximum allowable cladding temperature is reached due to the full and partial flow blockage. The flow rate blockage in the channel is a condition for manual reactor shutdown. This case is dangerous because other means to cool the fuel channel (FC) would be inaccessible. Three events of flow rate blockage in a FC during RBMK-1500 reactor operation have occurred at the Ignalina NPP (INPP SAR, 2001). All cases have resulted in burn-through of the channel. These failures did not develop into a severe accident – ALS localized release of radioactive steam-water mixture from the reactor core. Neighboring FCs were not damaged. The replacement of an old design with a new design of the isolation valves in Ignalina NPP eliminated the possibility of a complete coolant flow rate blockage in a FC. Therefore two cases were investigated: full flow blockage and partial flow blockage (25% of initial flow) of one fuel channel.

The analysis of this transient was performed out in two steps: first 3-D neutronic calculations of the reactor were carried out. Afterwards, the data from the neutronic calculations (change of axial power profiles along time) were supplied as boundary conditions for a detailed subchannel model of RBMK-1500 fuel channel for VIPRE-02 thermal hydraulics analysis.

Results of CORETRAN 3-D neutronic calculations

Figure 41 shows the reactor power behavior during the full flow blockage transient. The results of calculations, performed with the LAC-LEP system in operation provide a higher power level during the transient. The CORETRAN calculations were carried out using two different neutron cross section data libraries. The HELIOS and WIMS-D4 code generated cross section data libraries were used. The CORETRAN calculated power profiles, obtained with the active LAC-LEP system were used in the thermal-hydraulic analysis.

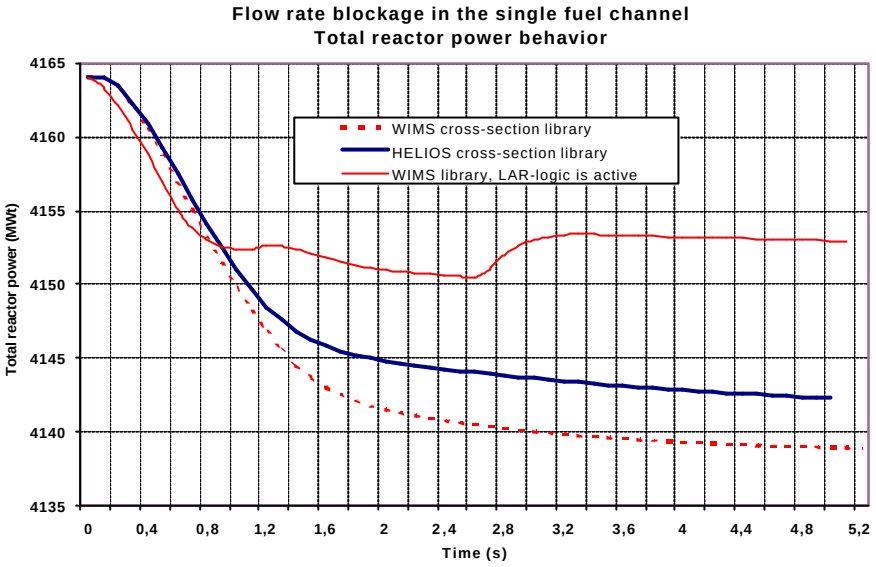

Figure 41. CORETRAN calculated reactor power during the transient.

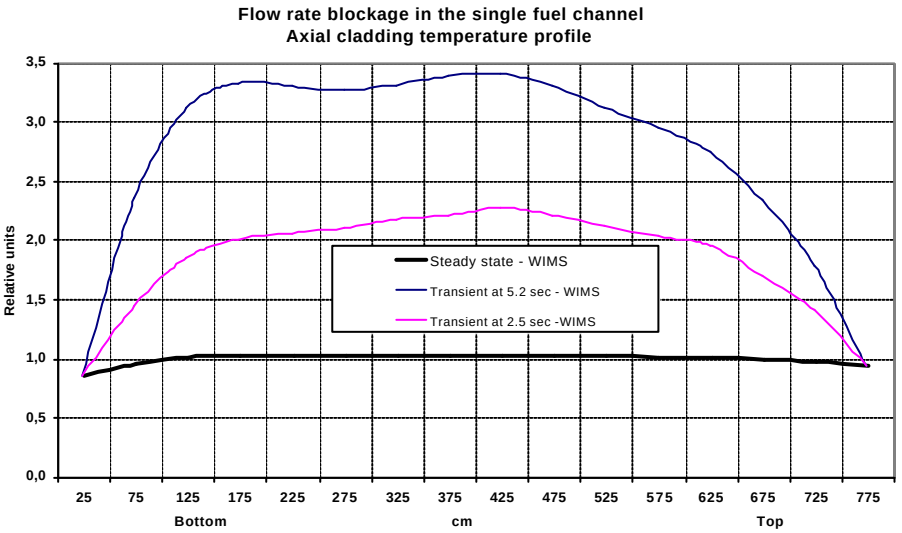

Figure 42. CORETRAN calculated average cladding temperature during the full fuel channel blockage transient.

The CORETRAN calculated changes in axial temperature profiles of the cladding are presented on the Figure 42.

VIPRE-02 model and calculation results

In order to assess the fuel cladding integrity, one needs to investigate the maximum fuel cladding temperatures during the transient. In order to do that, the VIPRE-02 code input was developed for a single RBMK-1500 fuel channel.

The fuel channel was divided into 30 square and triangle subchannels (Figure 31). The axial power profiles obtained during the CORETRAN 3-D neutronic transient calculations were used as an input data for the thermal hydraulic analysis. During the VIPRE-02 code studies (see Chapter 3) it was determined that the RRC KI CHF correlation (Osmachkin, 1974) added to the code by the author, and the Bowring CHF correlation, implemented in the standard VIPRE-02 code version provide the closest agreement for the CHF occurrence in RBMK-1500 reactor upper fuel assemblies. For the lower fuel assemblies, EPRI CHF correlation, implemented in the standard VIPRE-02 version, provides a good agreement with the experimental data. These CHF correlations were used in the thermal hydraulic VIPRE-02 analysis, presented here.

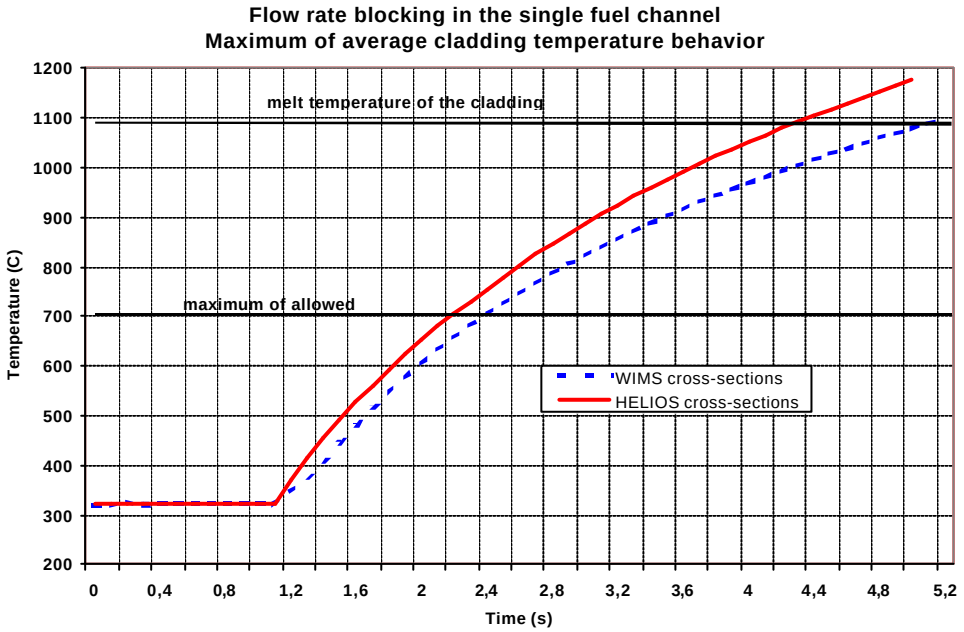

Figure 43. The maximum cladding temperature during full flow blockage transient.

Figure 43 shows the VIPRE-02 calculated maximum cladding temperatures for the full flow blockage case. The analysis of the transient with the full flow rate blockage in one fuel channel shows, that the fuel cladding temperatures increase very rapidly and that the melting point for the cladding is reached in about 5 seconds.

Calculations of the partial flow blockage in a fuel channel were performed under assumption that the flow was reduced to about 25% of the initial value due to the erroneous closure of the channel isolation valve (the new valve models, recently installed in the RBMK-1500 type reactors prevent the full closure of the valve). It was assumed that the valve was closed manually and the valve closure time was 30 seconds.

The maximum cladding temperatures (for the fuel rod No.6 at the inner ring of the fuel rods in RBMK-1500 fuel assembly; see Figure 31) during the partial valve closure transient are presented on the Figure 44. The reduction of the flowrate in the channel started at t=10 sec (after the initial steady state). After about 10 seconds, when the flowrate in the channel was about 75% of the initial flow rate, the increase of the cladding temperature had begun. Even more rapid increase in the maximum cladding temperature started at t= 35 sec, when the coolant flow rate became 35 % of the initial flow. The flow reduction stopped at t=40 sec, with the flow rate through the channel equal to 25.7 % of the initial flow. The maximum cladding temperature continued to increase for the next 40 seconds, and after t=80 s stabilized at a temperature of 685°C. This temperature is very close to maximum allowed temperature (700°C) of the cladding for RBMK-1500 fuel rods.

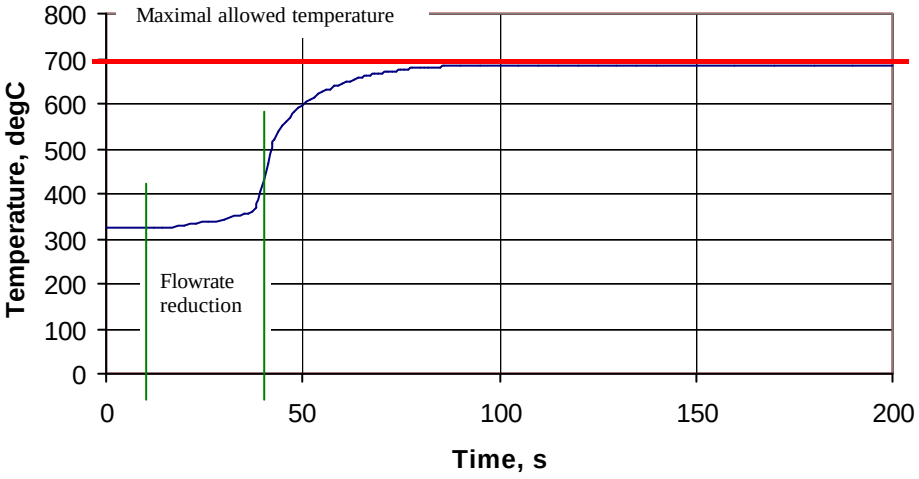

Figure 44. The maximum cladding temperature during partial flow blockage transient.

The CORETRAN calculated axial power profile for the fuel channel, which was used for the calculations, presented here is shown on the Figure 45. The Figure presents the normalized (to unity) axial power profile at the transient time t=41.0 sec. The power profile changed very little from t=41 sec to the end of the transient, therefore for the VIPRE-02 calculations it was assumed that profile was constant for t=41-200 sec.

Figure 46 presents the VIPRE-02 calculated cladding surface temperature profile at transient time t=200 sec. As it is seen from the Figure, the critical heat flux is reached at the elevation of about 4 m. However, due the non-uniformity of the axial

power distribution (lower heat flux at the upper part of the fuel assembly) along the axis at the fuel assembly, the sufficient amount of heat can be removed in transition and film boiling modes and the maximum allowed cladding temperature is not exceeded, i.e. the decrease of the heat transfer coefficient in the post-CHF region is compensated by the overall decrease of the heat flux in the upper part of the fuel assembly.

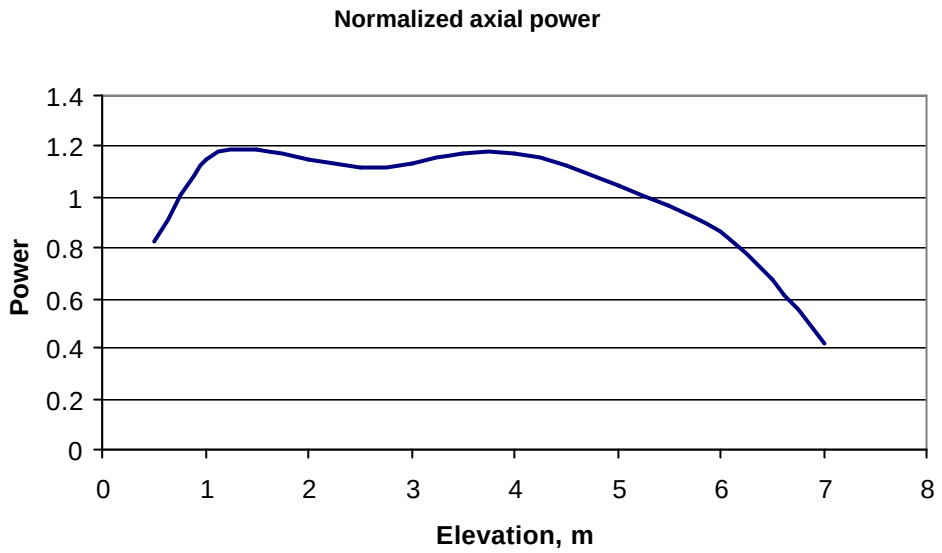

Figure 45. CORETRAN calculated axial power profile for t=41 sec.

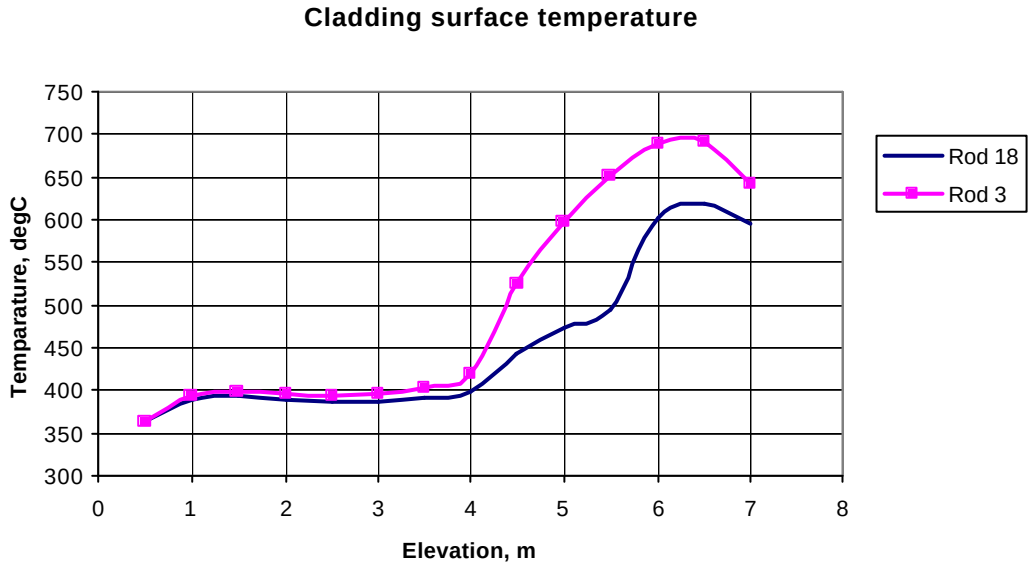

Figure 46. Cladding temperature at t=200 sec.

Figure 46 presents the calculated cladding temperatures for the fuel rod in the inner row of the fuel assembly (rod No. 3) and rod in the outer row of the assembly

(rod No. 18). As it is seen from the Figure, the VIPRE-02 predicted lower cladding temperatures for the fuel rods in the outer row.

The thermal hydraulic analysis of the flow reduction transient with VIPRE-02 code showed that with the flow reduction to the minimal value (through the new type of isolation valves of RBMK-1500 fuel channels) the safety limits of the fuel channels are not violated, although the maximum cladding temperatures are close to the limiting values.

4.6.3.3. Control and Protection System Loss of Coolant Accident (CPS LOCA)

This transient is considered to have the most positive reactivity input in the RBMK type reactors and therefore was chosen to be analysed in the scope of this Thesis. During the calculations, the assumption was made that all the emergency protection systems, which are outside the core region were not operational. No precise data about the CPS channel voiding rates during the transient and the conditions (e.g. the distribution of the flow rates in various parts of the core) is available. Usually for the RBMK-1500 analysis it is assumed that the level of the coolant in the CPS reaches the core bottom level at 44 seconds after the beginning of the CPS LOCA.

The analysis of this type of transient with CORETRAN code was performed for 3 different cases: CPS voiding time was assumed to be 30 seconds; CPS voiding time 44 seconds and CPS voiding time 44 seconds plus a single failure (first signal from the in-core detectors is ignored and does not initiate the CPS activation).

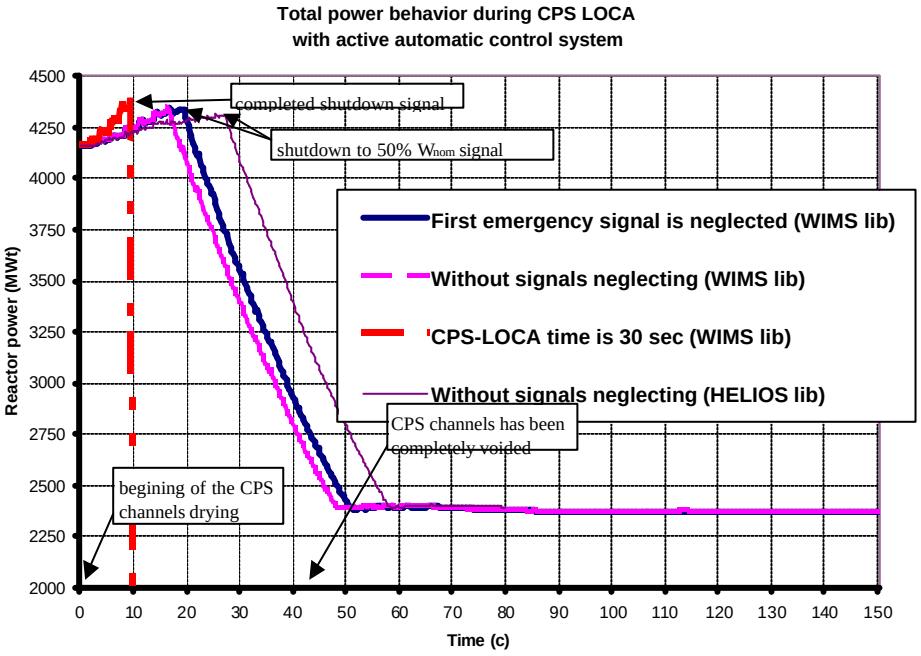

Figure 47. CORETRAN calculated reactor power during CPS LOCA transient.

During the CORETRAN calculations, the following additional assumptions were made:

- All CPS channels lose coolant at the same rate (i.e. the coolant level reduces at the same rate in all regions of the core);
- Technological set points, according to which the reactor scram signal is generated, are neglected. The transient starts at time zero, i.e. at the moment when the coolant level in the CPS system reaches the top of the reactor core;
- LAC-LEP system is in operation.

The results of CORETRAN calculations are presented in the Figure 47. The calculations were conducted using two sets of neutron cross section libraries, generated with HELIOS and WIMS-D4 codes. In the case when the CPS system voids in 30 seconds (Figure 47), the CPS detectors generate full reactor scram signal in about 10 seconds after the beginning of the transient, due to the CPS signal, initiated by the increase of the reactor power by more than 10%. If the CPS system voids in 44 seconds (Figure 47), CORETRAN calculations using both WIMS-D4 and HELIOS neutron cross sections results in the generation of AZ-3 signal, which reduces reactor power to 50% of the nominal power level. No full reactor scram signal is generated. During the CORETRAN calculations with WIMS-D4 cross section library the reactor power reduction signal is generated 10 seconds earlier, compared to the case when HELIOS cross section data are used. This could be explained by the fact that the HELIOS code estimates higher efficiency of the control rods (i.e. higher absorption cross sections).

The calculated case implies, that the control and protection system of the RBMK-1500 reactor is capable of handling even the transient with the most positive reactivity addition without having to scram the reactor, i.e. LAR-LEP systems ensure the operation of the reactor at the reduced power level even after the coolant is no longer present in the control and protection system circuit.

In the case when the single failure criterion was used (first signal, generated by the control and protection system was neglected) during the CORETRAN calculations (Figure 47), the delay of the system response was 2 seconds.

The continuous operation of the reactor at the reduced 50% power level in the case of the CPS LOCA prompted to perform more detailed thermal hydraulic analysis of the transient using VIPRE-02 code, as for the case of reactor operation with voided CPS system the risk of overheating of the CPS channels has to be evaluated.

VIPRE-02 model and calculation results

The CPS channels are located and cooled independently from the fuel channels (Almenas, et al, 1998). This diversity ensures the safety of the CPS channels and subsequently could result in operability of enclosed control elements in case of accidents due to fuel channel loss of coolant. Manual control rods, shortened absorber rods and fast-acting scram system rods are placed within the CPS channels. Cooling system of CPS channels is intended to provide coolant circulation to keep the

temperature of the channels and instrumentation installed within the required limits. The system performs the following operational tasks: keeps coolant temperature equal to 40°C at the inlets of CPS and reflector cooling channels; removes heat from CPS channels, control rods, control rod drives, power density sensors; keeps required quality of water used to cool CPS and reflector cooling channels. Aluminum alloys are used for the CPS equipment. They have good corrosion resistance in the water at temperatures 100-250^{o}C. Maximum permissible temperature for these alloys is 190^{o}C. The aim of the VIPRE-02 calculations was to evaluate how rapidly this safety limit would be violated in the case if the reactor continues operating at 50% of the nominal power with the voided CPS.

The schematic VIPRE-02 model of the CPS channel is shown on the Figure 48. The CPS channel with a control rod and four surrounding fuel channels were modeled. It was assumed that the heat transfer area from the surrounding fuel channels to the neighboring CPS channel is equal to ¼ of the total heat transfer area of the fuel channel. Each channel in the RBMK type reactor is located in a separate graphite block, at the pitch of 25 cm. Therefore, in order to calculate the heat transfer between the structures the corresponding mass of the graphite has also be taken into account in the model. Figure 48 indicates the equivalent graphite heat transfer area, which was modeled in VIPRE-02. Manual Control Rod (MCR) was modeled in the center of the CPS channel. The MCR inner and outer surfaces are made of aluminum alloy and B_4C absorber material is located inside. The specific heat and thermal conductivity of graphite, aluminum alloy and boron carbide were supplied as additional user-specified material data for the VIPRE-02 input. The graphite blocks between fuel and CPS channels were modeled as wall elements. The control rod surface temperature in a CPS channel, surrounded by 4 fuel channels of the highest power, was calculated.

Besides heating up of the control rod due to the heat conduction and radiation from the surrounding fuel channels, the heat production in the absorber material has also to be taken into account. The amount of heat produced by neutron and gamma absorption can be estimated as (El-Wakil, 1971):

$$q''' = mI + \Sigma_a f \Delta E \qquad (37)$$

Where μ - gamma absorption coefficient, I – intensity of gamma radiation, Σ_a-neutron absorption cross section, ϕ - neutron flux, ΔE – energy per neutron reaction.

In the case of RBMK-1500 reactor, the neutron and gamma fluxes in the absorber of the manual control rod were calculated using the HELIOS code model for the RBMK-1500 lattice. A quarter cell of 3×3 HELIOS model used for the transport calculations is described in the Chapter 2. The CPS channel was surrounded by fuel channels of the average burnup (11 MWd/kg). As the result of the HELIOS calculations, the neutron and gamma fluxes in absorber and the macroscopic absorption cross sections for each neutron energy group were obtained. The calculations were carried out in 18 gamma and 45 neutron energy groups. The HELIOS predicted heat production rate in the absorber due to the neutron and gamma absorption was equal to 0.4 W/cm^3 of the absorber material (for the case, when

reactor is operating at 50% of the nominal power and no coolant is present in the CPS).

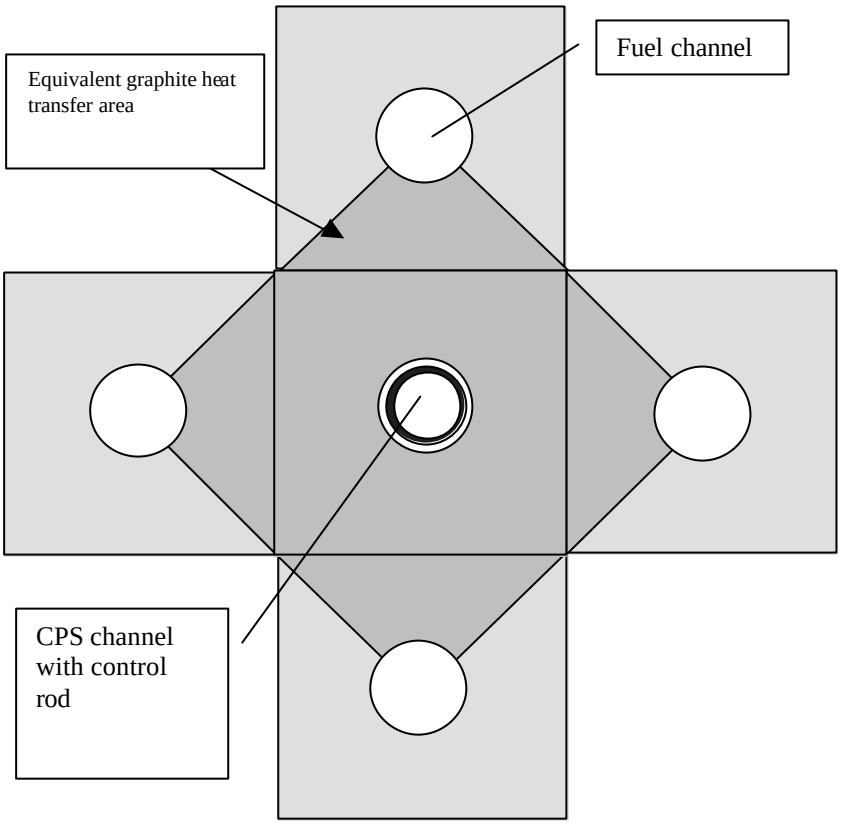

Figure 48. VIPRE02 model of CPS and surrounding fuel channels.

Figure 49 shows the VIPRE-02 calculated maximum control rod surface temperature during the CPS LOCA transient. The axial power profiles along time were obtained from CORETRAN 3-D neutronic calculations.

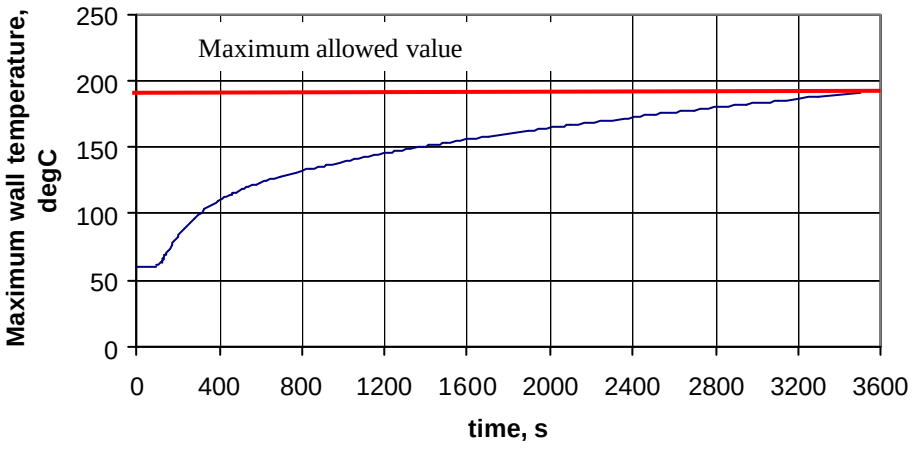

Figure 49. Maximum control rod surface temperature during the CPS LOCA.

The model was verified applying it for the nominal reactor power calculations. According the Ignalina NPP data (LEI, 2002), the coolant flow rate in the CPS channel under the nominal operation conditions is 4 m^3/hour. The nominal coolant temperature at the CPS channel input is 40°C and at outlet 75°C.

The VIPRE-02 calculations with the model presented above were carried out for the nominal reactor power operation. The neutron and gamma fluxes were calculated with HELIOS for the reactor nominal power level of 4200 MW_{th}. The calculated coolant temperature along the CPS channel is shown on the Figure 50. As it is seen, the temperature in the CPS channel is predicted correctly for the nominal reactor operation conditions.

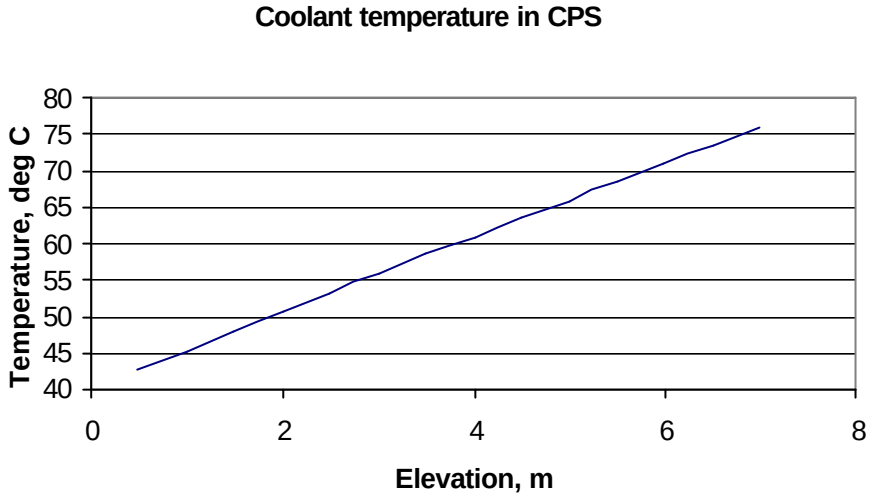

Figure 50. Coolant temperature in CPS channel during the nominal reactor operation.

For the first 100 seconds of the transient (Figure 49) the steady state transient was performed. The CPS LOCA begins at t=100 sec. At 144 seconds, the CPS channel is completely voided. At this time, the reactor power is also reduced to 50% of the nominal power. The further transient calculations show an increase of the control rod surface temperature and maximum allowed aluminum alloy temperature is reached at t=3400 sec after the beginning of the transient. The RBMK-1500 safety analysis guidelines (INPP SAR-2, 2001) indicate that the time before the reactor operator takes actions during the transient should be equal to 30 minutes, and cannot be less than 10 minutes in any case. In the case of the CPS LOCA transient, even if the reactor continues operation at the power level of the 50% of nominal power, the safety limits for the CPS rod surface temperature are not violated for almost 1 hour from the beginning of the transient.

This work was probably the first study of this kind – to evaluate control rod surface temperatures in RBMK-1500 during the CPS LOCA transient. The further model and code assessment in necessary in order to fully evaluate the performance of the presented model.

4.7. Major findings and accomplishments

The CORETRAN code was adopted for the RBMK-1500 type reactor calculations. The methodology was developed and implemented into the code and the code calculation results were verified against RBMK-1500 plant data for the cold and hot steady state and transient conditions.

In general, CORETRAN code calculations provide good agreement with the experimental results (and with the STEPAN code calculations). CORETRAN code provides closer agreement to the to experimental value for the power reactivity coefficient, compared to the STEPAN code.

The operation of CPS LAC-LEP logics, coded into the CORETRAN code for RBMK-1500 reactor was tested. Some examples of the transient calculations are presented in this Thesis. In particular, the analysis of the spontaneous withdrawal of one control rod has shown that the CPS logic reduced the reactor power to a new power level, as done in actual reactor operation. No violations of the safety limits were calculated during this transient.

A number of anticipated, postulated and ATWS transient calculations were performed. In particular, transient calculations of the spontaneous withdrawal of one control rod and a group of control rods in core center and core periphery (ATWS case), Control and Protection System Loss of Coolant Accident, erroneous reloading of one fuel assembly, drop-out of a shortened MCR rod were simulated. The calculations were carried out using HELIOS and WIMS-D4 generated neutron cross section libraries. In most of the cases the CORETRAN results were benchmarked with the STEPAN code. The developed analysis methodology based on HELIOS and CORETRAN codes for the RBMK-1500 core was employed for audit calculations during the Review of the Safety Analysis Report of the Ignalina NPP Unit 2 (RSAR-2).

Transient calculations showed higher, than expected, level of performance of the RBMK-1500 reactor Control and Protection System: during both spontaneous withdrawal of one control rod and the CPS LOCA transient, the LAC and LEP control rods of the reactor proved to be capable of controlling these reactivity transients and reducing the power level to 50% in an orderly fashion. Full reactor shutdown (scram) was not predicted.

Coupled neutronics-thermal hydraulics analysis of some transients, such as the spontaneous withdrawal of one control rod, full and partial flow blockage in one fuel channel and Control and Protection System Loss of Coolant Accident (CPS LOCA) were investigated and results are presented. The aim of the calculations was to evaluate the safety margins (maximum fuel cladding and control rod surface temperatures) during the transients. The coupled calculations were carried out and the variation of axial power profiles as a function of time, obtained as a result of 3-D neutronics calculations was supplied as a boundary condition for the VIPRE-02 code thermal hydraulic calculations. The VIPRE-02 thermal hydraulic model of the CPS

channel and surrounding fuel channels was developed in order to evaluate the increase of the temperature of the control rod surface during such type of transient. It was determined that, with the assumptions employed, the safety limits, even in this transient, would not be violated for about 1 hour after the beginning of the transient.

The main results of the work, presented in this Chapter, demonstrate that a fully functional and independent RBMK-1500 core analysis methodology was developed, verified and validated. The methodology is based on the HELIOS and the modified CORETRAN code. The methodology has been employed in a number of RBMK-1500 core design base and beyond design base core transient calculations and it was demonstrated that the methodology provides reliable results.

Chapter 5

Investigations on the Coolability Potential of the CRGTs During a Severe Accident in a BWR

5.1. Objectives

This Chapter describes the investigations on the in-vessel retention of the corium melt, during a postulated severe accident in a BWR. All BWR designs contain a large number of control rod guide tubes (CRGTs) in the lower head. These guide tubes are quite massive and contain appreciable heat capacity. They also have an annulus region through which there is a steady supply of subcooled water at the operating pressure. This offers a significant capacity to remove the decay heat generated in the melt several hours after the reactor shutdown. The aim of this work was to investigate this potential for the additional decay heat removal, offered by the presence of the CRGTs.

5.2. Introduction and background

The postulated severe accident scenario for a BWR, in general, results in the core melt transferring from the original core geometry to the lower head of the reactor pressure vessel. The BWR vessel being larger than that of a PWR, containing a number of control rods and a larger quantity of water will provide the conditions for core melt to break up and form a debris bed. This heat generating debris bed could become dry if water supply to the vessel is not resumed and in time could melt and form a melt pool in the lower head. This melt pool would start natural circulation and in time, it is possible that the vessel would fail due to the thermal loading imposed.

It has been recognized by almost all of the reactor safety community that it would be wise to retain the core melt within the reactor pressure vessel (RPV) and prevent vessel failure. During the late phase of in-vessel accident progression a particulate debris bed or a core melt would accumulate in the lower head of the RPV and will fail the lower head unless cooled and stabilized. The accident management strategy of adding water to the lower head full of a melt pool has been found to be unsuccessful in cooling the melt pool (Sehgal et al 2003). Additional cooling of the vessel from outside is needed to cool the debris bed/melt pool. This recognition has resulted in the design of the evolutionary reactor designs: AP-600, AP-1000, SBWR-1000 and the Korea Advanced PWR (KSNP – Korea Standard Nuclear Plant) employing the accident management strategy of establishing a water pool in the PWR cavity or

BWR drywell submerging the RPV, which should provide the additional heat removal on the outside of the RPV to keep it cool and retain the melt within the vessel lower head.

The Swedish BWRs designed by the ASEA Co. have a lower drywell and the vessel is very high above the bottom of the lower drywell. The accident management strategy employed by the Swedish BWRs establishes a pool of water in the lower drywell of 7 to 11 meters depth. The water level, however, is much below the vessel lower head and cannot cool the lower head containing the core particulate debris or melt.

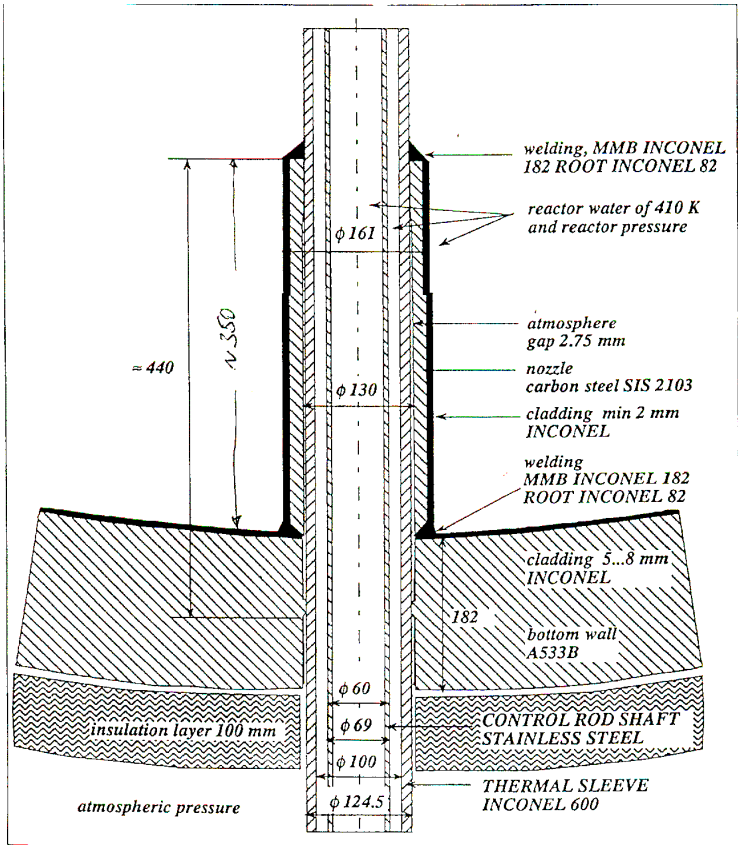

Figure 51. The bottom part of the Control Rod Guide Tube (CRGT) in the BWR-75 reactor.

All BWR designs contain a large number of stainless steel control rod guide tubes (CRGTs) in the lower head. The CRGTs support (a) the B_4C-steel cruciform control blades which traverse through the height of the core and (b) the fuel subassemblies. Thus, these guide tubes are quite massive and incorporate appreciable heat capacity. They also have an annulus region through which there is a steady flow of subcooled water at the operating pressure. The flow rate, however, is not large; e.g., in the TVO plant in Finland, the flow rate/CRGT is 62.5 grams/sec. This water flow, however, has sufficient heat capacity to remove the decay heat after an accident. The question then, is whether the cooling capacity inherent in the heat capacity and the water supply of the multitude of CRGTs can be employed to cool the debris bed/melt pool that may be

formed in the lower head of a BWR as a result of a severe accident, and thereby prevent vessel failure.

This is the subject of the investigations described in this Chapter. The approach of the study was to perform well-scaled experiments with simulant materials employing heat transfer conditions representative of the prototypic accident. Thus the the binary oxide melt composition employed had sufficiently high liquidus and solidus temperatures and formed crust on the cool surfaces of the CRGT and protected it. The scaling strategy employed a unit cell concept per CRGT, i.e., the particulate debris material mass and the melt mass associated per CRGT was employed. The CRGT dimensions were nearly prototypic and so was the heat input to the debris or melt surrounding a CRGT.

The actual dimensions of the prototypic CRGT in the ABB's BWR-75 reactor were used, in order to develop a clear rationale for scaling in this experimental program. The design and dimensions of the lower part of the CRGT are presented in the Figure 51.

5.3. Scenario

The postulated severe accident scenario focussed here is that of a depressurized BWR lacking any water supply in which the water level has dropped below the core plate. The heat up of the core leads to core melt down and the accumulation of melt above the core plate. The core plate and the fuel assemblies are supported by the numerous control rod guide tubes situated in the lower head. The corium melt discharge from the core region to the lower head occurs through the holes in the core plate. Since the corium jets are not of large diameter and the volume of water in-between the CRGTs is not large, it is expected that there will not be any steam explosion, the corium will break up into particles and will be quenched. A large volumetrically-heated particulate debris bed will be formed in the lower head.

The scenario continues with the postulate that the feed or the ECCS water supply to the RPV is not restored, leading in turn to evaporation of the water in the lower head and dryout and heat-up of the particulate debris bed, which will, in time, form a melt pool. It is assumed that the water supply to the CRGTs is not lost during the accident and the CRGTs do not melt or collapse when the debris bed heats up and later forms a melt pool.

The scenario postulates that the water supply to the vessel is restored when the lower head is full of either a hot debris bed or a melt pool and a water layer is established at the top surface. Clearly, if the water supply is not restored long after the melt pool is formed and the natural circulation is established in the melt pool, the integrity of the CRGTs will be threatened even with the presence of a crust on their exterior walls, since the water flow rate in the CRGTs is not large. However, since the debris heat up process is not coherent and the time to convert the debris bed to a melt pool takes about 2 hours, there is a substantial time window in which many of the CRGTs could survive and be available for enhancing the coolability of the melt in the lower head. For the purposes of this study we have assumed that the hot debris bed or

melt pool surrounds the CRGTs which have a prototypic water flow rate and that the crusts formed on the outer walls of the CRGTs have preserved their integrity. The melt pool is then flooded from the top. The study investigates whether the heat removed by the mass of the CRGTs and by the water flowing inside the CRGTs substantially aids in achieving coolability (quenching) of the debris bed/melt pool, thereby preserving the integrity of the lower head and retaining the debris/melt in it.

5.4. Test Facilities

5.4.1. POMECO test facility

The POMECO (POrous MEdia COolability) facility was designed for experimental studies on coolability of heat generating particulate debris beds. The test section was a stainless steel vessel with the cross section of 350×350 mm. Total height of the test section was 1400 mm, which included the upper vessel where water was supplied. Up to 370 mm high sand bed could be formed to simulate the debris. The test section contained an annular pipe of the same dimensions as the prototypic CRGT in a prototypic BWR (the TVO BWR). One CRGT and the debris mass associated as a unit cell was represented in POMECO. The decay heat for the scenario was chosen as that appropriate for 3-4 hours after the scram, i.e. about 1 MW/m^3. The maximum power available for the sand bed was 46 kW, which corresponds to the volumetric power of about 1 MW/m^3, for the POMECO vessel sand bed dimensions.

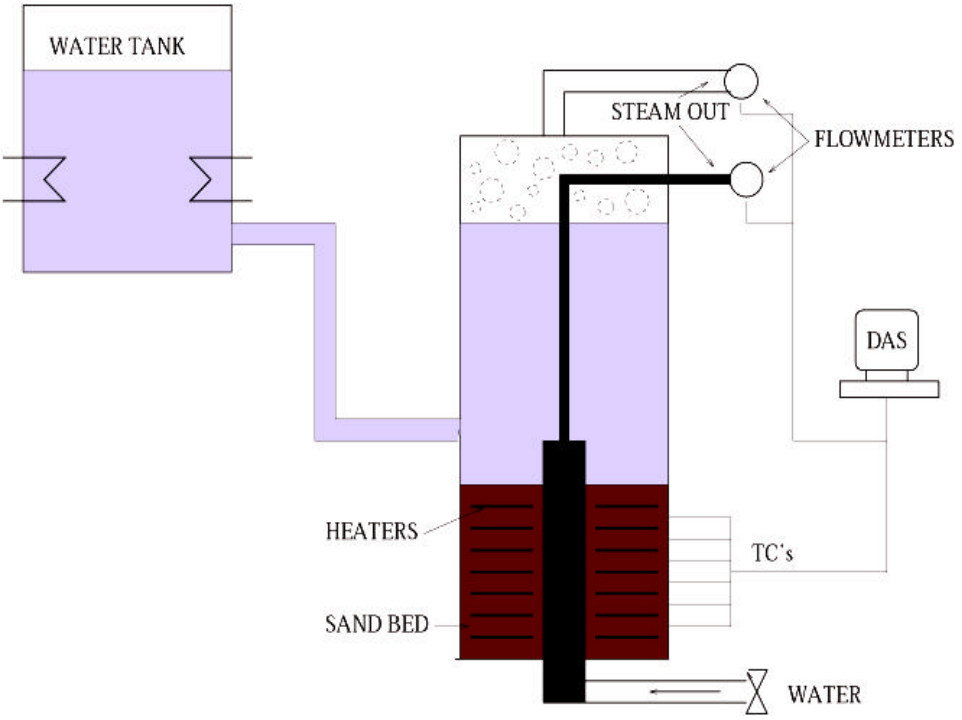

Figure 52. POMECO test facility.

The schematic of the POMECO (POrous MEdia COolability) facility, modified for this study to include the CRGT is shown in the Figure 52. The POMECO facility

consisted of water supply system, test section, heater power supply, instrumentation and the data acquisition (DAS) systems.

Some details of the test section are presented on the Figure 52 and 53. The height of the lower part is 500 mm and the height of the upper part is 900 mm. Figure 53 (b) also shows the configuration of the heaters and the thermocouples contained in the sand bed. Figure 53 (a) shows the axial cross section of the actual CRGT, which is employed in the sand bed contained in lower part of the POMECO facility.

The upper part of the CRGT annular pipe was closed with the cover, which contained holes. These holes were of the same flow area as the bypass inlet in the prototypic CRGT. The holes were designed to be open or closed. A pipe was connected to the cover of the CRGT annular pipe and it was led out of the POMECO facility, so that the steam generated in the annular pipe can be measured separately from that generated from the sand bed. The CRGT pipe was connected to a water line at the bottom, which could supply the same (or different) rate of water flow to the CRGT as in the prototypic BWR.

Thirty-three thermocouples were distributed at different locations in the particle bed as shown on the Figure 53 (b). To obtain the axial temperature variation and to determine the heat flux in the CRGT wall, 9 thermocouples were embedded at three different wall depths (Figure 53 a) and at three different axial positions along the CRGT height.

The dryout tests were started with a fully water-saturated bed. The power input to the bed was increased in small steps until the dryout (i.e. the sudden increase in debris bed temperature) was recorded.

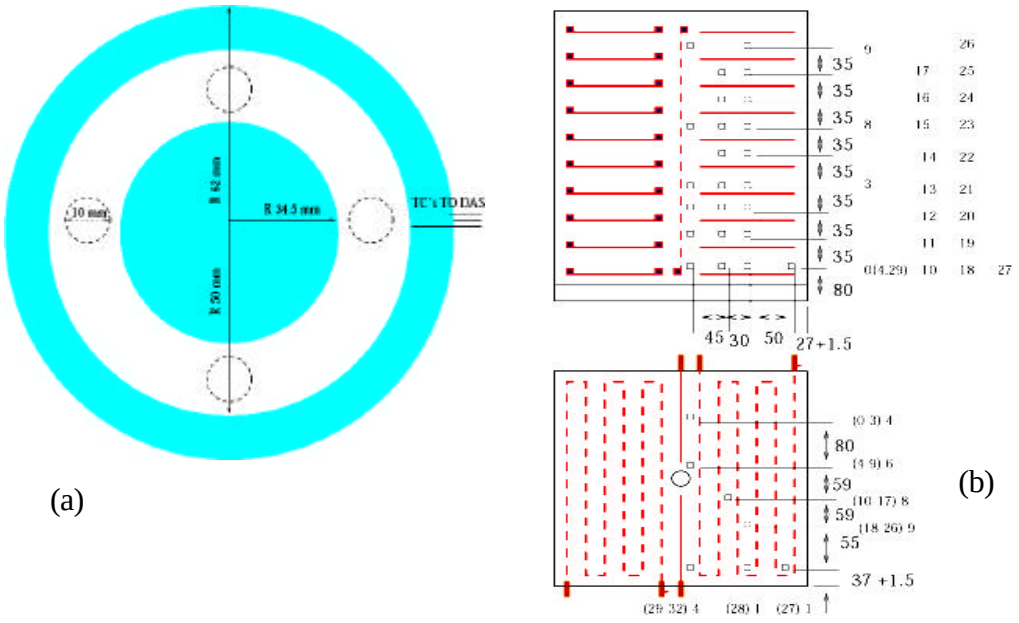

(a) (b)

Figure 53. CRGT design, heater and thermocouple distribution.

The quenching experiments were carried out by establishing a column of water above the dry particulate beds, which were initially heated up to 500ºC. All experiments were performed at atmospheric pressure.

5.4.2. COMECO test facility

The dimensions of the COMECO facility were smaller than the dimensions of the corresponding unit cell of the prototypic BWR. Therefore another scaling relation had to be introduced in order to maintain the correct representation in the experiment of the prototypic geometry of the CRGT unit cell.

COMECO facility (Figure 54) consisted of a test section (200 × 200 mm cross section), with the maximum melt pool height of 300 mm. The test section walls were made of 25 mm thick carbon steel. The test section was connected to the upper tank (1000 mm high). Water was supplied to the upper tank via the water line from the heated water storage. The melt pool was heated directly by heaters, located outside the test section on the four sidewalls. The heaters were made with the Molybdenum silicate ($MoSi_2$) alloy that can be operated at temperatures up to 1700°C. The four heaters could deliver the maximum power of 16 kW to the melt pool, i.e., the maximum power density in the melt pool of 1.33 MW/m^3 could be attained.

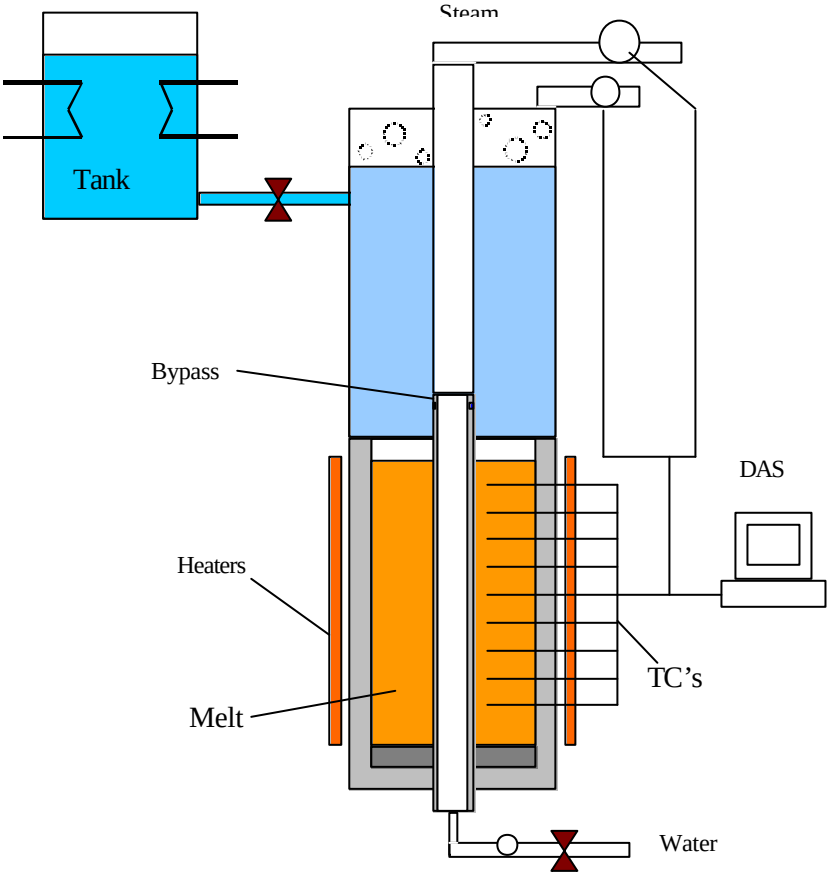

Figure 54. COMECO test facility.

The CRGT model (with the outside diameter d_o=50 mm and the inside diameter of d_i=45 mm) was placed in the center of the test section. The CRGT was connected to the water line at the bottom. Two bypass openings (of the diameter d=9 mm) were made in the upper part of the CRGT model. Flowmeters were installed on the steam outlet lines from the CRGT and the upper tank and also on the water supply line, to measure the water flowrate through the CRGT.

The temperature readings were obtained from 24 thermocouples, distributed uniformly within the melt pool. The thermocouples were placed at 8 axial elevations and at 3 radial locations within the melt pool. The distribution of the thermocouples in the COMECO facility is shown on the Figure 55.

Before the experiment, the binary oxide mixture was heated up to the initial temperature of about 1300°C in an induction furnace. The test section was also heated up to about 1100°C in order to avoid the thermal shock and deformation of the test section when the melt was poured into the test section from the induction furnace. It should be noted that at 1100°C, the melt pool has a superheat of about 120°C and the method of heating the test section from outside assures that there will be no hang up crust on the sidewalls. Afterwards, the requisite coolant flow rate was established through the CRGT and the experiments were started.

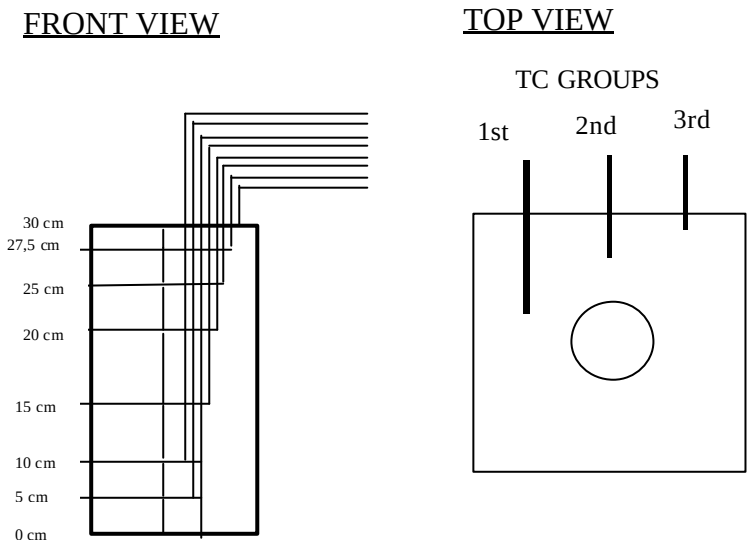

Figure 55. Thermocouple distribution in the COMECO facility.

5.5. Scaling of COMECO experiments

Scaling of experiments is an important issue since scaling distortions will prevent the extrapolation and applicability of the data obtained to the prototypic accident conditions. The experiments should be scaled as accurately as possible for both the geometry and the materials. The actual construction of the facility and/or the limitations of the operations of the experimental facility may also require additional

scaling considerations. All of these aspects are described below for the experiments performed in the COMECO facility for this study.

5.5.1. Geometrical scaling

The control rod guide tubes are arranged at a certain pitch in the lower head. They are as tall as the lower head (about 2.5 meters) and each incorporates a stainless steel rod surrounded by a tube, which provides an annulus through which water flow is maintained. In the scenario all the CRGTs are surrounded by a particulate debris bed or a melt pool.

We consider the CRGTs in the interior of the lower head and consider that part of a CRGT, along its height, which has the bypass holes. The configuration of CRGTs in the lower head is similar to that of the subassemblies in a BWR core, and a CRGT receives heat from the debris/melt at its outer surface. We have modeled the CRGT as a unit cell which will represent all the CRGTs in the interior of the lower head if it is assumed that the debris/melt composition and power density are uniform.

In the experiments employing a particulate debris bed in the POMECO facility the CRGT and the debris bed surrounding the CRGT are represented exactly as in the prototypic (TVO) reactor, i.e., the CRGT is an annulus with the prototypic dimensions and the dimensions of the debris bed outside are almost the same as in the prototypic case for one CRGT, i.e., a unit cell is constructed. The water addition rate to each CRGT was maintained the same as in the prototypic plant. The bypass flow area is also maintained the same as in the prototypic CRGT. Thus for the POMECO facility the geometrical and accident condition scaling is nearly exact.

Unfortunately, for the COMECO facility, to maintain the exact geometrical scaling would have required a volume of melt which could not be produced by our induction furnace. Thus, the test section was of the same height as that in the POMECO facility, i.e. about 35 cm, but the cross section area was considerably smaller. This necessitated reducing the size of CRGT and making it a tube instead of an annulus. The test section scaling is discussed in Section 5.5.3 below.

In the COMECO facility the heat to the melt is provided by heaters incident to each of the four sides of the test section containing the melt. Thus no crusts are formed on the test section boundaries and the test section configuration satisfies the unit cell concept for one CRGT. The heat input to the melt is increased to about 1.3 MW/m^3 in order to compensate for the lower volume of the melt surrounding the CRGT, i.e., the same total heat input per unit height is provided as in the prototypic accident conditions.

The melt pool is flooded from the top, both in the experiment and in the prototypic scenario. The CRGT water flow is exactly the same as in the prototypic plant. The bypass holes provided in the CRGT in the experiment are also sized according to the prototypic plant.

Thus for COMECO CRGT the heat input, the water flow rate are exact, while its dimensions are not, but are scaled correctly, as indicated in Section 5.5.3.

5.5.2. Material scaling

The materials employed for the construction of the CRGT in the experiments were prototypic and so was the coolant. However, the melt employed was a binary oxide melt simulating the corium (UO_2-ZrO_2) melt that would be present during the accident. The corium melt could be at temperatures exceeding 2500K with the characteristic that it would be a non-eutectic mixture with a liquidus to solidus temperature difference of ≤ 100K. The corium would form insulating crust at surfaces, which are cooler than its solidus temperature. The crust would protect the structure (such as CRGT) as long as the critical heat flux condition is not reached on the coolant-structure boundary.

The simulant material chosen should have a phase diagram similar to that of UO_2-ZrO_2, in particular for the difference between the liquidus and solidus temperature. The temperature should be sufficiently high so that the heat transfer processes are similar in their nature. The simulant material should form insulating crust. The simulant material also should be non-toxic, compatible with crucible materials, which can couple with an induction furnace.

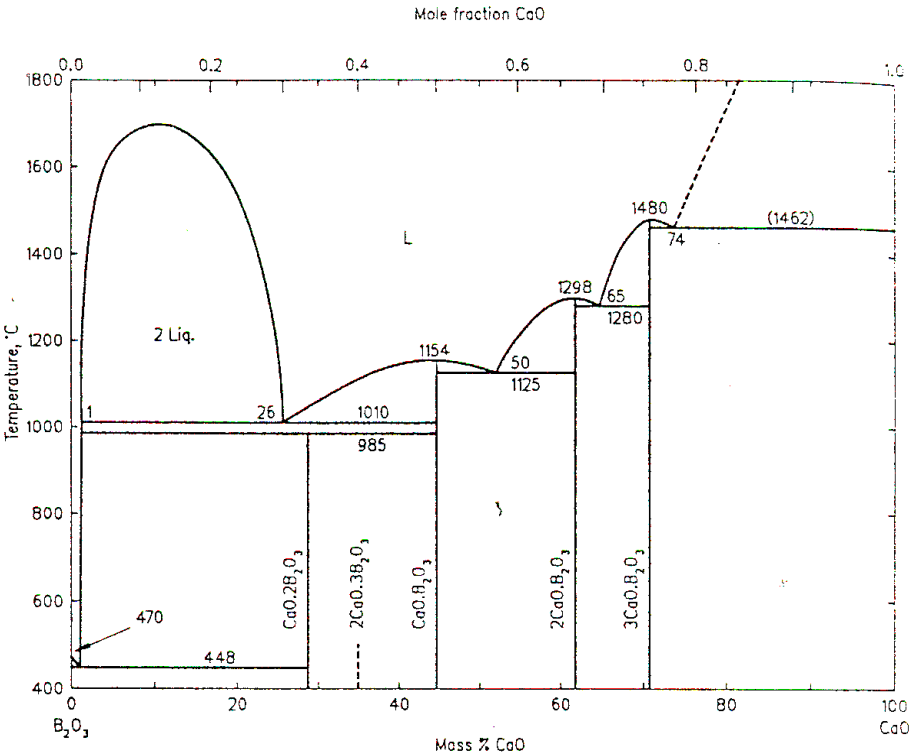

Figure 56. Phase diagram of the CaO-B_2O_3 system.

Table 12. Simulant material experimental data.

PROPERTY	Corium ($UO_2 - ZrO_2$) (80 – 20 Wt%)	$CaO - B_2O_3$ (30 – 70 Wt%)
Melting point (K)	2900	1300
Density (Kg/m^3)	8000	2500
Viscosity (Pa.s)	0.005	0.1 – 0.3
Thermal Conductivity (W/m/K)	10	3.0
Surface tension (N/m)	1.0	0.15
Specific heat (J/Kg/K)	540	2200
Fusion heat (KJ/Kg)	360	460

After much experimentation and analyses, conducted at the Nuclear Power Safety Division (Stolyarova, Green, 1997), the binary oxide (30% CaO-70% B_2O_3) was chosen for the COMECO experiment as the simulant representing the corium melt. Its phase diagram is shown in Figure 56 and its physical properties compared with those of corium (80% UO_2-20% ZrO_2) are shown in Table 12. The physical properties, for the purposes of the COMECO experiments, are quite similar; except for the viscosity, which is higher by about the factor of 10 for the CaO-B_2O_3 melt at temperature of about 100 K above the liquidus temperature (superheat).

5.5.3. Test section scaling

The dimensions of the COMECO test section were smaller than the dimensions of the corresponding unit cell of the prototypic BWR. Therefore a proper scaling relation had to be introduced in order to maintain the correct representation of the experiment setup, compared to the prototypic case. The scaling down of the CRGT model, employed in the COMECO test facility, was done by maintaining the same ratio:

Heat transfer area / Flow area = Const.

The area of the bypass openings was also reduced according the ratio:

Bypass area / Flow area = Const.

5.6. Results of the experiments

5.6.1. POMECO experiments

POMECO experiments with three different particulate debris bed configurations were performed. The effects of porosity and presence of CRGT on the dryout heat flux and the quenching rate had been measured.

5.6.1.1. Dryout experiments

The following dryout experiments were performed within each test series on dryout heat flux:

- With no water flow in the CRGT pipe;
- Water supply flow from the bottom to the CRGT pipe;
- Water flow through the open the upper holes (bypass) in the CRGT pipe, no water addition from the bottom;
- Water flow through the open upper annular part of CRGT, no water addition from the bottom.

In the first two test series (experiment with only top flooding) no dryout at the full power density of 0.98 MW/m^3 was observed (Tables 13 and 14).

In the tests DRC-1 this result is confirmed by the Lipinski model, which shows that for such bed configuration dryout can be expected at the power supply of about three times larger than that provided by the POMECO test section. Experiments with subcooled and saturated water in the CRGT showed similar results.

In the previous POMECO experiments (test series homo-2 described in Konovalikhin, et al, 2000) for the bed of the same configuration as in the test DRC-2 the measured dryout heat flux was 222 KW/m^2. This result is in good agreement with the prediction by Lipinski model (see Table 13). But during the DRC-2.1 experiment with the CRGT inside the bed no dryout was obtained (Table 14). This can be explained by the additional coolability capacity of the bed, provided by the CRGT. The heat removal rate through the CRGT was estimated as 15 kW, which, added to the Lipinski model value, could provide the estimation of 350 kW/m^2 as the dryout heat flux for such test conditions.

Table 13. Experimental conditions and results for the sand bed with porosity 0.4 and mean particle size 1.9 mm.

Test	Water flow rate in the CRGT, kg/s	Experimental dryout heat flux, kW/m^2	Dryout heat flux Lipinski model, kW/m^2	
			Without CRGT	With CRGT
DRC-1.1	-	>327	932	1061
DRC-1.2	0.0625 (10°C water)	>327	932	1077
DRC-1.3	0.0625 (85°C water)	>327	932	1094

Table 14. Experimental conditions and results for the sand bed with porosity 0.36 and mean particle size 1.0 mm

Test	Water flow rate in the CRGT, kg/s	Dryout heat flux, kW/m^2	Dryout heat flux Lipinski model, kW/m^2	
			Without CRGT	With CRGT
DRC-2.1	-	>327	226	350

In the third test series the bed with the similar mean particle size as in the previous DRC tests and low porosity of 0.26 was examined. The first experiment, DRC-3.1, showed (Table 15) that the presence of the CRGT increases the dryout heat flux significantly.

Earlier series of POMECO experiments conducted with similar particle bed composition had shown a good agreement between the experimental result and prediction by Lipinski model (Konovalikhin, et al, 2000).

From the comparison of these two experiments the additional cooling capacity provided by CRGT can be estimated as 10 kW for this bed configuration. It can be seen that addition of this value to the Lipinski model prediction gives a result, which is very close to the experimental.

Table 15. Experimental conditions and results for the sand bed with porosity 0.26 and mean particle size 0.8 mm.

Test	Water flow rate in the CRGT, kg/s	Dryout heat flux, kW/m^2	Dryout heat flux Lipinski model, kW/m^2	
			Without CRGT	With CRGT
DRC-3.1	-	133	51	132
DRC-3.2	0.0625 (85°C water)	154	51	154
DRC3.3	0.00625	166	51	170
DRC-3.4	Open upper holes	275	-	-
DRC-3.5	Open top part (cross section)	251	-	-

The tests DRC-3.2 and DRC-3.3 were conducted in order to investigate the enhancement of the dryout heat flux by the water flow in the CRGT. Two different flow rates were used: 0.0625 kg/s (prototypic) and 0.00625 kg/s of 85ºC water. As it can be seen in the Table 15, water flow enhances the dryout heat flux. In the test DRC-3.2 with flow rate of 0.0625 kg/s the additional heat removal is provided due to the heating of flowing water without vaporization. From the experimental data the heat flux to the water inside the CRGT estimated as 40-50 kW/m^2.

The comparison between experimental result of the test DRC-3.2 and Lipinski model gives good agreement (with consideration of heat removal through the CRGT

wall to the water overlayer and heating of water inside CRGT). In the test DRC-3.3 partial vaporization of coolant was registered, which explains higher dryout heat flux in comparison to that in the two previous experiments. To analyze this experiment by the Lipinski model steam generation rate in the CRGT was calculated employing the methodology described in (Konovalikhin, et al, 2000). The results of the comparisons are presented in the Table 15.

The objective of the test DRC-3.4 was to investigate dryout behavior in the situation, when saturated water can be delivered into CRGT pipe through the bypass flow openings in a BWR. For this purpose four holes, with total flow area equal to that in the BWR's bypass, were kept open during this test. As a result (see Table 15) a great enhancement in dryout heat flux was obtained. The improvement can be caused by intensive boiling inside the CRGT line, which resulted in significantly higher total steam discharge flow rate in comparison to the previous tests.

The test DRC-3.5 simulated the situation when the upper part of CRGT pipe is melted down and water could penetrate into the tube from the layer above. The total steam discharge was slightly lower in comparison to that in the test DRC-3.4 and, correspondingly, the experimental dryout heat flux was less (see Table 15).

It can be explained by the fact that during the test DRC-3.4 the steam release rates were recorded at the outlets of the CRGT pipe and water tank, but in the test DRC-3.5 only water tank steam discharge flow rate was measured, because the upper part of CRGT pipe was removed, and part of the steam discharged from the CRGT could be directly condensed during the passage through the water overlayer.

5.6.1.2. Dry bed cooling by water flow in CRGT

The experiment DRYFL was performed in order to obtain the heat removal rate from the dry bed by the water flow in the CRGT pipe without top flooding. The objective of this test was to measure heat extraction by water in the CRGT during cooling down of the bed from 450°C to 100°C.

Table 16. Experimental results of cooling test for homogeneous particle bed (porosity – 0.4, mean particle size – 1.9 mm); power supply – 4200 W; coolant t=85°C.

Test	Initial bed temperature, °C	Water flow rate in the CRGT, kg/s	Average steam discharge flow rate, kg/s	Quenching time, s
DRYFL	450	0.0625 (85°C water)	0.007	450

Experimental conditions and results of the test are presented in the Table 16. This test can be characterized by a relatively high CRGT heat removal rate, due to a partial vaporization of water (85ºC at inlet) during the passage through the CRGT pipe.

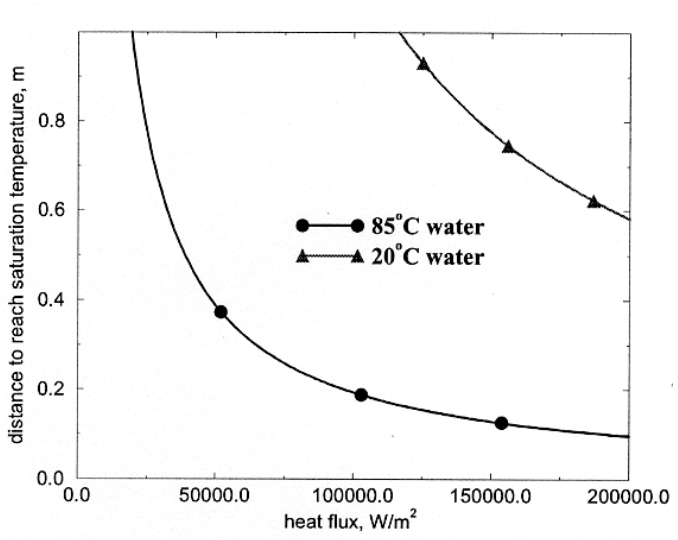

Figure 57. Calculated water saturation distances.

The heat flux was estimated to be 150 kW/m^2. As it can be seen from the Figure 57, calculations for the water saturation distance with experimental conditions presented above show that subcooled water cannot reach the saturation temperature. In other words, the dry bed with constant power supply of 4200 W and flow rate in CRGT of 0.0625 kg/s of 20ºC water would not be coolable.

5.6.1.3. Quenching experiments

Experimental results

Three series of experiments with different particle bed configurations to study the effects of porosity and the presence of CRGT on the quenching process of the dry bed have been carried out. Tables 17-19 with different experimental conditions. From the temperature histories at various locations in the particulate layer, the quenching time was determined by a rapid drop in the particle temperature (down to about the saturation temperature of water at the system pressure).

Table 17. Experimental results of quenching tests for homogeneous particle bed (porosity – 0.4, mean particle size – 1.9 mm); power supply – 4200 W; coolant temperature – 85ºC.

Test	Initial bed temperature, °C	Water flow rate in the CRGT, kg/s	Average steam discharge flow rate, kg/s	Quenching time, s
QC-1.1	500	-	0.014	240
QC-1.2	500	0.0625 (85°C water)	0.02	175

The water flow through the CRGT decreased the quenching times (Table 17 and Table 18) due to the additional heat removed by the flowing coolant. During the tests QC-2.2 and QC-2.3 two different coolant flow rates are compared: 0.0625 kg/s

(prototypic) and 0.00625 kg/s. During the test QC-2.3 with lower water flow more intensive water vaporization was registered, which caused the decrease in quenching time compared to the test QC-2.2.

Table 18. Experimental results of quenching tests for homogeneous particle bed (porosity – 0.36, mean particle size – 1.0 mm), power supply – 4200 W; coolant temperature – 85 ºC.

Test	Initial bed temperature, °C	Water flow rate in the CRGT, kg/s	Average steam discharge flow rate, kg/s	Quenching time, s
QC-2.1	450	-	0.009	210
QC-2.2	450	0.0625 (85°C water)	0.011	160
QC-2.3	450	0.00625 (85°C water)	0.013	140

Two main observations can be drawn from experimental results of QC-3 test series:

- the decrease in bed porosity resulted in a significant increase of quenching time;
- the presence of CRGT in the bed intensifies the quenching process.

In the tests QC-2 and QC-3 (see Table 18 and Table 19) the mean particle sizes were quite similar, but porosity value in the test series QC-3 was lower. It led to the slower water penetration through the bed due to a higher capillarity and lower steam generation rates (Table 19).

The test QC-3.4 was performed with open upper holes, which simulate the bypass openings in a BWR CRGT. Through these holes saturated water from the water overlayer could access the CRGT from above and provide intensive boiling and steam release inside the pipe.

Table 19. Experimental results of quenching tests for homogeneous particle bed (porosity – 0.26, mean particle size – 0.8 mm), power supply – 4200 W; coolant temperature – 85 ºC.

Test	Initial bed temperature, °C	Water flow rate in the CRGT, kg/s	Average steam discharge flow rate, kg/s	Quenching time, s
QC-3.1	450	-	0.003	1300
Qc-3.2	450	0.0625 (85°C water)	0.0035	1200
QC-3.3	450	0.00625 (85°C water)	0.004	1100
QC-3.4	~470	Open upper holes	0.007	1000
QC-3.5	450	Open upper cross section	0.005	950

The test QC-3.4 did not lead to a significant decrease in the quenching time because the initial bed temperature was higher in comparison to that in previous tests of the series QC-3. The last quenching experiment QC-3.5 with the open annular cross-section represented the situation with melted down upper part of CRGT. The test showed that the larger flow area provided more intensive water penetration into the CRGT, thus, providing more intensive heat transfer, which led to a decrease in the quenching time (Table 19) in comparison to that in the previous experiments of the test series QC-3.

5.6.2. COMECO experiments

One high temperature porous debris bed coolability experiment (HT-1) was carried out in the COMECO facility in order to assess the validity of the findings of the POMECO experiment to the higher temperature region (i.e. the porous debris bed coolability experiment was carried out at 1100°C vs. 450°C at the POMECO facility). A quenching test was carried out for the sand bed with the porosity of 0.4 and the mean particle size of 2 mm. The model for the quenching time prediction, derived for the POMECO experimental data was applied for the higher temperature experiment (see Section 5.5.1). The test confirmed the validity of the POMECO experimental findings (the prediction of the quenching time see section 5.5.1) for the higher temperature region.

Afterwards, three high-temperature melt pool coolability experiments were conducted at the COMECO facility for the melt pool with a CRGT inside. As the experiments were performed at temperatures of up to 1100°C, and the test section materials were subjected to a severe environment, attempts were made to complete the various phases in one experiment. Thus each experiment employed different CRGT flow rates, with different inlet temperatures and with/without the top quenching of the melt pool.

The first experiment (CT-1) in the series was performed with closed bypass openings at the top of the CRGT. The second experiment (CT-2) was planned to be performed with different flow rates and coolant temperatures in the CRGT (during this experiment the test section had failed and the melt had leaked, therefore the experimental data from this test are not reliable). The third experiment (CT-3) was performed with open bypass holes and with coolant flow through the CRGT.

5.6.2.1. Experiment CT-1

The first experiment series (CT-1) were performed with closed upper bypass holes in the CRGT. In the first phase of this experiment (Table 20), the coolant was supplied at ~11°C and at the flow rate of 62.5 g/s (nominal flow rate in the reference BWR). During the next phase of the test the flow rate through the CRGT was reduced to 6.25 g/s. As the feed water was highly subcooled, only its partial evaporation occurred during its passage through the CRGT during the Phase I of this experiment. Reduction of the coolant flow rate led to a greater evaporation in the CRGT but the overall heat removal rate was reduced, due to the significantly lower coolant mass flow rate during

the Phase II and due to the fact, that the melt pool temperatures were lower during the Phase II, compared to the Phase I.

Table 20. Experiment CT-1.

Phase	Flow rate in CRGT, g/s	T_{water} in CRGT, °C	Top flooding	Time on DAS, s
I	62.5	11	NO	112
II	6.25	11	NO	590
	Flow stopped			700
III	6.25	95	YES	3200

During the Phase III of this experiment, the CRGT feed water temperature was raised to 95°C (at a flow rate of 6.25 g/s). At the same time, water was supplied to the top of the melt pool (the water temperature was 95°C).

The heat removal rate from the CRGT and from the upper tank, for the three phases of the experiment CT-1 were based on the steam flow rates obtained by the steam flow meters. The total heat removed was estimated as the sum of the heat, required to heat up the water to the saturation temperature and the latent heat of vaporization.

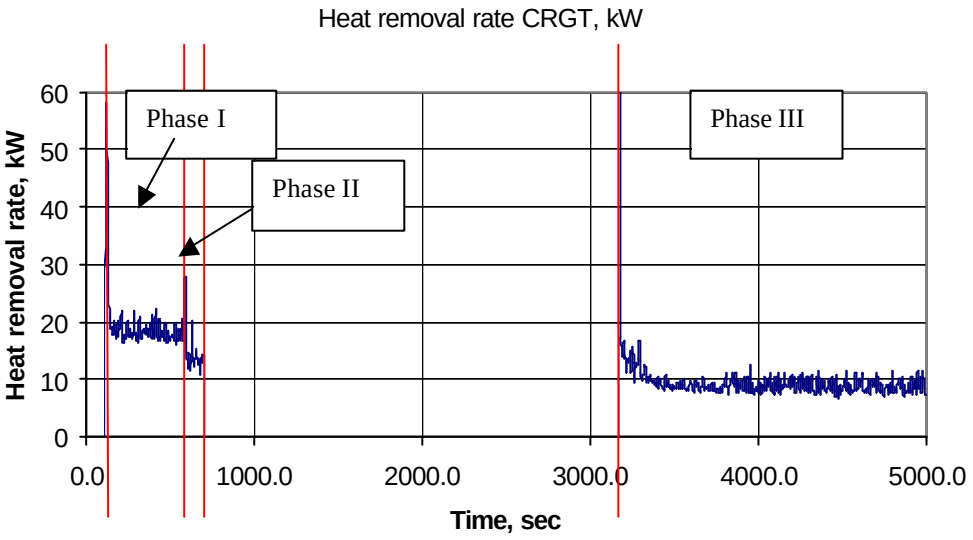

Figure 58. Heat removed through CRGT during the experiment CT-1.

As seen on the Figure 58, the reduction of the flow rate through the CRGT from 62.5 g/s to 6.25 g/s (Phase I-II) led to a decrease of the heat removal rate (from 18 kW removed through the CRGT at 62.5 g/s flow rate to 11 kW at 6.25 g/s). During Phases I and II highly subcooled liquid (11°C) was supplied to the test section, therefore, the evaporation rate was low for these phases of the experiment. During the Phase III slightly lower heat removal rates through CRGT were registered (Figure 58), even though the feed water temperature was close to saturation and much greater evaporation rates were expected. But the additional top flooding during the Phase III

(Figure 58) decreased the average melt pool temperature, therefore decreasing the overall heat transfer coefficient to the CRGT. For the Phase III the amount of heat removed through the CRGT was about 10 kW (at the coolant flow rate of 6.25 g/s through the CRGT).

High heat removal rates (up to 80 kW) from the upper tank were recorded at the beginning of the quenching process. However, due to the rapid crust formation at the upper layer of the melt pool, the heat transfer rate to the water in the tank decreased exponentially and stabilized at about 18 kW for the later stages of the experiment.

Table 21 . Summary of the experiment CT-1.

Phase	Flow rate in CRGT, g/s	T_{water} in CRGT, °C	Top flooding	Heat removed through CRGT, kW	Heat removed by top quenching, kW	Total amount of heat removed, kW	Average heat transfer coefficient at CRGT wall , kW/m²
I	62.5	11	NO	18.0	-	18.0	382
II	6.25	11	NO	11.0	-	11.0	233
III	6.25	95	YES	10.0	83÷18	93÷28	212

During the COMECO experiments, full quench of the melt pool was not achieved. This supports the findings of other experimental programs (e.g. MACE program carried out at the Argonne National Laboratory), during which the full quenching of the pool was also not achieved due to the formation of an impermeable crust on the top of the melt pool.

The results of the experiment CT-1 are summarized in the Table 21. From the results it may be concluded that the maximal heat removal rate from the test section was about 80 kW (at the early phases of the process). After the crust at the top of the melt pool was formed, about 18 kW of heat were removed from the test section by the top quenching (heat transfer through the crust). The maximal heat removal capacity of the CRGT was 18 kW.

5.6.2.2. Experiment CT-2

The second experiment series (CT-2) were planned to be carried out with the closed bypass openings and with various coolant flow rates and temperatures in the CRGT. Unfortunately, the experiment was not completed, as the test section developed a leak and all the melt was lost to surroundings.

5.6.2.3. Experiment CT-3

The third experiment series (CT-3) were conducted with open upper CRGT bypass. This experiment consisted of 5 phases. Figure 59 shows the steam flow rates from CRGT and tank during the experiment.

Table 22. Summary of the experiment CT-3.

Phase	Flow rate in CRGT, g/s	T_{water} in CRGT, °C	Top flooding	Time on DAS, s
I	62.5	12	NO	280
End of Ph. I				880
II	6.25	12	NO	3980
End of Ph. II				4570
III	62.5	95	NO	7480
End of Ph. III				8100
IV	6.25	95	NO	12880
V	6.25	95	YES	13480

After the each of the phases I, II and III, the test section was reheated to high temperatures and the experiment continued. In the first phase of this experiment (Table 22), the coolant was supplied at ~12°C and at the flow rate of 62.5 g/s (nominal flow rate in the reference BWR). As the bypass holes were open above the melt pool, part of coolant was supplied to the upper tank of the COMECO facility on the top of the melt pool through these openings. This generated additional steam flow from the tank and provided additional coolability capacity for the melt pool.

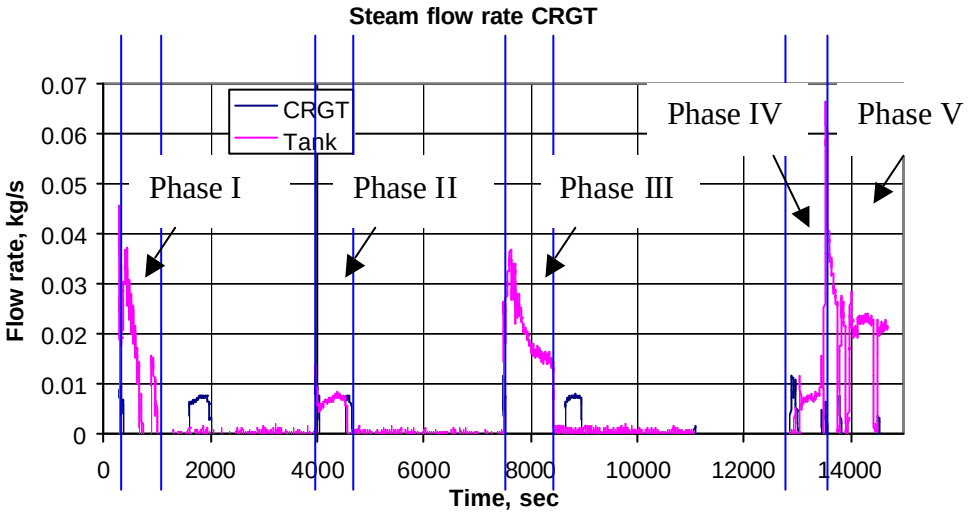

Figure 59. Steam flow rates during experiment CT-3.

In the second phase of the experiment the flow rate through the CRGT was reduced to about 6.25 g/s. During the third phase the coolant at t=95ºC and flow rate of 62.5 g/s was supplied to the CRGT. In the Phase IV the coolant flow rate was reduced to ~6.25 g/s. In the Phase V additional water was supplied to the upper tank and melt pool quenching (with additional flow of the water through CRGT) was investigated.

Phase I

The average heat removal rate from the CRGT during the Phase I was about 18 kW during the first 100 seconds. The steam generation within the tank had a peak value of 120 kW (during the film boiling) during the first seconds of the experiments. Later on, as the upper layers of the melt pool cooled down and the crust was formed, the heat removal rate was reducing gradually.

However, after the water flow in the CRGT was stopped at t=880 sec, the water layer above the melt pool in the upper tank began to heat up. The water reached the saturation and the heat removal rate from the tank (Figure 59) reached the values of about 40 kW at t=900 sec.

Phase II

The melt pool was reheated to high temperatures, and the second phase of the experiment started. During this phase water at t=12ºC and flow rate of 6.25 g/s was supplied to the CRGT. The heat removal rate from the CRGT was about 20 kW for the Phase II of the experiment CT-3. The heat removal from the tank was also close to 20 kW.

Phase III

During this phase water at t=95ºC and flow rate of 62.5 g/s was supplied to the CRGT. The coolant flow in CRGT was stopped at about 8100 seconds.

As the water temperature in the CRGT was close to the saturation during this Phase, the heat removal from the melt pool did not decrease sharply after the initial peak during the first seconds. This was due to the fact, that for this Phase a rapid reheat of the coolant to saturation prevented from a time delay, during which the steam generation rates are low (warming up of the coolant in the tank). The average amount of heat removed through the CRGT was about 16 kW.

Phases IV and V

During the final two phases of the experiment CT-3, the coolant at 95°C temperature and 6.25 g/s flow rate was supplied through the CRGT. During the Phase V the additional coolant (at the temperature of 95°C) was supplied to the upper tank of COMECO test facility, on the top of the melt pool. Quenching experiment was carried out.

During the Phase IV the heat removal rate through the CRGT was about 20 kW. Similar heat removal rate through the CRGT was registered during the Phase V (top flooding of the melt pool). The stabilized heat removal rate from the tank was close to 50 kW, with a peak of 150 kW at the first moments after the additional water was supplied into the upper tank. During this experiment, similar to the test CT-1, a peak value of the heat transfer coefficient is noted at the beginning of the process. Afterwards, the heat transfer rate dropped significantly as the crust formed on the top

of the melt pool. Initial peak was due to the direct contact heat transfer between melt and water. The experiment CT-3 is summarized in the Table 23.

Table 23. Summary of the experiment CT-3.

Phase	Flow rate in CRGT, g/s	T_{water} in CRGT, °C	Top flooding	Heat removed through CRGT, kW	Heat removed by top quenching, kW	Total amount of heat removed, kW	Average heat transfer coefficient at CRGT wall , kW/m²
I	62.5	12	NO	18	120-40	138-58	382
II	6.25	12	NO	20	20	40	424
III	62.5	95	NO	16	80-35	96-51	340
IV	6.25	95	NO	20	19	39	424
V	6.25	95	YES	18	150-50	168-68	382

From the results of this experiment it can be concluded, that the maximum heat removal rate from the test section was up to 170 kW (at the early phases of the top quenching process). After the crust at the top of the melt pool is formed, about 20 kW of heat were removed through the CRGT from the test section by flow through the CRGT and additional 20-50 kW by the top quenching (heat transfer through the crust). The maximum heat removal capacity of the CRGT was 20 kW.

5.7. Analytical models

5.7.1. POMECO experiments

A simple zero-dimensional integral analysis has been performed based on consideration of hydrodynamic flooding due to the steam formation. The basic assumptions were that the water penetrates the debris bed at a constant velocity, which is uniform across the bed, and the steam is generated immediately after the contact of water with the solid particles. In addition, it was assumed that the hot particles are completely quenched and cooled to water saturation temperature as the water penetrates through the debris bed. The quenching rate of the bed is directly proportional to the penetration rate. The following relation for the quenching time can be written:

$$\Delta t = \frac{r_{sol} C_{p,sol} (1-e) V (T_{sol} - T_{sat})}{(G_w H_{fg} + W_{CRGT}) - W} \qquad (38)$$

Here, heat removal rate through CRGT W_{CRGT} consists of heat removed through CRGT structure (wall) to the water overlayer, heat to heat up the coolant inside the CRGT ($G_{w,CRGT}\Delta T$) and the latent heat of vaporization ($G_{w,CRGT}H_{fg}$). The numerator in this ratio is responsible for the total heat, which has to be removed in order to quench the bed and the lower term is the cooling down (quench) rate.

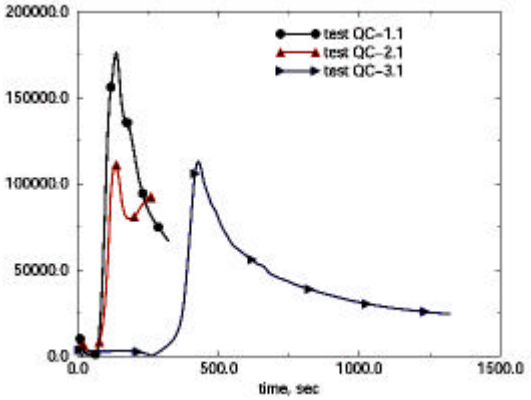

Figure 60. Inversely predicted surface heat flux in quenching experiments QC-1.1, QC-2.1 and QC-3.1.

The CONTA code was employed to estimate heat removal rate through the CRGT structure. The results of the calculations are presented on the Figure 60. For the given experimental conditions the heat fluxes in the CRGT wall are between 100 KW/m^2 and 170 KW/m^2. Higher heat flux in the QC-1.1 test is due to the higher initial bed temperature.

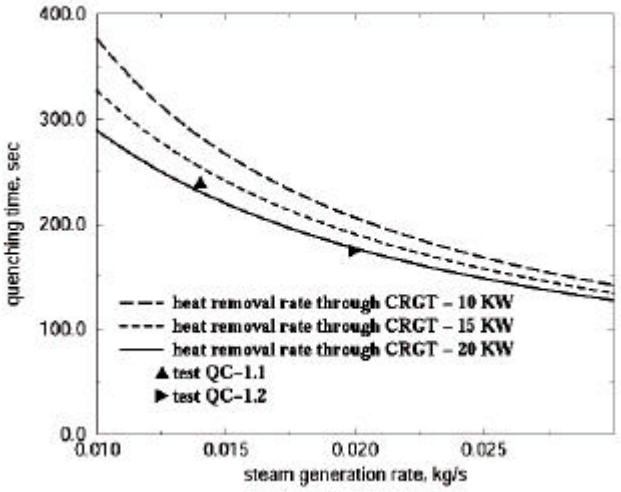

Figure 61. Comparison between experimental and calculated results of QC-1 test series.

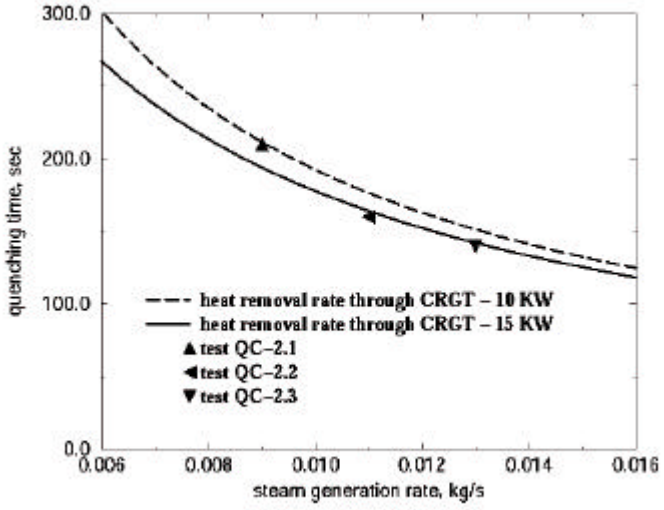

Figure 62. Comparison between experimental and calculated results of QC-2 test series.

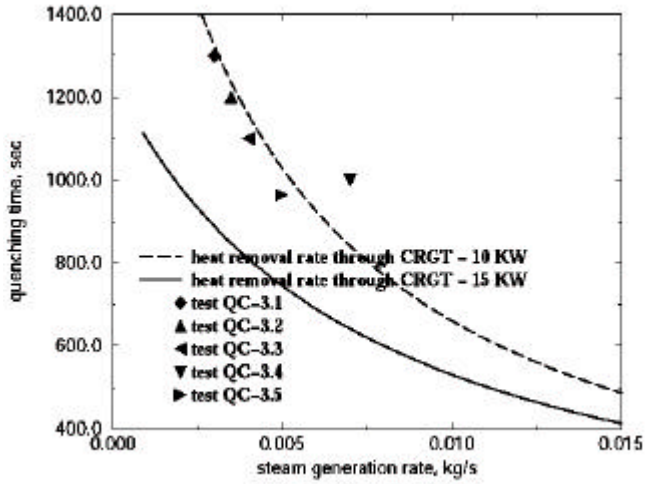

Figure 63. Comparison between experimental and calculated results of QC-3 test series.

Using the values predicted by the CONTA calculations all the quenching experiments performed in the POMECO test series were analyzed. The results of the analysis are depicted on the Figure 61 and Figure 62. As it can be seen from these Figures the experimental results of the first test series agree best with the calculations with average heat removal rate through CRGT structure taken as 20 kW; for the second test series - between 10 and 15 kW and for the last test series - 10 kW.

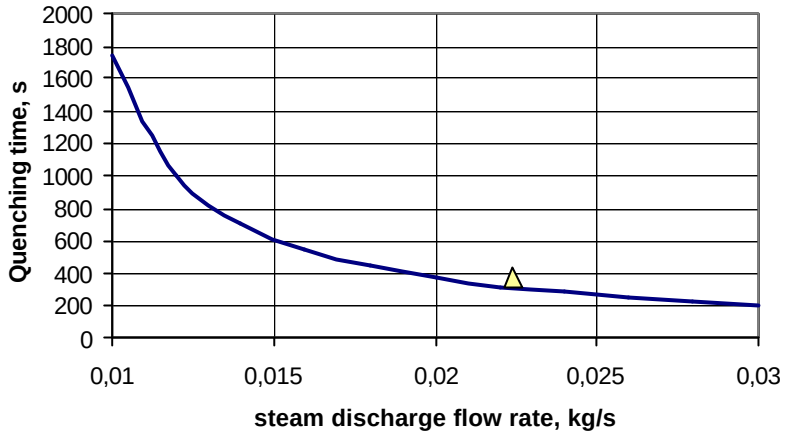

Figure 64. Comparison between experimental and calculated results for test HT-1.

The Eq. (38) was applied to predict the quenching time for the high temperature debris bed test (Experiment HT-1, carried out at COMECO facility for the particle bed of porosity 0.4 and mean particle size 2 mm). The model proved to be as well valid for the higher temperature of the debris bed region (Figure 64).

5.7.2. COMECO experiments

5.7.2.1. Prediction of the quenching time

Assuming that melt cooling and quenching occurs due to water ingression, a zero-dimensional integral analysis has been performed, based on the consideration of a balance between the heat content of the melt and heat removal from the melt pool by water. The following relation for the cooling time can be written:

$$\Delta t = \frac{(r_m V_m (C_{p,m} \Delta T_m + H_{fus,m}) + W)\frac{d}{H}\Delta t}{q_{CRGT} p d_{crgt} d + q_{out} S} \tag{39}$$

where Δt is the cooling down time, ρ_m is the melt density, V_m is the melt bed volume, W is the power supply, q_{CRGT} is the heat flux from melt pool to CRGT wall, d_{CRGT} is the outer diameter of the CRGT, δ is the crust thickness, q_{out} is the heat flux from crust to overlaying water and S is the crust-water interacting area, H is the initial depth of the melt pool. The numerator in the ratio is responsible for the total heat, which should be removed in order to solidify the bed, and the lower term shows the cooling rate. The equation could be rewritten as:

$$\Delta t = \frac{(r_m V_m (C_{p,m} \Delta T_m + H_{fus,m}))\frac{d}{H}}{(q_{CRGT} p d_{CRGT} d + q_{out} S) - W\frac{d}{H}} \tag{40}$$

As only partial quenching of the melt pool was reached during the experiment, the equation above was applied to estimate the partial quenching times for the experiment CT-1 and the first four phases of the experiment CT-3. The calculation results are presented in the Table 24. Calculated quenching time, presented in this table was estimated using Equation 40.

Table 24. Comparison of experimental and calculated quenching times.

Experiment	Experimental water ingression depth, cm	Experimental partial quench time, sec	Calculated quench time, sec	Calculated quench time with no CRGT, sec
CT-1, Phase 3	2.5	105	114	120
CT-3, Phase 1	2.5	99	106	122
	5.0	258	235	259
	10.0	438	436	597
CT-3, Phase 2	2.5	54	51	54
	5.0	138	116	135
	10.0	194	254	366
CT-3, Phase 3	2.5	64	77	80
	5.0	101	100	110
	10.0	159	216	268
CT-3, Phase 4 and Phase 5	2.5	67	88	96
	5.0	99	171	190
	10.0	182	181	248
	15.0	251	251	426

Calculated quench times with no CRGT were estimated by removing the term for the heat removed through the CRGT wall in Eq. 40. These are shown in Table 24. There is a substantial increase in the calculated quench times, which indicates the significant contribution of the heat removal through CRGT to the water ingression melt quenching process. In this case the predicted quenching times become longer, compared to the measured values. The difference between the quenching time increases with the growth rate of the crust layer.

As it is seen from the Table 24, a reasonable prediction of the quenching times was obtained for all the phases of the experiments. For the later phases of the experiment CT-3, the calculations predict later occurrence of the quenching compared to the recorded experimental results. The reason for this are the lower temperatures in the upper part of the melt pool during the later phases of the experiment, as the melt pool was reheated after each phase. The reheating of the melt between different phases of the experiment CT-3 did not always result in completely uniform temperatures in the melt pool. At the end of each phase, the upper part of the melt pool solidified while the bottom parts of the pool were more or less in liquid state. After the reheating the upper parts of the melt pool could not reach temperatures of melt liquidus and above. Thus, there may be some hysterisis in the phase 3 and of the experiment CT-3 i.e., the ingression passages used by water in the earlier phase may still be available for water to ingress. The water ingression depth reached in Phase IV was higher than in Phase III and the time to reach ingression depth of 10 cm in Phase III was less than that in Phase II.

5.7.2.2. Film boiling

Film boiling commences as soon as the coolant layer is established on the top of the melt pool, which is terminated when the surface temperature decreases below the minimum film boiling temperature.

During the early phases of the coolability process the surface temperature of the melt pool is above that required for film boiling of water so that a vapor film separates the melt surface from the water.

This initial phase of the melt pool-water interactions could be investigated applying the classical Berenson equation for zero-gas flux film boiling (Berenson, 1961):

$$q_{out} = \frac{k(T_m - T_{sat})}{d_{Ber}} + h_{rad}(T_m - T_{sat}) \quad (41)$$

where k is the thermal conductivity of vapor, T_{sat} is the water saturation temperature, δ_{Ber} is the vapor film thickness and h_{rad} is the radiation heat transfer coefficient.

The radiation heat transfer coefficient is obtained from the following equation:

$$h_{rad} = e\, s_{SB}(T_m^2 + T_{sat}^2)(T_m + T_{sat}) \quad (42)$$

The Berenson (1961) equation for the vapour film thickness:

$$d_{Ber} = 2.35\left(\frac{n_v k_v (T_{sol,m} - T_{sat})}{h_{fg} g(r_w - r_v)} \cdot \left(\frac{s_w}{g(r_w - r_v)}\right)^{0.5}\right)^{0.25} \quad (43)$$

where ν_v is vapor kinematic viscosity, k_v is the vapor thermal conductivity, $T_{sol,m}$ is the melt solidus temperature, ρ_v is the vapor density and σ_w is the water surface tension.

The Equation 41 was applied while assessing the maximum heat flux during the film boiling (Experiment CT-1 Phase 3). As the flowmeter, installed on the steam line from upper tank at COMECO facility was designed to record the maximum steam flow rates of up to 30 l/min, the actual peak value of the steam flow during the initial phase of the test CT-1 was not recorded, as it was above the tolerance limits of the flowmeter. Therefore, this value was calculated using the equation described above (Figure 65).

As it is seen from the Figure 65, the calculated maximum heat removal value for the film boiling was about 120 kW, which corresponds to q"=3.156 MW/m^2. This is much greater than the recorded rate; however, it agrees quite well with the measured value for the Phase V of the test CT-3 in which water was added to the top surface of the melt pool and the steam flow was measured with the higher capacity flow meter.

The heat transfer rate at the top surface of the melt decreased rapidly due to the reduction of the temperature of the surface of the melt pool and the formation of the crust on the top of the melt pool.

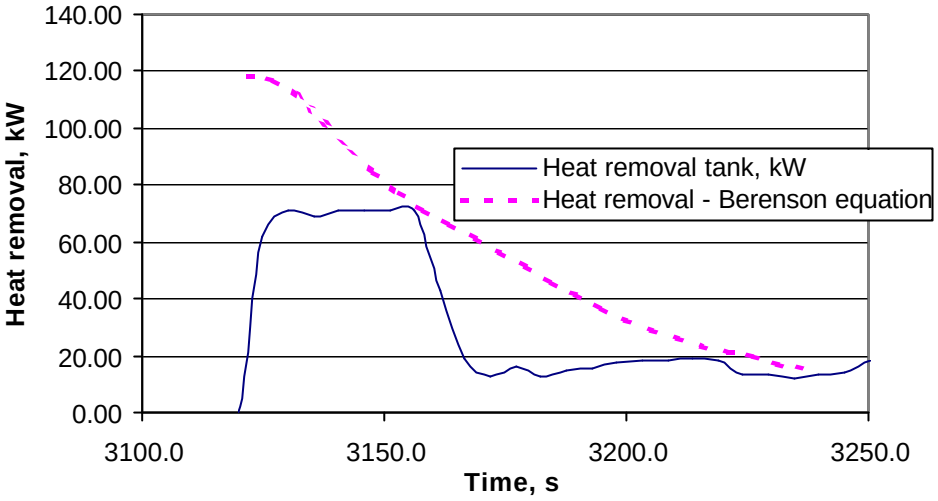

Figure 65. Comparison of experimental data and predicted values for the bulk cooling phase.

The maximum value for the film boiling heat transfer was close to 150 kW for the experiment CT-3, Phase V, corresponding to q"=3.945 MW/m^2.

5.7.2.3. Crust growth

For the prediction of the crust growth rate the model developed by Farmer (2001) was modified and used for the analysis of COMECO experiments. In this model, the particular form of the boundary condition at the crust upper surface depends upon whether the porous particle bed is present or not above the crust upper surface (Farmer, 2001).

For the cases, when the melt pool is dry (no water is present), the crust growth and cooling down of the melt pool is governed by the radiation heat transfer. For the cases in which the particle bed is absent and the crust is impervious to water ingression, the assumption of the uniform physical properties and heat distribution is used and the growth rate from the original Farmer's equation is expressed as:

$$r_c \Delta e_{ls} \frac{dd}{dt} = k_c \frac{(T_f - T_I)}{d} - \frac{X^c_{UO_2} r_c q_{dec} d}{2} - h_m (T_m - T_f) + h_{rad} (T_f - T_I) \qquad (44)$$

where ρ_c is the crust theoretical density, Δe_{ls} is the latent heat of fusion, δ is the crust thickness, T_I is the crust/coolant interface temperature, which is evaluated from a suitable energy balance depending of whether water is present or not above the

crust, $X^{c}_{UO_2}$ is the weight fraction of fuel in crust, q_{dec} is the decay heat. Third term on the right hand side of the Equation 44 defines the melt -side convective heat transfer.

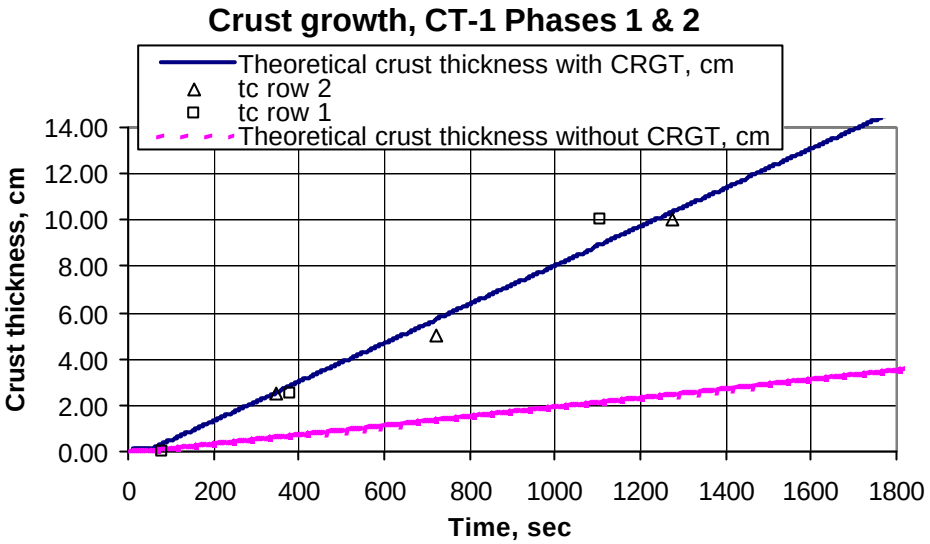

Figure 66. Crust growth during Phases I and II of the experiment CT-1.

In the case of the COMECO experiment analysis, the decay heat was simulated by the external heating of the melt pool and the crust. Also, there was no convection on the melt side in the test section. The heat transfer from melt to the crust was only due to the crust conduction. Therefore, the Equation 44 for the COMECO experiments can be reformulated as:

$$r_c \Delta e_{ls} \frac{dd}{dt} = k_c \frac{(T_f - T_I)}{d} - \frac{q_c}{2} + q_{CRGT} + h_{rad}(T_f - T_I) \qquad (45)$$

in this case q_c is the heat generation in crust and q_{CRGT} is the additional heat removal from the crust, provided by the presence of CRGT.

The results of the average crust growth rate, calculated using Equation 45 for the Phases I and II of the experiment CT-1 are presented on the Figure 66. During the first two phases of the experiment there was no water layer above the melt pool and, therefore, the melt was cooled under the dry cavity conditions.

As it is seen from the Figure 66, the experimental data (thermocouples in the rows 1 and 2) are in good agreement with the predictions of the Farmer model for the crust growth in the dry conditions. The crust growth rate for the conditions when the CRGT is not present (i.e. no last term in the Eq. (45)) is also plotted on the Figure 66. In this case the crust growth rate for the dry cavity would be significantly lower. The crust thickness of 10 cm for the case with no CRGT would be reached only at t=5088 sec, according the present model (vs. about 1200 sec when having a flow inside the CRGT).

5.7.2.4. Water ingression

For the case, when the crust is treated as permeable, the onset of the water ingression occurs when the total heat flux from the crust falls below the corresponding dryout heat flux for the upper surface of the melt pool (Farmer, 2001):

$$q''_{d,c} - r_v h_{l,v} j_{nc} \mid_{T_{sat}} \geq k_c \frac{(T_f - T_I)}{d} + \frac{X^c_{UO2} r_c q_{dec} d}{2} \qquad (46)$$

here j_{nc} is the CCI non-condensable gas interfacial velocity.

After the onset of water ingression, the crust growth is governed by the following equation:

$$r_c \Delta e_{sat} \frac{dd}{dt} = q''_{d,c} - X^c_{UO2} r_c dq_{dec} - r_v h_{lv} j_{nc} \mid_{T_{sat}} - h_m (T_m - T_f) \qquad (47)$$

where Δe_{sat} is the change in melt specific enthalpy during quench to saturation temperature, h_{lv} is the convective heat transfer coefficient.

Since there was no non-condensable gas injection during the series of the COMECO experiments, presented here, the Equation 47 can be rewritten, also taking into account the additional heat removal, offered by the CRGT:

$$r_c \Delta e_{sat} \frac{dd}{dt} = q''_{d,c} - q_c + q_{CRGT} \qquad (48)$$

Integration of Equation 48 and the experimental data obtained during the water ingression period in the experiment CT-1, can be employed to estimate average values of the dryout heat flux as a function of time or d, the quenching depth (or crust thickness). Figure 67 shows the measured values of the crust thickness (as derived from the thermocouple data). The water was added to the melt pool at 3200 seconds, the upper 10 cm of the melt pool were quenched in 600-700 seconds. The next 5 cm of water ingression took much longer and the crust depth of 15 cm was reached at ~6500 seconds, i.e. ~3300 seconds after water flooding.

Employing Eq.(48) along with the measured values for the heat addition q_c and the heat removal through CRGT, i.e. q_{CRGT}, the average values obtained for the dryout heat flux are 220 kW/m^2 for the crust depth of 15 cm. There was no quenching observed for the thermocouple at 20 cm depth before the experiment was terminated.

A conceptual variation of the dry-out heat flux versus the crust thickness is shown in Figure 68. The curve drawn is intuitive and is simply based on the observations of the water ingression rate in the experimental CT-1. It is anchored at ~1 MW/m^2 for the value of the dryout heat flux at the initiation of crust formation, since that is the value for a flat plate.

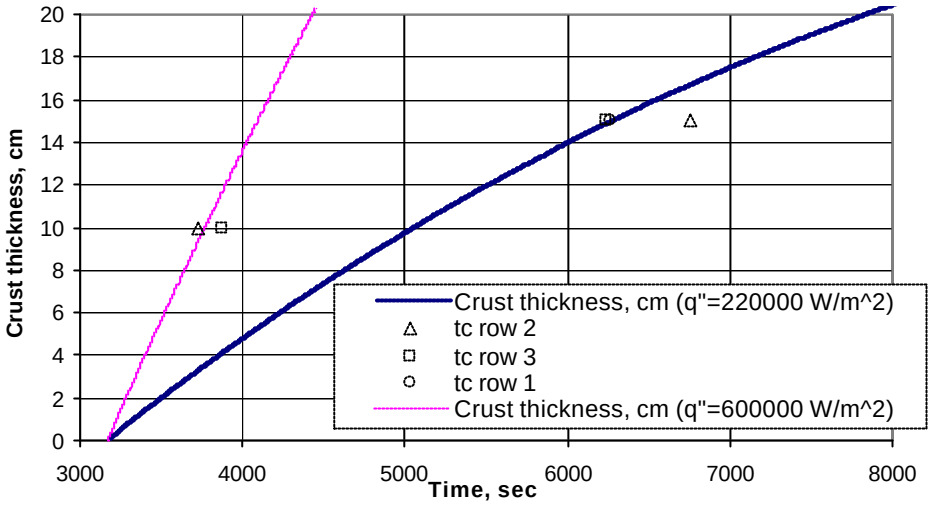

Figure 67. Comparison of CT-1 Phase III experiment data and crust growth rate, calculated using Farmer's model.

The observation of the decrease in the water ingression rate with the crust depth are not peculiar to the experiment CT-1. The water ingression data in the MACE test MIB (Farmer et al2001) although not explicitly reported also showed that it took much longer for water to ingress in the deeper regions of the melt pool than it did in the top portion of the melt pool. In fact, it is observed both in the MACE test MIB and the tests FOREVER-5 and –6 (Sehgal et al 2003) that the water ingression takes place up to a certain time and to a certain depth of the melt pool and then it stops. This may be interpreted as a decrease in the dryout heat flux with the depth of the water ingression. Perhaps, the material cracking and the inter-connected porosity formation that occurs in a molten material due to cooling by water is a function of the depth of the cracked structure formed. It should be noted here that the cracked structure that is formed in a melt pool is far from conventional porous particulate debris of uniform porosity everywhere.

It is quite conceivable that the water ingression behavior is a function of material properties of the melt (Farmer, 2003), e.g. the temperature difference between the liquidus and the solidus, the heat of fusion, the coefficient of expansion, the material strength, etc. (Lister, 1974). Further experiments to provide guidance to development of a model and for its subsequent validation are advised and will be undertaken at the Nuclear Power Safety Division of KTH.

Assuming the behavior of the dryout heat flux as shown in Figure 68 the crust thickness (or quenched depth) as a function of time was calculated for the Phase III of the test CT-1. Employing Eq. 48, with and without the CRGT, the crust depth is calculated as a function of time. Figure 69 shows the results of the calculations.

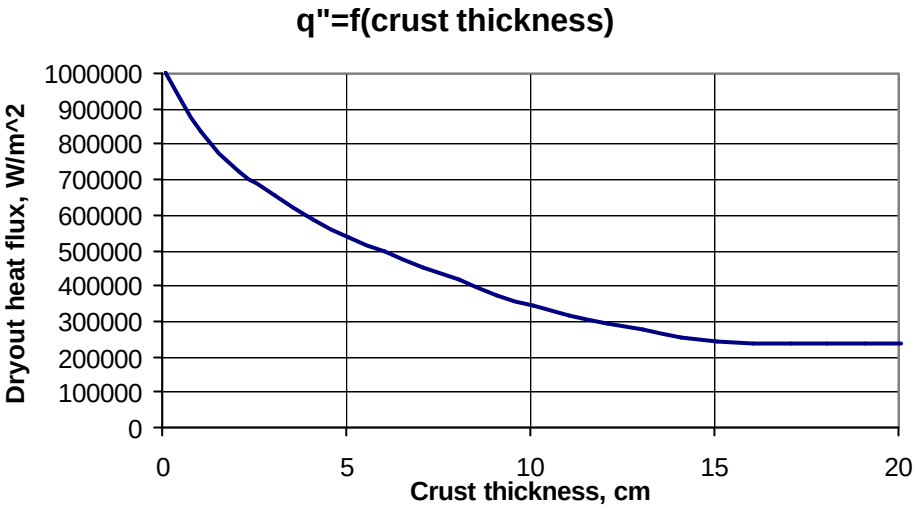

Figure 68. Assumed dryout heat flux during CT-1 Phase III.

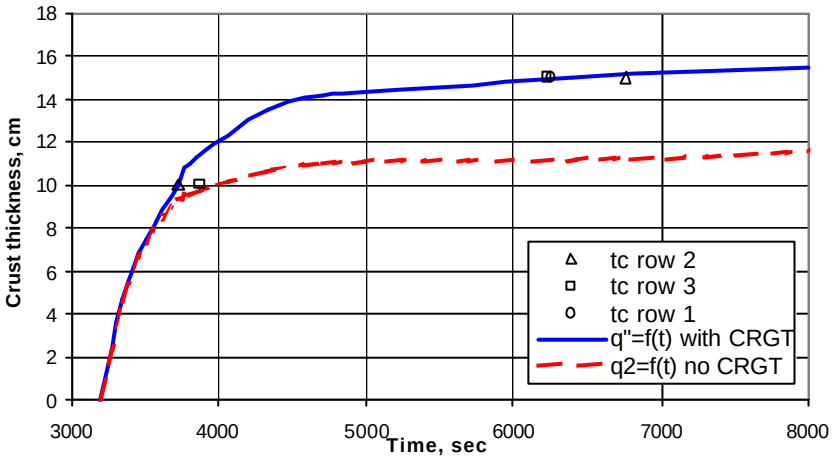

Figure 69. Calculated crust thickness during CT-1 Phase III.

As it is seen from the Figure 69, at the beginning of the quenching process there is no significant difference between the crust growth rates for configurations with/without the CRGT in the melt pool. At the beginning of the process the dryout heat flux (first term on the RHS of Eg. (48)) is much greater than the heat removal rate through the CRGT. During the later stages of the process, however, the dryout heat flux reduces significantly, thereby limiting the total heat removal rate from the melt pool. In these later stages the additional heat removal through the CRGT provides a significant contribution to the overall crust growth (Figure 69).

5.8. Major findings and accomplishments

A series of experimental investigations on the coolability of the particulate debris bed and melt pool coolability were performed out. Two test facilities: POMECO and

COMECO were constructed and scaled experiments with the prototype test set-up were performed.

The POMECO experiments have shown that the presence of the control rod guide tubes offers a significant additional cooling capacity for the particulate debris bed, since both the dryout heat flux and the quenching rate are enhanced. Heat removal rate through CRGT structure was found to be 10-15 kW depending on the surrounding porous medium characteristics and the temperature regime. Water flow rates in the CRGT result in additional increase of the dryout heat flux and of quenching rate.

Lipinski model with addition of CRGT heat removal rate was employed to analyze the POMECO dryout experiments. Reasonable agreement between the experimental and calculated results was obtained.

Characteristic times for quenching were computed by the model, which combines parameters of the process (V, p_{over}, T_{sol}, T_w, W), geometry (A_{bed}, d_{dwnc}) and physical properties (H_{fg}, $C_{p,w}$, ρ_w, μ_w, $C_{p,sol}$, ρ_{sol}, ε). Good agreement between experimental and calculated results has been achieved for the POMECO experiments and for the high temperature particle debris bed experiment performed in the COMECO facility.

Two successful experiments with a unit cell of a melt pool in the lower head of a BWR containing a tube representing a CRGT were performed on the COMECO facility. Each experiment consisted of several phases, during which the temperature and flow rate of the water inlet to the CRGT were varied. The experiments were performed with open and closed bypass holes at the upper part of the CRGT.

Quenching experiments were also performed by establishing a water layer on top surface of the melt pool. Full quench of the 30 cm deep melt pool was not achieved during the experiments. The thickness of the permeable crust on the top of the molten pool was 5-15 cm. The experimental results show that an average of about 20 kW of additional heat can be removed from the test section through one CRGT surrounded by a melt pool, which corresponds to a heat removal flux of ~ 350 kW/m^2 for the 30 cm heated height of the CRGT; however, with a crust formed on the surface of the CRGT the heat removal capacity decreases. We believe that with the surface area offered by all the CRGTs in the lower head of a BWR, it may be possible to remove much of the decay heat generated in a corium melt pool, deposited in the lower head of a BWR.

The analysis of the experimental results was performed for 3 phases of the quenching process. The zero-dimensional model derived from the heat balance of the test section provides a good prediction for the quenching times, recorded during the COMECO experiment. It shows that the critical heat flux decreases as the water ingression depth increases and that the importance of the heat removal capacity offered by the CRGTs increases with increasing crust thickness. The bulk cooling resulted in high heat fluxes during the first moments of the experiments. Later on the heat flux from the top surface of the melt decreased substantially as the crust growth took place.

The COMECO experiment has shown that additional heat flux of 200-400 kW/m^2 could be established though the CRGT, which indicates a large potential for the heat removal from the BWR lower head through the CRGTs during a severe accident. This heat removal process through the CRGT also increases the crust growth rate during the later stages of the melt pool quenching process for both dry and wet conditions.

Chapter 6

Porous medium coolability

6.1. Objectives

The aim of the work was to investigate the ex-vessel debris coolability and the CCFL limitations during the corium-concrete interaction (CCI) process for a particulate debris bed. For this purpose the POMECO test facility was modified, adding the air inlet at the bottom of the test section. The airflow through the test section simulated the non-condensable gas generation during the CCI. The coolability of particulate debris beds of different porosities was investigated. The comparison of the experimental data obtained was rationalized with the available CCFL correlations.

6.2. Introduction and background

Ex-vessel melt (debris) coolability is a critical safety issue for the current and future LWR plants, with respect to the management and termination of a postulated severe (core melt) accident. In such cases, after the vessel failure, the core melt (debris) attacks the concrete basemat, whose ablation can be terminated only by cooling the melt (debris) to below the concrete dissolution temperature (Sehgal et al, 1999).

A particulate debris bed can be generated in the cavity of a PWR or, in the dry well of a BWR if water is present. If no more water is available the existing water will evaporate in time, resulting in a dry heat generating particulate debris bed, which would start attacking the basemat concrete. It is most opportune to cool the debris bed in its particulate state before it melts and becomes a melt pool.

The most convenient accident management measure is to cool the particulate debris by establishing a water layer on its top. The concrete ablation process induces the release of gases from the concrete, which could limit the quenching of the debris bed.

The scenario investigated here is that of the quenching of a hot particulate debris bed with the gas release from the bottom of the debris bed. The gas (air) supply system was installed in the POMECO facility below the debris bed. The gas flow rates through the debris bed corresponded to the gas release rates at the late stages of

CCI (several hours after beginning of the process) from both basaltic and limestone-common sand concretes. Series of quenching experiments (adding the coolant from the top of the debris bed) were carried out at various gas flow rates. The dependence of the quenching time of the debris bed on the gas addition rates was investigated.

6.3. Experimental Facility

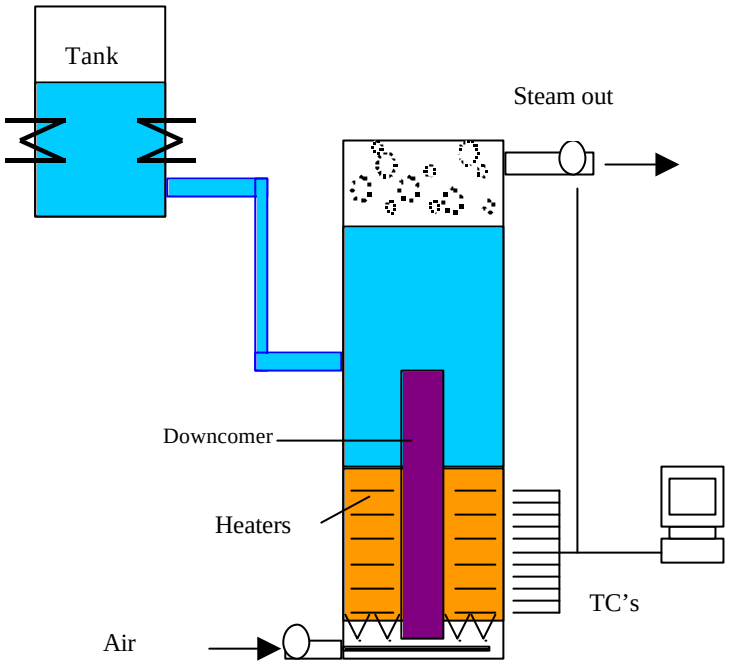

Figure 70. POMECO test facility.

The schematic of the POMECO (POrous MEdia COolability) facility, designed and constructed at the Nuclear Power Safety Division of the Royal Institute of Technology, was described in the previous Chapter and is shown on the Figure 70. Test section is 350×350 mm square (500 mm high). The modification of the POMECO facility consists of installing an air supply system below the test section. The porous debris bed was assembled from sand. The porosity and mean particle sizes of the sand were varied. The sand bed was supported from bottom by a stainless steel net. Another stainless steel net covered the top surface of the bed to prevent the flying-off of the sand particles. Air, supplied from the bottom of the test section, passed through the stainless steel net and penetrated the sand bed.

Pressurized air was supplied at the bottom of the test facility. The maximum capacity of the air was up to ~190 l/min (3.15 l/sec). A flowmeter was installed at the air-line to measure the amount of air supplied.

A water tank was connected to the upper part of the POMECO facility. The tank supplied water to the top of the debris bed. The feedwater from the tank was heated up to a required temperature (~90ºC for the tests, described in this Chapter).

6.3.1. Test section and instrumentation

The test section was a stainless steel vessel whose details are presented in Figure 71 (picture b). The cross-sectional area of the test section is 350×350 mm. The height of the lower (heated) part was 500 mm and the height of the upper part is 900 mm. The maximum height of 370 mm could be achieved for the sand bed in the lower part of the test section.

The POMECO facility contained an annular pipe (outside diameter ∅124 mm) in the center of the sand bed. The annular pipe was of the same dimensions as the Control Rod Guide Tube (CRGT) in the BWR lower head. This test section configuration was the same as in the previously described POMECO experiments.

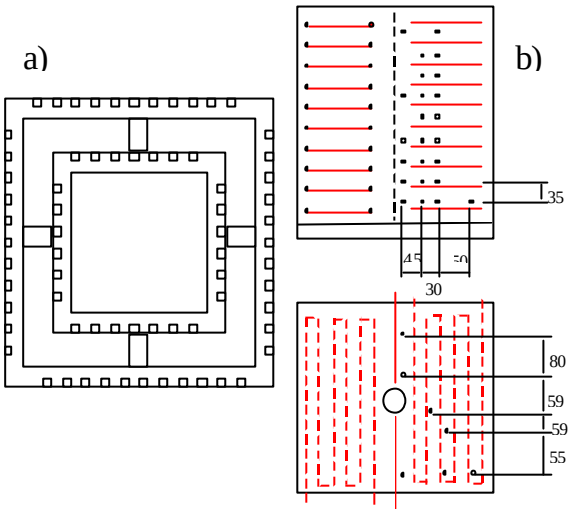

Figure 71. POMECO test section design, heater and thermocouple distribution.

Picture a) on the Figure 71 presents the design of the air supply grid, installed at the bottom of the POMECO test section. The air was distributed into two rectangular passage lines with openings on the sides of the lines. This allowed for more mixing and more homogeneous air distribution before air entered the sand bed.

As in the previous POMECO test series (see Chapter 5), thirty-three thermocouples are distributed at different positions in the particle bed as shown in Picture b) in the Figure 71. The thermocouples were located at 11 axial elevations and at 5 radial positions. The quenching occurrences during the test series were recorded according the readings of those thermocouples.

6.3.2. Experimental procedure

These POMECO experiments represent the later stages of the CCI process (i.e. several hours after the onset of CCI). During the CCI interactions in the later phases of the transient, the concrete ablation rate was assumed to be equal to 5 cm/hour (i.e., corium continues to penetrate the concrete at this velocity). The heat generation in the debris bed of the POMECO facility was equal to 0.1 MW/m^3. This heat generation rate is equal to about 10% of the estimated decay heat rate for corium mixture.

Table 25. Chemical composition of Default Concretes (values in $^{w}/_{o}$).

Species	Basaltic Aggregate Concrete	Limestone Aggregate-Common Sand Concrete	CRBR Concrete
SiO_2	54.84	35.8	3.60
TiO_2	1.05	0.18	0.12
MnO	0.00	0.03	0.01
MgO	6.16	0.48	5.67
CaO	8.82	31.30	45.40
Na_2O	1.80	0.082	0.078
K_2O	5.39	1.22	0.68
Fe_2O_3	6.26	1.44	1.20
Al_2O_3	8.32	3.60	1.60
Cr_2O_3	0.00	0.014	0.004
CO_2	**1.50**	**21.154**	**35.698**
H_2O evap	**3.86**	**2.70**	**3.94**
H_2O bound	2.00	2.00	2.00

The series of quenching experiments were carried out. First the sand in the test section was heated up to about 500°C. After the sand bed in the test section reached this temperature, airflow from the bottom of the test section was established.

The flow rate of the air through the test section was calculated according to the amount of gas, which is contained, and released, from various default concrete types. The material content of some types of concretes, used in the reactor technology, is presented in the Table 25. The gaseous components are typed in bold in the Table 25. As it is seen, the main contributors for the gas release in the concrete are carbon dioxide (CO_2) and water vapor (H_2O). It was assumed that gases, contained in the concrete, are fully released during the CCI scenario, investigated at the POMECO test facility.

As it is seen from the Table 25, the amount of the gases contained in the concrete differs with various concrete types. During the experiments, gas amounts, corresponding to the gas release rates from two widely used concrete types: basaltic and limestone concretes, were chosen to be simulated. Airflow at the flow rate, which corresponds to the amounts of the gas released, was supplied at the bottom of the POMECO test facility. Initial air temperature at the entrance to the test section was equal to the room temperature (about 20°C). The air heated up to the porous bed temperature (about 450÷500°C) after traveling about 8 cm through the porous bed.

After establishing the airflow through the porous debris bed, the water (at the temperature of about 90°C) was supplied to the top of the debris bed. Quenching experiments were carried out, in order to determine the debris bed quenching time at various airflow rates.

Two configurations of the porous beds were used during the experiments: with porosities ε=0.38 and 0.26 and corresponding mean particle sizes of 1.0 and 0.7 mm.

6.4. Experimental results

Four different experimental conditions were investigated:

- No airflow through the test section. Quenching experiments were carried out in order to determine the reference quenching time for the different bed configurations;
- Experiments with low airflow rate. These conditions correspond to the CCI with low gas content concrete (gas generation in basaltic concrete);
- High airflow rate experiments, which correspond to the CCI with high gas content concrete (gas generation in limestone concrete);
- Experiments with varying airflow rate, which were carried out in order to determine the corresponding CCFL onset airflow rate in the porous debris bed.

6.4.1. Debris bed of porosity 0.26

Table 26 presents the experimental results for the quenching tests in the first test series, with low porosity debris bed (the porosity of 0.26 and the mean particle sizes of 0.7 mm). The power supply to the test section was 4200 W (about 0.1 MW/m^3). Initial average sand bed temperature was about 450°C. The highest temperatures (over 500°C) were in the middle plane of the test section (about 20 cm deep in the debris bed). The temperatures at the top and the bottom of the debris bed were lower, due to the heat losses to the environment. The temperatures at the locations of the lowest and highest thermocouples, embedded in the test section were about 430-450°C.

Test LP-1.1, presented in Table 26, was carried out with no airflow through the debris bed. For this porous bed composition, the full quenching of the debris bed in the test section occurred at about 2400 seconds after the filling of the upper tank with water. Average steam generation rate was about 0.003 kg/s, which corresponds to about 6.5 kW heat removal rate from the debris bed by the top flooding (the power input during the test series was 4.2 kW).

Table 26. Quenching experiments for the low porosity debris bed. (Porosity – 0.26, mean particle size 0.7 mm; power supply 4200 W, initial mean sand bed temperature 450°C).

Test No.	Air flow rate through the debris bed, l/min	Average steam discharge rate, kg/s	Quenching time, s
LP-1.1	-	~0.003	2400
LP-1.2	30.0	~0.002	5100
LP-1.3	142.5	0.0	No quenching
LP-1.4	Stepwise reduction to ~93 l/min	variable	Initiation of quenching

During the test LP-1.2 the airflow at the rate of 30 l/min was supplied to the test section. This additional airflow significantly increased the quenching time for the debris bed (5100 sec vs. 2400 sec with no airflow).

During the test LP-1.3 the gas flow rate, which corresponds to the gas generation rate in the limestone sand concrete (several hours after the onset of CCI, when concrete ablates at the rate of about 5cm/hour) was supplied through the test section. At this gas flow rate, the counter current flooding limit (CCFL) was exceeded, and no water was able to penetrate the debris bed of the porosity 0.26.

Test LP-1.4 was carried out in order to determine the gas flow rate, at which the CCFL is reached. For this test, the initial gas flow at the rate of 142.5 l/min was established. After this, the gas flow rate was reduced in steps of 10 liters/every 10 minutes, until the quenching of the debris bed was initiated. After the start of the quenching process, the gas flow rate was not changed during the rest of the experiment. It was determined, that for the porosity of 0.26 and the mean particle size of 0.7 mm the CCFL is reached at the flow rate of about 93 l/min.

6.4.2. Debris bed of porosity 0.38

The second series of experiments was carried out with the debris bed of porosity 0.38 and mean particle sizes of about 1.00 mm. The results of the experiments are presented in Table 27. As it is seen, the CCFL for the higher porosity debris bed configuration was reached at the air flowrate of about 160 l/min. This flowrate exceeds the gas generation rate from the investigated types of concrete, when the corium is ingressing at 5 cm/hour.

Table 27. Quenching experiments for the higher porosity debris bed. (Porosity – 0.38, mean particle size 1.00 mm; power supply 4200 W, initial mean sand bed temperature 450°C).

Test No.	Air flow rate through the debris bed, l/min	Average steam discharge rate, kg/s	Quenching time, s
HP-1.1	-	~0.003	1680
HP-1.2	30.0	~0.002	1740
HP-1.3	142.5		2220
HP-1.4	Stepwise reduction to ~160 l/min	variable	Initiation of quenching

During the test HP-1.1 no additional airflow was supplied into the test section. The quenching time (Table 27) for the debris bed was 1680 sec, i.e. the debris bed was quenched in a shorter time, compared to the first experimental series (Table 26), due to higher porosity of the debris bed, which results in larger flow area and smaller influence of the capillarity effects, compared to the porosity of 0.26 (during the first test series).

Test HP-1.2 was carried out with 30 l/min air flow rate (which corresponds to the gas generation rate in a basaltic concrete). The quenching time in this test was longer, compared to test HP-1.1.

At the high gas flow rates of 142.5 l/min (test HP-1.3) the quenching of the debris bed occurred about 540 sec later, compared to the reference case.

The onset of the CCFL for the high porosity debris bed composition was investigated during the experiment HP-1.4. The test started with the high air flowrate (about 180 l/min) established through the test section. The airflow rate was reduced in steps of 10 liters/every 10 minutes, until the quenching of the debris bed started. The initiation of quenching of the debris bed started. The initiation of quenching of the debris bed was recorded at the air flowrate of 160 l/min.

6.5. Analysis

Dell and Pratt (1951) found, that for immiscible fluids the flooding velocities can be correlated as:

$$j_1^{1/2} + j_2^{1/2} = C \tag{49}$$

where the constant C is a function of particle diameter, bed porosity, surface area and phase densities (1 and 2 represent two phases or fluids). Later on, the C value was found to be affected also by changes in viscosity and surface tension of the two phases (Marshall and Dhir, 1983).

For the flooding limit of the gas flow moving upward and the liquid flux downward, Wallis (1969) had proposed an empirical flooding correlation of the form:

$$j_g^{*1/2} + m\, j_f^{*1/2} = C \tag{50}$$

Where m and C are the constants and j_k^* are the dimensionless superficial velocities, defined as:

$$j_k^* = j_k \left[\frac{r_k}{gD(r_l - r_g)\dfrac{e^3}{a}} \right]^{1/2} \tag{51}$$

Marshall and Dhir (1983) defined the parameter *a*, surface area packing per unit volume of the column, as:

$$a = \frac{6(1-e)}{D_p} \tag{52}$$

For a bed with top flooding, several correlations were developed on this basis. Correlations, presented by Wallis (1969), Marshall & Dhir (1983) perform quite well for high gas flow rate:

$$j_g^{*1/2} + j_l^{*1/2} = 0.775 \quad \text{Wallis} \tag{53}$$

$$j_g^{*1/2} + j_f^{*1/2} = 0.875 \quad \text{Marshall\&Dhir} \tag{54}$$

For the low flow region a correlation, developed by Schrock at al (1984) can be applied:

$$j_g^{*0.38} + 0.95\, j_f^{*0.38} = 1.075 \qquad (55)$$

Dimensionless superficial velocities j_k^* were calculated and plotted for the POMECO experimental data (Figure 72).

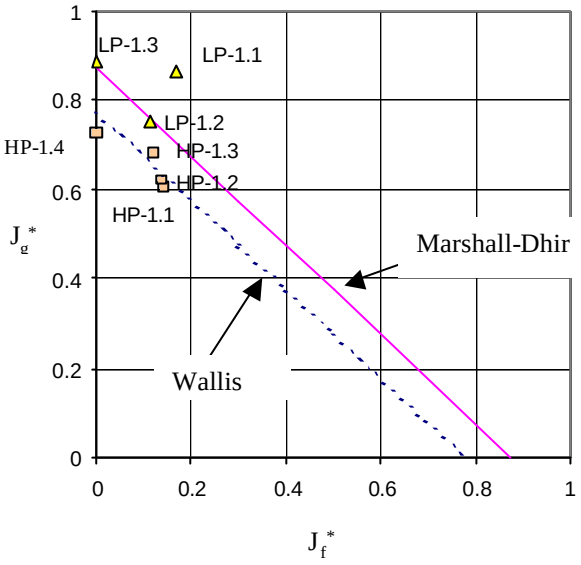

Figure 72. Comparison of the experimental data with flooding correlations.

As it is seen from the Figure 72, Marshall and Dhir correlation provides good estimate for the flooding for the experiments LP-1.2 and LP-1.3. Both flooding limit and dimensionless superficial velocities for this case agree well with the experimental data. During both experiments LP-1.2 and LP-1.3 additional gas flow through the test section was present.

For the case with no additional gas flow (experiment LP-1.1) the experimental data does not fit the correlation predictions. I.e. either gas or liquid phase superficial velocities were higher during the experiment, compared to the correlations. The better agreement for this case (LP-1.3) is obtained using the Schrock et al correlation for the flooding limit prediction. In this case we obtain the constant C~1.1 (see right hand side of the equation (55)), instead C=1.075, predicted by the Schrock et al correlation.

On the other hand, the experimental data, obtained during the experiments with high porosity (ε=0.38) particle beds (experimental series HP-1, 2, 3 and 4) provide lower values of the constant C, compared to the previous experimental case, with the porosity of ε=0.26. Gas and liquid superficial velocities for the experimental series HP agree best with the Wallis correlation (Equation 53) estimation (Figure 72).

6.6. Major findings and accomplishments

Series of experiments, simulating the ex-vessel particulate debris beds on the POMECO facility were carried out. Additional airflow was supplied through the test section in order to simulate the CCI scenario, with gas generation from the concrete structures. The concrete ablation and associated gas generation rates were estimated equal to the ablation velocity at the later stages of the CCI transient (about 5 cm/hour of the concrete ablation). The experiments were aimed at the investigations of the coolability of the various types of debris beds under the conditions, when additional gas is supplied through the debris bed.

Two debris bed configurations were investigated: of porosities 0.26 (mean particle size 0.7 mm) and 0.38 (mean particle size 1.0 mm). During the experiments it was determined that:

- The addition of the gas at the bottom of the porous bed significantly increases the quenching time for the low porosity small mean particle size beds;

- Flooding limitation might be reached for the low porosity beds at high air flow rates at the gas generation rates, comparable to the gas content in the common types of concrete, i.e. the penetration of coolant into the particle bed may be impossible;

- For higher porosity bed composition (ε=0.38; mean particle size 1 mm) the addition of the gas from the bottom does cause an increase in the bed quenching time but the CCFL is reached for this bed configuration at substantially higher gas flow rates.

A comparison of the experimental results with the empirical flooding correlations, developed by Wallis (1969), Marshall & Dhir (1983) and Schrock et al (1984) shows the good agreement for the flooding limitation prediction. For the low porosity bed compositions (ε=0.26), for the experimental with additional air supply through the test section. Experiment LP-1.1, performed with no air supply and resulted in higher, as compared to Wallis and Marshall & Dhir correlation, liquid/gas superficial velocities. For this case, the closest agreement was obtained with Schrock et al, correlation predictions, although the experimental superficial velocities were still higher, compared to the correlation predictions.

For the high porosity debris bed compositions (ε=0.38), the experimental liquid/gas superficial velocities were lower than predicted by the Marshall-Dhir correlation. The close agreement with Wallis correlation was obtained for these test series (experiments HP-1.1, 2, 3 and 4).

Chapter 7

CONCLUSSIONS

This Thesis describes the work, carried out by the author at the Nuclear Power Safety Division, KTH. The research performed could be divided into two areas: RBMK-1500 core analysis methodology development and the experimental investigation of postulated severe accidents in the LWRs. The aim of the work was: first – to develop, validate and verify an independent RBMK-1500 core analysis methodology for the reactor core kinetics and thermal hydraulic analyses and second – to carry out experimental investigations of the postulated in- and ex-vessel severe accident scenarios in a LWR.

In the first parts of this Thesis, the RBMK-1500 core analysis was presented. A new RBMK-1500 core analysis independent methodology based on and Western codes was developed. The RBMK-1500 neutron cross-section database was generated using the HELIOS code. The HELIOS calculations were benchmarked with WIMS-D4 code. The WIMS-D4 cross section library developed in Russia and used in the STEPAN code calculations was employed for the benchmarking purposes.

Sufficiently close agreement was found between the HELIOS and WIMS-D4 calculation results. In addition, the HELIOS cross section library was validated through 3-D neutron kinetics calculations using CORETRAN code. The validation was performed by comparison against the experimental data of the RBMK Experimental Critical Facility at RRC Kurchatov Institute.

The thermal hydraulics subchannel analysis code VIPRE-02, which is a part of the CORETRAN package was supplemented with additional Critical Heat Flux (CHF) correlations, applicable to the RBMK-1500 reactor analysis. Three additional CHF correlations were implemented into the VIPRE-02: Osmachkin correlation for the lower fuel assemblies of the RBMK-1500, RRC KI correlation for the upper RBMK-1500 fuel assemblies and Khabenski correlation for the low coolant mass flux region.

The VIPRE-02 code was validated against the experimental data for CHF and post-CHF heat transfer in long (approx. 7 m) tubes and fuel bundles. Data from 3 experimental test series were used for the validation: KTH and EREC E-108 experiments on heated single tubes and RRC KI experiments on CHF in the RBMK fuel bundles. The VIPRE-02 calculations were benchmarked with RELAP5/MOD3.3 code. The additional CHF correlations provide good agreement with the experimental results for the RBMK parameter range. The use of Osmachkin correlation resulted in

good agreement with the experimental data only for single channel models. For the subchannel models of VIPRE-02 the Osmachkin correlation provides an overprediction of the CHF. In addition, two of the standard VIPRE-02 CHF correlations: EPRI and Bowring, also provided good CHF prediction for pressures of about 7 MPa. Maximum wall temperatures during the transition and film boiling regimes for the p=7 MPa were predicted correctly with VIPRE-02. For higher pressures (12-20 MPa) the maximum wall temperature during the transition boiling was underpredicted with VIPRE-02.

The CORETRAN model for the RBMK-1500 core analysis was developed and verified against the Ignalina NPP RBMK-1500 reactor data. The CORETRAN code provides good predictions for axial and radial power distribution within the RBMK-1500 core, voiding effect, fast power coefficient, Xenon transient, control rod worths, etc. The CORETRAN calculations were performed with HELIOS and WIMS-D4 generated sets of neutron macroscopic cross section data. The benchmarking with STEPAN code calculations was carried out.

The developed CORETRAN model for RBMK-1500 was employed for a series of RIA and ATWS analyses. Results of some transient calculations are presented in this Thesis. The model proved to be fully functional and may be employed in various areas of RBMK-1500 safety analysis.

The severe accidents in the LWR's were investigated in the second part of the Thesis. The in-vessel scenario in a BWR and the additional corium coolability potential offered by the presence of the control rod guide tubes (CRGTs) in the lower head of a BWR was investigated experimentally and analytically. Two experimental facilities were modified: POMECO and COMECO. Particulate debris bed coolability and dryout heat flux measurement experiments were carried out on the POMECO facility. The test facility incorporated a full-size unit-cell model of a prototypic CRGT. Various flow modes and scenarios were investigated. The experimental results show that, depending on the debris bed configuration, additional 10-20 kW of heat could be removed from the POMECO test section due to the presence of CRGT. The dryout heat flux may be up to 3 times of that obtained in a low porosity debris bed where no CRGT was employed. The presence of CRGT also significantly enhanced the quenching times of the particulate debris bed. The 0-D model for the quenching time prediction in a particulate debris bed was assessed.

Melt pool coolability enhancement experiments performed in the COMECO facility showed that the CRGT with a water flow could remove 10 to kW of heat from the melt pool, which corresponded $\underline{\sim}$200 to 400 kW/m^2 heat flux. This heat removal also facilitates the water ingression into the melt, thus an increase in the thickness of the quenched depth of the melt pool when the melt pool is flooded with water from the top.

The rate of water ingression into the melt pool in the COMECO facility was measured and it was found that the water ingression rate decreases with the depth of the quenched region. This was interpreted as a decrease in the dryout heat flux with the water ingression depth in the melt. It is believed that the cracking and porosity

creation that occurs in a molten material due to the cooling by water is a function of the depth of the cracked structure formed. This conclusion, derived from experimental observation is supported by the observation in the MACE H1-B test and in the FOREVER-5 and –6 tests (Sehgal et al, 2004) where it is observed that the water ingression proceeds to a certain depth and effectively stops. It is quite conceivable that the water ingression behavior is also a function of material properties (Farmer-2003), e.g. the ΔT between liquidus and solidus, the heat of fusion, the coefficient of expansion, the material strength (Lister, 1974) and the heat generation rate in the melt. The experiment CT-1, performed in the COMECO facility shows, similar to the other melt coolability experiments, that the potential for coolability may be enhanced if other means of removing heat from the melt pool can be devised.

Experimental investigations on the ex-vessel coolability scenario with the non-condensable gas flow through the particulate debris bed was carried out on POMECO facility. High and low porosity debris debs were investigated. It was found that for low porosity beds, having the non-condensable gas release rate similar to that, which could be expected during the corium concrete interaction process for the limestone aggregate-common sand concrete, the counter current flooding limit (CCFL) for the particle bed may be exceeded, thus limiting the quenching of the debris bed. The CCFL for the particulate debris bed could be predicted using Wallis and Marshall-Dhir CCFL correlations. For larger porosity particulate debris bed (= 0.38), the CCFL condition is not exceeded for the anticipated gas release rates. Thus the CCFL in a heat generating particulate bed was found to be a strong function of the bed porosity.

Bibliography

[1] Accident Analysis for Nuclear Power Plants, IAEA Safety Report Series, No. 23, International Atomic Energy Agency, Vienna, 2002.

[2] Adamov, E. O., Grozdov, I. I:, Petrov, A. A., Cherkasov, Yu. M., Burlakov, E. V., Kramerov, A. Yu., Status and prospects for pressure-tube water-cooled graphite-moderated reactors, *Nuclear Engineering and Design*, Vol. 173, pp. 59-66, 1997.

[3] Alexeev, N., Behrens, D., Davydova, G., Donderer, R., von Ehrenstein, D., Krayushkin, A., Meyer, S., Shumacher, O., The Monte Carlo codes MCNP and MCU for RBMK criticality calculations, Nuclear Engineering and Design 183 (1998) 287-302.

[4] Almenas, K., Kaliatka, A., Uspuras, E., Ignalina RBMK-1500. A Source Book. Ignalina Safety Analysis Group, Lithuanian Energy Insitute, Kaunas, Lithuania (1998).

[5] Alsmeyer, H., Spencer, B., and Tromm, W., The COMET Concept for Cooling of Ex-Vessel Corium Melts, Proceedings of ICONE-6 conference, San Diego, USA, 1998.

[6] Alsmeyer, H., Review on Experiments on Dry Corium Concrete Interactions in: Molten Corium/Concrete Interaction and Corium Coolability – A State of the Art Report – Directorate – General XII Science, Research and Development, EUR 16649EN.

[7] Babaytsev, M.N., et.al., The STEPAN code for RBMK Reactor Calculations, RCC KI, IAE-5660/5 (1993) (In Russian).

[8] Baek, W.-P., Chang, H. C., An independent assessment of Groenevald et al's 1995 CHF look-up table. *Nuclear Engineering and Design* 178, pp. 331-337, 1997.

[9] Balunov, B. F., Ilukhin, Yu. N., Smirnow, E. L., Heat transfer crisis in channels with blocked lower end. *High Temp. Thermophys.* 25 (1), 116-124, 1987.

[10] Barchevtsev, V., Artisyuk, V., Ninokata, H., Concept of erbium doped uranium oxide fuel cycle in light water reactors, *Journal of Nuclear Science and Technology*, Vol., 39, No. 5, pp. 506-513, May 2002.

[11] Barleon, L, Thomauske, K., Werle, H., *Extended dryout and rewetting of small-particle core debris*, 6th International meeting on Debris Coolability, Los Angeles, Ca, November7-9, 1984.

[12] Bechaud, C., Duval, F., Fishot, F., Quintard, M., Parent, M., Debris Bed Coolability Using 3-D Two-Phase Model in a POrous Medium, Proceedigns of ICONE-9 conference, Nice, France, April 8-12, 2001.

[13] Beck, J.V., Blacwell, B. and Clair, Ch. "Inverse Heat Conduction III-Posed Problems", Walay-Interscience, 1985.

[14] Becker, K., Hermborg, G., Development and description of a novel method for accurate measurements of fluid flow rates, AE-RPL-102, 1961.

[15] Becker, K. M., et al, Round tube burnout data for flow of boiling water at pressure between 30 and 200 bar. KTH-NEL-14, 1971.

[16] Becker, K.M:, Ling, C.H., Hedberg, S. and Strand, G. An experimental investigation of post dryout heat transfer. Royal Institute of Technology, KTH-NEL-33, 1983.

[17] Becker, K. M., Söderquist, B., Assessment of round tube CHF tables. KTH-NEL-55, June 1992.

[18] Bell, G. I., Glasstone, S., Nuclear Reactor Theory, Van Nostrand Reinhold Co., N. Y., 1970.

[19] Bestion, D., Geffraye, G., The CATHARE code, DTP/SMTH/LMDS/EM/2001-063, Grenoble, France, April 2002.

[20] Blose, R. E., et. Al., Sustained Heated Metalic Melt/Concrete Interactions with Overlaying Water Pools, NUREG/CR-4747, SAND85-1546 R3, R4, R7, July, 1987.

[21] Blose, R.E., et. Al., Core-Concrete Interactions with Overlaying Water Pools – the WECTOR 1 test, NUREG/CR-5907, November, 1993.

[22] Bobkov, V. P., Kirillov, P. L., Smogalev, I. P., Vinogradov, V. N., Look-up tables developing methods for critical heat flux in rod bundles. *Proceedings of the NURETH-8 conference*, 1997.

[23] Bowring, R. W., A new mixed flow cluster dryout correlation for pressures in the range 0.6 to 15.5 MN/m^2 (90 to 2250 psia) -- for use in a transient blowdown code. I. Mech. Engr., 1977.

[24] Bowring, R.W., WSC-2: A subchannel dryout correlation for water-cooled clusters over the pressure range 3.4 to 15.9 MPa (900 to 2300 Psia), Winfrith, England, United Kingdom Atomic Energy Authority, AEEW-R524, 1979.

[25] Bromley, L. A., Heat transfer in stable film boiling, *Chemical Engineering Progress*, Vol. 46, No. 5, pp. 221-226, 1950.

[26] Bubelis, E., Kaliatka, A., Uspuras, E., RELAP-3D code application for RBMK-1500 Reactor Core Analysis, Submitted for ICONE-10 conference, Arlington, USA, April 14-18, 2002.

[27] Burlakov, E.V., et.al, Critical Experiments performed for Validation and Improvement of the RBMK Design, Transactions of the American Nuclear Society, 77, 380 (1997).

[28] Burlakov, E.V., et.al., Critical Benchmark Experiments for the RBMK Design, Proceedings of Intl. Conference on the Physics of Nuclear Science and Technology, Long Island, USA, October 5-8, 1998.

[29] Burlakov, E.V., Glembotsky, A.V.,Davydova, G.B., Jitarev, V.E.,Kachanov, V.M., Kuzmin, A.N., Krayushkin, A.V., Fedosov, A.M., An analysis of the experiments with Erbium for the RBMK design, ANS International Topical Meeting on Advances in Reactor physics and Mathematics PHYSOR 2000, Pittsburgh, USA, May 7-12, 2000.

[30] Burlakov, E. V., Balygin, A. A., Krayushkin, A. V., Fedosov, A M. And Tsareva, S. M. Depth of iodine well in RBMK burning uranium – erbium fuel, *Atomic Energy*, Vol. 93, No. 2, 2002.

[31] Carslaw, H.S. and Jaeger, J.C. "Conduction of Heat in Solids", Second edition, Oxford University Press, London, 1962.

[32] Casal, J. J., Stamm'ler, R. J. J., Villarino, E. A., Ferri, A. A., HELIOS: Geometric Capabilities of a new Fuel – Assemblyu Program, Proceedings of the International Topical Meeting Advances in Mathemetics, Computations and Reactor Physics, Pittsburgh, PA, USA, April 28 - May 2, 1991.

[33] Celata, G. P., Cumo, M., D'Anibale, F., A data set of critical heat flux of boiling R-12 in uniformly heatedvertical tubes under transient conditions. *Experimental and thermal fluid science*, 1991.

[34] Celata, G., P., Cumo, M., Katto, Y., Mariani, A., A new mechanistic model for the prediction of the CHF in water subcooled flow boiling, *Proceedings of 3rd International Conference on Multiphase Flow ICMF'98*, Lyon, France, June, 1998.

[35] Celata, G. P. Mishima, K., Zummo, G., Critical heat flux prediction for saturated flow boiling of water in vertical tubes, *International Journal of Heat and Mass Transfer*, Vol. 44, pp. 4343-4331, 2001.

[36] Celovani, S., Insertion of the 1995 look-up table into the ANTEO code. 3rd research co-ordination meeting on thermalhydraulics

relationships for advanced water cooled reactors, Obninsk, Russia, October 1997.

[37] Cheng, X., Erbacher, F. J., Muller, U., Critical Heat Flux in uniformly heated vertical tubes, *Int. J. of Heat and Mass Transfer*, vol. 40, No. 12, August 1997.

[38] Chernik, J. and Vernon, R., Some Refinements in the Calculation of Resonance Integrals, *Nucl. Sci. Eng.* 4, p 649.

[39] Chernobyl Accident. Technical Lessons, RRC KI, Moscow, 1996.

[40] Cho, D.H. and Bova, L. "Formation of Dry Pockets During Water Penetration into a Hot Particle Bed", Trans. ANS, Vol. 41, 1983.

[41] Cizek, J., DNB analysis of the VVER CHF data bank. 3rd research coordination meeting on thermalhydraulic relationships for advanced water cooled reactors, Obninsk, Russia, October, 1997.

[42] Chang, S. H., Baek, W. P., Bae, T. M., A study of critical heat flux for low flow of water in vertical round tubes under low pressure. *Nuclear Engineering and Design*, Vol. 132, pp. 225-237, 1991.

[43] Clemente, M., Langenbuch, S., Kusnetsov, P., Stenbock, I., Investigation of void recativity behavior in RBMK reactors, ANS International Topical Meeting on Advances in Reactor physics and Mathematics PHYSOR 2000, Pittsburgh, USA, May 7-12, 2000.

[44] Coffield, R. D., Jr, Rohrer, W. M., Jr., Tong, L. S., An Investigation of the Departure from Nucleate Boiling in a Crossed Rod Matrix with Normal Flow of Freon 113 Coolant, *Nuclear Engineering and Design*, 6, 147, 1967.

[45] Collier, J. G., Convective Boiling and Condensation, McGraw – Hill International Book Company, 1972.

[46] CORETRAN-01 Volume 1: General overview, Electric Power Research Institute, Palo Alto, CA, 1997.

[47] CORETRAN-01 Volume 2: User's manual, Electric Power Research Institute, Palo Alto, CA, 1997.

[48] CORETRAN-01 Volume 3: Programmer's manual, Electric Power Research Institute, Palo Alto, CA, 1997.

[49] Courtaud, M., Deruaz, R., D'Aillon, L. G., The French thermal-hydraulic program aqddressing the requirements of the future pressurized water reactors. *Nuclear Technology*, Vol. 80, pp. 73-82, 1982.

[50] Davidova, G. B., Kachanov, V. M., 1995. Experiments on the RBMK Critical Facility. Data for calculation modeling. Kurchatov Insitute, Moscow (in Russian).

[51] Decossin, , E., Numerical Investigations on Particulate Debris Bed Coolability: Critical Analysis of the SILFIDE Experimental Project. *Proceedings of NURETH-9 conference*, San Francisco, CA, October 3-9, 1999.

[52] Dell, F.R., Pratt, H. R. C., Flooding Rates for Packed Columns, *Inst. Chem. Eng*., 29, 89 (1951).

[53] Dougall, R. L. and Roshenow, W. M., Film boiling on the inside of vertical tubes with upward flow of the fluid at bw qualities, MIT-TR-9079-26, 1973.

[54] Dresner, L., The Effective Resonace Integrals of U^{238} and Th^{232}, Nucl. Sci. Eng. 1, pp 68, 501.

[55] El-Wakil, M., M., 1971, Nuclear Heat Transport, International Textbook Company, Cranton, USA.

[56] Farmer, M. T., Spencer, B. W., Kilsdonk, D. J., Assessment of water ingression phenomenon and proposed separate effect tests. Presented at MACE/TAC meeting, Palo Alto, CA, USA, February 16-18, 2000.

[57] Farmer, M.T., Modeling of ex-vessel corium coolability with the CORQUENCH code, *Proceedings of ICONE-9 conference,* Nice, France, April 8-12, 2001.

[58] Fedosov, A. M., Improvement of the RBMK core: modern actions and perspectives. Presented at the IAEA Regional Workshop on RBMK Safety Issues, Visaginas, Lithuania, 25-29 November, 2002 (in Russian).

[59] Fighetti, C. F., Reddy, D. G., Parametric study of CHF data, Vol. 1: Compilation of CHF data obtained at Columbia University. Final Report, EPRI, RP-813-1, 1982.

[60] Fighetti, C. F., Reddy, D. G., A generalized sub-channel CHF correlation for PWR and BWR fuel assemblies. EPRI-NP-2609-Vol. 2, 1983.

[61] Fisher, M., Main Conceptual Features of the EPR Melt Retention Concept, OECD Workshop on Ex-Vessel Debris Coolability, Karlsruhe, Germany, 16-18 November, 1999.

[62] Glasstone, S., Sesonske, A., 1994, Nuclear Reactor Engineering, Chapman & Hall, Inc., London.

[63] Gellersted, J.S., et. al., Two-phase flow and heat transfer in rod bundles, ASME, Los Angeles, pp. 63-71, 1969.

[64] Ginsberg, T., Klein, J., Klages, J., Schwarzand, C.E., Chen, J.C. "Transient Core Debris Heat Removal Experiments and Analysis", presented at the International Meeting on Thermal Nuclear Reactor Safety, Chicago, Illinois, 1982.

[65] Groenevald, D. C., Post-dryout heat transfer at reactor operating conditions. AECL-4513, presented at Topical Meeting on Water Reactor Safety, ANS, Salt Lake City, USA, 1973.

[66] Groenevald, D. C. and delorme, G. G. J., Prediction of thermal nonequilibriumin the post-dryout regime, *Nuclear Engineering and Design*, Vol. 36, No. 1, pp. 17-26, 1976.

[67] Groenevald, D. C., Cheng, S. C., Doan, T., 1986 AECL-UO critical heat flux look-up table. *Heat Transfer Engineering*, 1986, 7 (1-2), 46-61.

[68] Groenevald, D. C., On the Definition of Critical Heat Flux Margin, *Nuclear Engineering and Design* 163 (1996) 245-247.

[69] Groenevald, D. C., et al, A general method of predicting critical heat flux in advanced water-cooled reactors. *Proceedings of NURETH-9 conference*, San Francisco, USA, 1999.

[70] Handbook about Ignalina Nuclear Power Plant, LEI, Kaunas, 1997.

[71] Hall, P. C., Hall, C. M., Quenching of a Hot Particulate Debris Bed by Bottom Flooding: Preliminary Results and Analysis, Presented at the European Two-Phase Flow Group Meeting, Eindhoven, The Netherlands, 1981.

[72] Hall, D. D., Mudawar, I., Critical Heat Flux (CHF) for Water Flow in Tubes – I. Compilation and Assessment of World CHF Data, *International Journal of Heat and Mass Transfer* 43, pp. 2573-2604, 2000.

[73] Hall, D. D., Mudawar, I., Critical Heat Flux (CHF) for Water Flow in Tubes – II. Subcooled CHF correlations, *International Journal of Heat and Mass Transfer* 43, pp. 2573-2604, 2000.

[74] Henry, A. F., Nuclear reactor analysis, MIT press, 1980.

[75] Hewitt, G. F., Govan, A. H., Phenomena and prediction in annular two-phase flow. Proc. of ASME Winter Annual Maating, Dallas, USA, 1990.

[76] Hewitt, G. F., Delhaye, J. M. And Zuber, N. Post-dryout Heat Transfer. CRC press, FL, 1993.

[77] Hu, K., Theofanous, T.G., *Scale effects and structure of dryout zone in debris bed coolability experiments*, Proceedings of 6th Information Exchange Meeting on Debris Coolability, UCLA, CA, 1984.

[78] Hutton, J. L., New capabilities of the WIMS code, ANS International Topical Meeting on Advances in Reactor physics and Mathematics PHYSOR 2000, Pittsburgh, USA, May 7-12, 2000.

[79] Ignalina NPP Unit 2 Safety Analysis Report, Task 5. Accident analysis, Chapter 1. Database of initial data and engineering handbooks, Section 1.1. Main circulation circuit database, Kaunas, LEI, 2001.

[80] Ignalina NPP Unit 2 Safety Analysis Report, Task 5. Accident analysis, Chapter 2. Accident analysis during normal reactor operation and reactor start up, Section 2.3. Analysis of accidents, resulting into change of coolant flowrate through the reactor core, Kaunas, LEI, 2001.

[81] Ignalina NPP Unit 2 Safety Analysis Report, Task 5. Accident analysis, Chapter 3. Analysis of ATWS for reactor power operation and during reactor start-up, Section 3.1. Analysis of the maximum reactivity insertion during continuous withdrawal of a single control rod from central and peripheral part of the reactor core, Kaunas, LEI, 2001.

[82] Iloje, O. C., Roshenow and Griffith, P. Three-step model of disperssed flow heat transfer (post-CHF vertival flow), ASME paper #75-WA/HT-1, 1975.

[83] Investigation of the flow intensifiers for the RBMK-1500 reactor fuel assembly, RRC KI report, 1977.

[84] International Atomic Energy Agency, Safety Series No. 75-INSAG-3, Vienna, 1989.

[85] Jasiulevicius, A., Kubarev, A., Sehgal, B. R., Development and Validation of a Methodology for Neutron Dynamics Analysis of RBMK Reactors, ANS International Meeting on Mathematical Methods for Nuclear Applications, Salt Lake City, USA, September 9-12, 2001.

[86] Jasiulevicius, A., Sehgal, B.R., VIPRE02 code assessment for CHF and post-CHF heat transfer modes in long tubes, Proceedings of ICONE-10 conference, Arlington, USA, April 14-18, 2002.

[87] Jasiulevicius, A., Kubarev, A., Sehgal, B.R., CORETRAN code application for RBMK reactor safety analysis, Proceedings of PHYSOR 2002 conference, Seoul, Korea, October 7-10, 2002.

[88] Jasiulevicius, A., Sehgal, B. R., Asmolov, V., Kobzar, L., VIPRE02 code development and validation for CHF prediction in RBMK reactor fuel assemblies, Proceedings of ICONE-11 conference, Tokyo, Japan, April 20-23, 2003.

[89] Jukov, Yu. M., Use of skeleton tables fortube for heat transfer crisis calculation in rod bundles for water cooled reactor. *Atomic energy*, Vol. 17, No. 2, 108-111, 1994.

[90] Kaviany, M. "Principles of heat transfer in porous media", Second Edition, Springer, 1995.

[91] Katto, Y., Ohno, H., An improved verssion of the generalized correlation of critical heat flux for the forced convection boiling in uniformly heated vertical tubes. *International Journal of Heat and Mass Transfer*, Vol. 27, pp.1641-1648, 1984.

[92] Katto, Y. , Yokoja, S., A data set of critical heat flux of boiling R-12 in uniformly heated vertical tubes including very large length-to-diameter ratio. International Journal of Heat and Mass Transfer, Vol. 30, pp. 2261-2269, 1987.

[93] Katto, Y., A physical approach to critical heat flux of subcooled flow boiling in round tubes. International Journal of Heat and Mass transfer, Vol. 33, pp. 611-620, 1990.

[94] Katto, Y., Critical heat flux, *Internationa Journal of Multiphase flow*, Vol. 20, pp. 53-90, 1994.

[95] Kirilov, P. L., Bobkov, V. P., On standard critical heat flux for round tubes. *Proceedings of the NURETH-4 conference*, Karlsruhe, 1989.

[96] Kirilov, P. L., Some aspects of heat transfer during nuclear reactor accidents. *Proceedings of 10th International Heat Transfer Conference*, 1994.

[97] Kirilov, P. L., Smogalev, I. P., On the look-up tables for the critical flux in tubes (history and problems). *Proceedings of the NURETH-7 conference*, New York, 1995.

[98] Kitamura, M., et al, BWR 9×9 Type-A and Type-B fuel assembly critical power tests at high pressure conditions, *Proceedings of ICONE-6 conference*, San Diego, CA, USA, 1998.

[99] Khabenski, V. B., Malkin, S. D., Shalia, V. V:, Ilukhin, Yu. H., Nigmatulin, B. I., Critical heat flux in vertical bottom-closed rod bundles, *Nuclear Engineering and Design*, Vol. 182, pp. 203-224, 1998.

[100] Khabenski, V.B.et al Critical heat flux prediction in rod bundles under upward mass flux densities. Jour. Nuclear Engineering and Design 183 (1998) 249-259.

[101] Knoglinger, E., Burlakov, E., Krayushkin, A., Kubarev, A., Stenbox, I., Ionov, A., Rozhdestvensky, M., Evaluation of the Smolensk-3

Shutdown System. Final report: Phase II and III: Steady State and Transient Analysis. PSI Bericht Nr. 96-10, April 1996. ISSN 1019-0642.

[102] Konovalikhin, M.J., Yang, Z.L., Amjad, M. and Sehgal, B.R. "On Dryout Heat Flux of s Particle Debris Bed with a Downcomer", ICONE-8, Baltimore, USA, April, 2000.

[103] Konovalikhin, M.J. and Sehgal, B.R "Investigation of Volumetrically Heated Debris Bed Quenching", ICONE-9, Nice, France, April 8-12, 2001.

[104] Konovalikhin, M. J., Investigations on melt spreading and coolability in a LWR severe accident, Ph. D. Thesis, ISSN 1403-1701 Kärnkraftsäkethet 8, Stockholm, 2001.

[105] Konovalikhin, M.J., Jasiulevicius, A., Sehgal, B.R., Debris bed coolability in the BWR pressure vessel, *Proceedings of 6th ASME-JSME conference*, Cohala Coast, USA, March 16-20, 2003.

[106] Kutateladze, S. S., Leontjev, A. I., Some applications of the asympthotic theory of the turbulent boundary layer, *Proc. of the 3rd International Heat Transfer Conference*, Vol. 3, pp. 1-6, Chicago, Illinois, USA, 1966.

[107] Lagenbuch, S., Lisorkin, M., Rohde, U., Velkov, K., 3D Neutronics Codes coupled with Thermal-Hydraulics System Codes for PWR, BWR and VVER reactors, OECD/CSNI Workshop on Transient Thermal-Hydraulic and Neutron Codes requirement, Annapolis, USA, November 5-8, 1996.

[108] Lamarsh, J. R., Baratta, A. J., Introduction to nuclear engineering, Prentice Hall, 2001.

[109] Lee, C. H., Mudawar, I., A mechanictic critical heat flux model for cubcooled flow boiling based on local bulk flow conditions, *International Journal of Multiphase Flow*, Vol. 14, No. 6, pp. 711-728, 1988.

[110] Levitan, L. L., Lantsman, F. P., Effect of diameter on tube dryout. *Heat transfer – Soviet research*, Vol. 12, No. 3, 1980.

[111] Likhanskii, V. V., Loboiko, A. I., Khoruzhii, V. O., Critical heat fluxes when boiling occurs in a non-uniform heat-releasing porous medium. *Atomic Energy*, Vol. 84 (4), pp. 230-236, 1998.

[112] Liu, W., Nariai, H., Inasaka, F., A machanistic model for critical heat flux of subcooled flow, *Proceedings of the 5th ASME/JSME joint thermal engineering conference*, San Diego, USA, March, 1999.

[113] Lindholm, I., "A Review on Dryout Heat Fluxes and Coolability of Particle Beds", VTT Research Report, ENE 4/29/2000.

[114] Lipinski, R.J., "A Model for Boiling and Dryout in Particle Beds", Sandia Labs, SAND 82-9765, NUREG/CR-2646, 1982.

[115] Lipinski, R.J., "A Coolability Modal for Post Accident Nuclear Reactor Debris", Nuclear Technology, Vol. 65, pp. 53-66, 1984.

[116] Lister, C. R. B., On the penetration of water into hot rock, Geophys. J. R. astr. Soc. (1974) 39, 465-509.

[117] Lowdermilk, W. H., Lanzo, C. D., Siegel, B. L., Investigation of boiling burnout and flow stability for water flowing in tubes, NACA-TN-4382.

[118] Park, S., Lecture notes on Flow Boiling, CHF and post-CHF, RIT, Stockholm, 2003.

[119] Reed, A.W., Boldt, K.R., Gorham-Bergeron, E.D., Lipinski, R. J., Schmidt, T.R., DCC-1/DCC-2 Degraded Core Coolability Analysis, Report NUGER/CR-4390, SAND85-1967, Washington, D.C., October 1985.

[120] RELAP5/MOD7 Blowdown code, Version 2, Code Development and Analysis Program Report, Idaho National Engineering Laboratory, Idaho Falls, Idaho, USA, CDAP-TR-78-036, August 1978.

[121] RELAP5/MOD3.3Beta Code manual. Volume 4: Models and correlations. NUREG/CR-5535/Rev1 – Vol 4. 2001.

[122] Romas, A., 1999. Development, Validation and Application of an RBMK Reactor Physics Capability at KTH. Engineering Licentiate Thesis. Royal Institute of Technology, Stockholm.

[123] Paladino, D. Theerthan, A., Sehgal, B. R. DECOBI: investigation of melt coolability with bottom coolant injection, *Progress in Nuclear Energy*, Vol. 40, No. 2, pp.161-206, 2002.

[124] Parametric study of CHF data, Volume 2: A generalized subchannel CHF corerelation for PWR and BWR fuel assemblies. Electric Power Research Institute, Palo Alto, Ca, Prepared by Heat Transfer Research Facility, Department of Chemical Engineering, Columbia University, New York, March 1982, EPRI-NP-2609.

[125] Pedersen, E. S., Nuclear Power, Ann Arbor Science, 1978.

[126] Macbeth, R. V., Burnout Analysis, Part 5: Examination of published world data for rod bundles. AEEW-H-358, 1964.

[127] Magallon, D. and Honmann, H. High pressure corium melt quenching tests in FARO**,** *Nuclear Engineering and Design*, Volume 155, (1995), p. 253-270.

[128] Magallon, D., Huhtiniemi, I. and Hohmann, H. Lessons learned from FARO/TERMOS corium melt quenching experiments**,** *Nuclear Engineering and Design*, Volume 189, Issues 1-3, (1999), p. 223-238 .

[129] Magallon, D. and Huhtiniemi, I. Corium melt quenching tests at low pressure and subcooled water in FARO**,** *Nuclear Engineering and Design*, Volume 204, (2001), p. 369-376.

[130] Majhoub, F., Dor, I., Morel, C., The three-dimensional module of the CATHARe code, SMTH/LMDS/EM/99-032, Grenoble, France, January 2000.

[131] Marshall, J.S., Dhir, V.K., On the counter-current flow limitations in porous media. *International meeting on LWR Severa Accident Evaluation*, Cambridge, Ma, August 28- September 1, 1983.

[132] Mayer, P., Burger, M., Buck, M., Schmidt, W., Lohnert, G., Investigations on the coolability of debris in the lower head with WABE-2D and MESOCO-2D. *OECD/CSNI Workshop on In-vessel Core Debris Retention and Coolability*, March, 1998.

[133] Mishima, K., Nishihara, H., Michiyoshi, I., Boiling burnout and flow instabilities for water flowing in a round tube under atmospheric pressure, *International Journal of Heat and Mass Transfer*, Vol. 28, pp.1115-1129, 1985.

[134] Mishima, K., Nishihara, H., Effect of channel geometry on critical heat flux for low pressure water in small diameter tubes. *Proceedings of the 6th International topical meeting on nuclear reactor thermal hydraulics*, Grenoble, Fraqnce, 1993.

[135] Nuclear Safety Regulations for Reactors of Nuclear Power Plants, VD-T-001-0-97, VATESI, 1997.

[136] Nourgaliev, R. R., Modelling and analysis of heat and mass transfer processes during in-vessel melt progression stage of LWR severe accidents, Ph. D. Thesis, ISSN 1403-1701 Kärnkraftsäkerhet 2, Stockholm, 1998.

[137] Olekhnovitch, A., Teyssedou, A., Tapucu, A., Champagne, P., Groenevald, D. C., Critical Heat Flux in a Vertical Tube at Low and Medium Pressures. Part I. Experimental Results, *Nuclear Engineering and Design* 193, pp. 73-89, 1999.

[138] Olekhnovitch, A., Teyssedou, Tye, P., Critical Heat Flux in a Vertical Tube at Low and Medium Pressures. Part II. New data representation, *Nuclear Engineering and Design* 193, pp. 91-103, 1999.

[139] Osmachkin V.S., Studies of thermal-hydraulic characteristics of models for reactor fuel assemblies, Seminar TF-74, “Studies of critical thermal fluxes in rod bundles”, Moscow 1974.

[140] Osmachkin V.S., Studies of thermal-hydraulic characteristics of models for reactor fuel assemblies, Seminar TF-74, “Studies of critical thermal fluxes in rod bundles”, Moscow 1974.

[141] Ott, K. O., Bezella, W. A., Introductory nuclear reactor dynamics, American Nuclear Society, La Grange Park, Il, USA, 1985.

[142] Ott, K. O., Bezella, W. A., Introductory nuclear reactor statics, American Nuclear Society, La Grange Park, Il, USA, 1989.

[143] Parametric study of CHF data, Volume 2: A generalized subchannel CHF correlation for PWR and BWR fuel assemblies, Electric Power Research Institute, Palo Alto, CA, Prepared by Heat Transfer Research Facility, Department of Chemical Engineering, Columbia University, New York, EPRI-NP-2609, 1982.

[144] Safety Assessment and Verification for Nucler Power Plants, IAEA Safety Standarts Series, Safety Guide No. NS-G-1.2, International Atomic Energy Agency, Vienna, 2001.

[145] Schrock, V.E., Wang, C.-H., Revankar, S., Wei, L.H., Lee, S.Y., squarer, D., Flooding in particulate beds and its role in dryout heat flux, Proceedings of 6th Information Exchange Meeting on Debris Coolability, UCLA, CA, 1984.

[146] Sehgal, B. R. and Goldstein, R. Intermediate resonance absorption in heterogeneous media, Nuclear science and Engineering 25, 174 (1966).

[147] Sehgal, B.R., and Spencer, B. W., Ace Program Phase D: Melt Attack and Coolability Experiments (MACE) Program, Proceedings of 2nd specialist Meeting on Molten Core Debris – Concrete Interactions, Karlsruhe, Germany, 1992.

[148] Sehgal, B.R., et al, Investigation on Melt-Structure-Water-Interactions (MSWI) During Severe Accidents, SKI Report 99:42, ISSN 1104-1374, (1999), Stockholm.

[149] Sehgal, B.R., Cheng, H.W., Romas, A., Validation of the ARROTTA code against Experimental RBMK Critical Facility Data, ANS International Topical Meeting on Advances in Reactor physics and Mathematics PHYSOR 2000, Pittsburgh, USA, May 7-12, 2000.

[150] Sesonske, A., 1973, Nuclear Power Plant Design Analysis, US Atomic Energy Commision, USAEC Technical Information Center, Oak Ridge, USA.

[151] Spart, R., Laoke, H., Mewes, D., Mayinger, F., Countercurrent flow behavior in the fuel element top nozzle area. *Nuclear Engineering and Design*, Vol. 99, No. 1, pp. 131-139, 1987.

[152] Smolin, V. N., Polyakov, V. K., Critical heat flux investigations in rod bundles, *Thermal Engineering*, Vol. 4, pp. 54-58, 1967.

[153] Stacey, W. M., Nuclear Reactor Physics, John Wiley & Sons, Inc., 2001.

[154] Studsvik Scandpower. HELIOS Documentation. HELIOS methods. 1998.

[155] Studsvik Scandpower. HELIOS Documentation. HELIOS Functional Tests. 1998.

[156] Stolyarova, V.L:, Green, J., Physico-chemical properties of the Cao-B_2O_3 system, NPS-EDPR-97-22 Report (1997).

[157] Theofanous, et al, In-vessel coolability and retention of a core melt, DOE/ID-10460, 1995.

[158] Theofanous, T. G., Liu, C., and Yuean, W. W., Coolability and Quench of Corium – Concrete Interaction by Top Flooding, MACE-TR-D15, August, 1998.

[159] Thompson, B., Macbeth, R. V., Burnout in uniformly heated round tubes: a compilation of world data with accurate correlation. AEEW-R356, 1964.

[160] Todreas, N. E., Kazimi, M. S., 1990, Nuclear Systems, Hemisphere Publishing Inc.

[161] Tong, L.S., Heat transfer in water-cooled nuclear reactors, Nuclear Engineering and Design, Vol. 6, 301-324, 1967.

[162] Tong, L. S., Weisman, J., Thermal Analysis of Pressurized Water Reactors, *an AEC Monograph*, American Nuclear Society, 1970.

[163] Tong, L. S., Boiling Crisis and Critical Heat Flux, USAEC, 1972.

[164] Tong, L. S. and Young, J. D., A phenomenological transition and film boiling heat transfer correlation, paper 133.9, Heat Transfer 1974, Vol. IV, Fifth International Heat Transfer Conference, Tokyo, Japan, 1974.

[165] Transient and Accident Analysis of RBMK Nuclear Power Plants, RBMK-SC-052, International Atomic Energy Agency, Vienna, January 1998.

[166] Tung, V. X., Dhir, V. K., ”Quenching of a Hot Particulate Bed by a Bottom Flooding, Proc. ASME-JSME Thermal Engineering Joint Conference. Honolulu, Hawaii, USA, 1983.

[167] Tung, V.X., Dhir, V.K. and Squarer, D. "Quenching by Top Flooding of a Heat Generating Particulate Bed With Gas Injection at the Bottom", Proc. of the 6th Information Exchange Meeting on Debris Coolability, 1986.

[168] Urbonas, R., RELAP-5 analysis of RBMK-related flow instability experiments. Licenciate’s thesis. Royal Institute of Technology. ISSN 1403-1701, 1998.

[169] Villarino, E. A., Stamm’ler, R. J. J., HELIOS: transformation Laws for Multiple – Collision Probabilities with Angular Dependence. Proceedings of PHYSOR 96 confernce, Mito, Ibaraki, Japan, September 16-20, 1996.

[170] Voroncov, B., et. al., Control rod efficiency measurements during reactor subcriticality, Report, Ignalina NPP(2002) (in Russian).

[171] Wallis, G., One-dimensional two-phase flow, McGraw-Hill Boo Co, New York, (1969).

[172] Weber, P. Johannsen, K., Study of critical heat flux condition at convective boiling of water: temperature and power controlled experiments. *Proceedings of the 9th International Heat Transfer Conference,* Jerusalem, Israel, 1990.

[173] Whalley, P. B., Two-Phase Flow and Heat Transfer, Oxford Science Publications, Oxford university press, 1996.

[174] Whalley, P. B., Baoiling, Condensation and Gas-Liquid Flow.Oxford engineering science series-21, Clarendon Press, Oxford, 1987.

[175] Yoder, G. L., Morris, D. G., Mullins, C. B., Rod bundle burnout data and correlation comparisons, *Nuclear Technology*, Vol. 68, pp. 355-369, 1985.

[176] Yoo, S. – J., France, D. M., Post-CHF heat transfer with water and refrigerants, *Nuclear Engineering and Design* 163, pp. 163-175, 1996.

[177] Zweifel, P. F., Reactor Physics, McGraw-Hill, Inc., 1973.